Inherent Electric Field Measurements of Liquid Surfaces using Ionizing Surface Potential

Dissertation

Presented in Partial Fulfillment of the Requirements for the Degree Doctor of Philosophy in the

Graduate School of The Ohio State University

By

Tehseen Adel

Graduate Program in Chemistry

The Ohio State University

2021

Dissertation Committee

Prof. Heather C. Allen, Advisor

Prof. Anne C. Co

Prof. John M. Herbert

Prof. Matthew D. Ringel

Abstract

Measurements of the inherent electrical nature of the gas-liquid interface have persisted for over a century of anthropological advancement. Within its broad remit, the microscopic picture of the surface structure of the gas-liquid interface continues to be laid out by various theoretical and experimental contributions. The ionizing surface potential technique extends a distinct yet complementary approach to quantifying the inherent surface electric fields of aqueous and nonaqueous liquids. The studies in this dissertation offer insight into the nature of electrochemical measurements using the presented ionizing surface potential. These studies also contribute key interpretations as it relates to the fundamentals of the structural arrangement of interfacial molecules of solvents and the surface activity of ions and surfactants.

The surface electrical potential (χ or chi potential) at the gas-liquid interface is a macroscopic property of the electric dipolar (and quadrupolar) moment of molecules available at this interface. In measuring the potential difference across two phases, inherent features of the interfacial structure, especially the orientation of molecular dipoles and intermolecular interactions of surface molecules, are observed. In this work, the ionizing surface potential method is developed and utilized in the measurements of aqueous, nonaqueous, and electrolytic solvents. Despite its sensitivity for aqueous electrolyte systems, the ionizing method is relatively uncommon and utilized infrequently resulting in a 40–50-year knowledge gap since the last ionizing-related surface potential measurements on aqueous electrolytes. The first part of this work relates to the fabrication of the Ionizing Surface Potential Sensor (ISPS), and the adoption of necessary controls to ensure accurate and reproducible results with increased sensitivity to

aqueous electrolytes and nonaqueous solvents alike. The ISPS consists of a custom americium-241 (Am-241) ionizing working electrode that is suspended a few millimeters in the air over a liquid sample, within which a platinum gauze reference electrode is submerged. Alpha particles emitted from the active area of the Am-241 ionize the air gap to a small extent, allowing for current flow within the measuring circuit (high impedance electrometer). The potential difference (also known as the measurable surface potential) measured across the two electrodes is electrochemically proportional to the surface electric potential of the air–solution interface.

Moving towards an active understanding of the measurable surface potential requires a fundamental understanding concerning the robustness of its reported values. Herein proposed is a circuit model for the ISPS based on the alpha decay of a radioactive americium-241 electrode. With this model, the robustness of the surface potential at the air–aqueous interface is validated through the determination of derived surface energies at the air–electrolyte interface. Successful validation of the circuit model is made with a comparison interface with comparison to respective surface tension literature values. Apart from the circuit model, measured surface potentials are evaluated and assessed against factors such as the type of counter electrode and changes in the ionizing environment impact the magnitude of the measured response.

In the latter half of this work, the impact of aqueous inorganic ions upon the interfacial electric field of the air–aqueous interface is observed using ISPS. Here, measured potentials of aqueous halide electrolytes were normalized to well-known ionic surfactants, cetyltrimethylammonium bromide (CTAB) and sodium dodecyl sulfate (SDS). With potential measurements of sodium halide solutions, iodide has a dominant effect on the air–aqueous electric field. Compared to chloride and bromide, iodide is also directly observed with a net negatively charged surface electric field at all salt concentrations measured (0.2 to 3.0 mol/kg water). In concentrations above 2 mol/L, bromide is observed with a net negatively charged

surface. These results show the surface enrichment of bromide and iodide. Langmuir and Frumkin-Fowler-Guggenheim adsorption isotherm is used to quantify the specific adsorption of these anions at the air–aqueous interface.

Given recent interests in the solubility of ions in nonaqueous solvents, the measured surface potential of several neat solvents (methanol, acetonitrile, propylene carbonate, 1.2-dichloroethane, and diethyl ether) and water are presented. The surface potential difference of the air/water interface measured with ISPS ranges between -0.40V $< \chi_{H_2O} <$ -0.49 V. Using conventions of surface electrical potential theory, the direction of the surface dipole of a water molecule (aligned perpendicular to the surface normal) points from the gas towards the liquid, i.e., hydrogens orient towards the gas, the expected sign of the surface potential is negative. Thus, we conclude that our surface potential for water indicates a net orientation of water dipole towards the air. However, this molecular orientation is considered not to be the dominant motif observed in spectroscopic studies of the air-aqueous interface. In contrast to water, the measured surface potentials of the nonaqueous solvents are positive (indicating their net dipole orient away from the air). For these solvents, the interfacial alignment of their surface dipoles varies significantly from one solvent to another. As a result, we also re-evaluate the contribution of the dipoles for each solvent using a simple Helmholtz model. From our results, we conclude that interpretation of orientation of interfacial molecules with electrochemical measurements is heavily dependent on dipolar alignment, whereas a more holistic perspective must also require contribution from quadrupoles. Thus, interpreting surface electrical potential requires a unified approach, possibly based on theoretical groundwork, to shed light on the molecular arrangement at the gas-liquid interface.

Dedication

Soli Deo gloria

To my sister, Tabitha, and our parents, Beaula and Syed Adel.

Acknowledgments

The years of arduous work would not be possible without the love and support of many.

To begin with, I want to thank my friends Ka Chon, Maria Vazquez de Vasquez, and Mickey Rogers, whose friendship, encouragement, and camaraderie were integral in sustaining me throughout this process. I also want to acknowledge my incredible postdoctoral mentors and colleagues, Juan Velez-Alvarez and Stephen Baumler, for their mentorship and collaboration with the studies presented in this work. I also want to thank my mentee, Meredith Varmecky, for all her hard work and her cheerful nature. Instrument fabrication and support was not possible without input from Larry Antal, Eric Jackson, and John Sullivan, and I am grateful for their help and experience.

I also want to thank Dr. Co, Dr. Schutz, and Dr. Herbert for sharing their professional expertise on this subject matter. It was invaluable! I especially want to thank my research advisor Dr. Allen for her guidance over the years and for all the opportunities she had helped make available to me.

Lastly and most importantly, I would like to thank my sister and parents for their unending love and support throughout the years. None of this would be possible without them.

Vita

2015 .... B.S., Chemistry, Cedarville University

2017 .... M.S., Chemistry, The Ohio State University

2015–2017 .... Graduate Teaching Associate,

Department of Chemistry and Biochemistry,

The Ohio State University

2017–Present .... Graduate Research Associate,

Department of Chemistry and Biochemistry,

The Ohio State University

Publications

- **T. Adel**, K. C. Ng, M. G. Vazquez de Vasquez, J. Velez-Alvarez, and H. C. Allen; *Langmuir,* 2021, 37, 7863–7874. "Insight into the Ionizing Surface Potential Method and Aqueous Sodium Halide Surfaces" (Invited Feature Article).

- **T. Adel**, J. Velez-Alvarez, Anne C. Co, Heather C. Allen; *J. Electrochem. Soc.*, 2021, 168, 016507. "Circuit Analysis of Ionizing Surface Potential Measurements of Electrolyte Solutions."

- L. Lin, J. Husek, S. Biswas, S. Baumler, **T. Adel**, K. C. Ng, L. R. Baker, H. C. Allen; *J. Am. Chem. Soc.*, 2019, *141*, 34, 13525-13535. "Iron(III) Speciation Observed at Aqueous and Glycerol Surfaces: Vibrational Sum Frequency and X-Ray."

- S. K. Reddy, R. Thiraux, B. A. Wellen Rudd, L. Lin, **T. Adel**, T. Joutsuka, F. M. Geiger, H. C. Allen, A. Morita, and F. Paesani; *CHEM,* 2018, 1629-1644. "Bulk Contributions Modulate the Sum-Frequency Generation Spectra of Interfacial Water on Model Sea-Spray Aerosols."

Fields of Study

Major Field: Chemistry

Table of Contents

List of Tables

List of Figures

List of Abbreviations & Symbols

Abbreviations

ACS	American Chemical Society
DC	Direct Current
VSFG	Vibrational Sum Frequency Generation
SHG	Second Harmonic Generation
RHE	Reversible Hydrogen Electrode
IUPAC	International Union of Pure and Applied Chemistry
ISPS	Ionizing Surface Potential Sensor
CTAB	Cetyltrimethylammonium Bromide
SDS	Sodium Dodecyl Sulfate
FFG	Frumkin-Fowler-Guggenheim

Symbols

χ	surface electric potential, V
$\Delta\chi$	surface potential difference, V
ϕ	inner electric potential, V
μ	permanent dipole moment, D or C/m
μ_z	interfacial dipole moment (relative to the surface normal)
γ	surface tension, mN/m or mJ/m^2
$d\gamma$	change in surface tension relative to water, mN/m

$$d\gamma = \gamma_{\text{salt}} - \gamma_{\text{water}}$$

V_M	measured surface potential, V
V_D	predicted dipolar surface potential, V
E_V	electric field strength associated with the gas−liquid interface, V/m
E_D	predicted electric field, V/m
Q	surface charge density
A	interfacial area, m^2
r_z	vector of the interfacial dipole moment along the z-axis
t	time, s
α	attenuation factor of alpha particle
Z_1	distance between the respective surfaces of the Am-241 electrode and solution, m
Z_2	distance between the respective surfaces of the solution and Pt gauze, m
r	radius of Am-241 electrode, m
A_s	surface area of the solution, m^2
A_{Pt}	surface area of Pt gauze, m^2
d_{gauze}	diameter of Pt gauze, m
d_{wire}	diameter of Pt wire, m
σ_s	equivalent conductivity of electrolyte solution, Ohm^{-1} cm^{-1}
κ^{-1}	Debye length electrolyte solution at an electrified interface, m

$$\kappa^{-1} = \sqrt{\frac{\varepsilon_0 \varepsilon_{H_2O} k_B T}{2 * 10^3 N_A e^2 I}}$$

ε_0	permittivity of vacuum, 8.8541878128(13) E-12 F/m

$$\varepsilon_0 = \frac{1}{v^2 \mu_0}$$

μ_0	magnetic permeability of vacuum, 1.25663706212E-06 H/m
v	speed of light, 299792458 m/s
k_B	Boltzmann constant, 1.38064852E-23 m^2 kg s^{-2} K^{-1}
T	temperature, 295.15 K
N_A	Avogadro's constant, 6.02214086E+23 1/mol
c_i	concentration of ions, mol/L
I	Ionic strength, mol/L

$$I = \frac{1}{z} \sum_i c_i z_i^2$$

C_a	capacitance at Am-241 electrode/N_2 interface, F
C_s	capacitance at air/aqueous interface, F
R_s	resistance at air/aqueous interface, Ohm
C_b	capacitance at solution/Pt interface, F
R_b	resistance at solution/Pt interface, Ohm
R_{Pt}	internal resistance (Pt gauze electrode), Ohm
Ω	amplitude of the voltage, V
λ	decaying rate of alpha particles
$\mathcal{L}$	Laplace transform
s	complex variable transform of t
β	partial fraction term 1
ζ	partial fraction term 2
η	partial fraction term 3
z	number of charges circulating in circuit
e	elementary charge, 1.6 E-19 C
E_{cell}	equivalent conductivity of electrolyte solution, V
$\Delta G_{surface}$	Gibbs free energy at the air–aqueous interface, J/mol
v_i	interfacial potential at the air–aqueous interface
E_α	attenuated energy of alpha particle, MeV
E_0	initial mean energy of alpha particle, MeV
L_α	range of attenuated alpha particle near solution surface, m
L_0	range of alpha particle nearest to radioactive electrode surface, m
τ	mass attenuation constant for alpha particles in air
$Ł(r)$	Lorentzian profile of alpha particle beam as a function of radioactive electrode diameter

Chapter 1: Introduction

1.1 Motivation

The primary objective of the studies in this dissertation is to shed light on the nature of electrical fields at the gas–liquid interface and the electrochemical methods used to quantify them. Interfaces, specifically gas–liquid, have unique chemical and physical properties, unlike either that of the gas or liquid phase. These properties arise from the asymmetry of forces experienced by interfacially available molecules and atoms.[1,2] Given the molecularly thin interface and the inherent asymmetry of the interface, these factors define the chemical nature, interfacial molecular structure, the dielectric environment, and the capacity of solute (charged and/or neutral) transport across the interface.[2–5]

There currently exists a surplus of techniques that probe at either the macroscopic or microscopic level to characterize or quantify properties of the gas–liquid interface. Among them, the electrochemical ionizing surface potential method is the least understood and applied to various chemical systems at the gas–liquid interface. Though challenging to interpret, the ionizing method is a robust and economical means of quantifying the electrical properties of an interface, particularly the gas-liquid interface. In this work, we present several studies that allow us to understand and consider the fundamentals of surface potentials and the ionizing method in the context of gas–liquid systems.

1.2 The Gas–Liquid Interface: Why it matters.

1.2.1 Structure of the Air–Aqueous Interface

Water is the simplest and most abundant molecular solvent on Earth. When considering the chemistry and physics of liquids, water is unique due to its highly directional cohesion forces and strong hydrogen bonds, which stabilize the overall intermolecular structure. At the water surface, these cohesive forces come into play as water molecules at the surface only have half the neighboring molecules compared to those in the bulk liquid. Thus, surface molecules tend to associate more strongly, which results in a strong inward force towards the liquid. This is the surface tension of water with a value of 72 mN/m (20 °C).[6] It is one of the most important physical characteristics of the air–water interface. Yet, one might ask the question, what does this surface look like at the molecular level?

The structural arrangement of water at the air–water interface is an indispensable means to rationalizing the chemical and physical phenomena that one observes at this interface. Chemically, there is a myriad of chemical reactions that occurs with different mechanisms, kinetics, and dynamics at the surface of sea spray aerosols.[7–12] In biological systems, the peptide-bond formation is unfavored in bulk liquid water, yet quite favorable at the air–water interface.[13] Furthermore, physical phenomena such as the trapping and hopping of protons along so-called "water wires",[14] changes in the acidity/basicity of molecules at the surface relative to the bulk water,[15,16] charge separation at the aqueous electrochemical interface,[17,18] and the relationship of water droplet size and its high surface tension. Since the early 2000s, there has been much progress in understanding the structure and dynamics of water molecules at the neat air–water interface. Yet, experimentally, there has been extensive characterization primarily through non-linear vibrational spectroscopies, namely Vibrational Sum Frequency Generation (VSFG), where it has been shown that the water surface is dominated by hydrogen-bonded water molecules with

a single O-H group dangling towards the air. Within the subsurface (layer below the surface), water molecules are oriented reversely with one O-H pointing toward the liquid.[19–21] The remaining water molecules orient parallelly to the surface and thus forming dimers connected by more hydrogen bonds.[22–24] It has been suggested that more than 90% of the interfacial water is coordinated via a hydrogen bonding oriented parallel to the surface, forming a continuous "water skin" above bulk waters.[24]

In contrast to non-linear spectroscopy, the electrochemical surface potential also offers insight into the interfacial structure of the air–water interface by way of the surface electrical potential χ (Figure 1-1). χ has long been considered a sensitive property of the dipolar moment of interfacial molecules μ_z (and also quadrupoles). In this dissertation, χ measurements of water will be considered and contrasted with older water measurements and those calculated via simulations. However, understanding of the fundamental relationship of the dipolar moment and the physical nature of the "water skin" is yet to be uncovered.
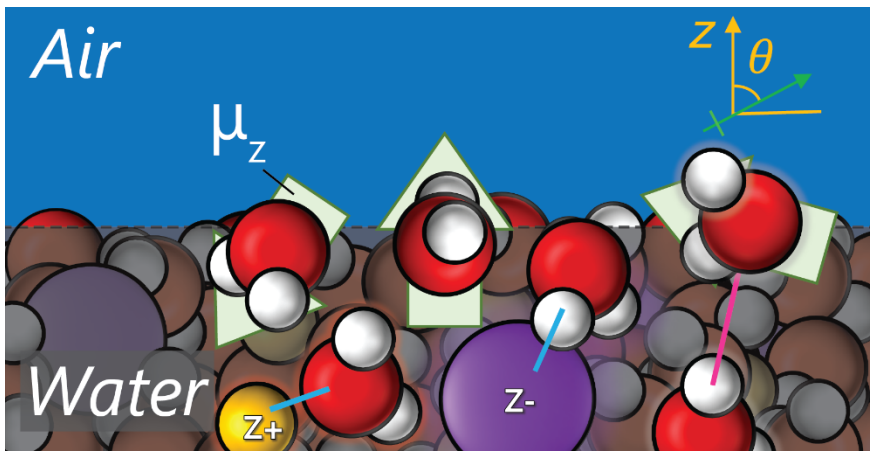
Figure 1-1. Complexity of the air−water interface. Surface electric potentials (χ) are a sensitive characteristic of the interfacial dipole moment (μ_z) and are indirectly quantified using electrochemical surface potential methods. An example of a dangling O-H from a surface water molecule is shown on the far-right side.

1.2.2 Ion Adsorption at Gas−Liquid Interfaces

The field of research related to ion solvation at air−water interfaces is vast and ongoing

since the first surface tension (γ; mN/m) measurements of aqueous salts solutions by

Heydweiller[25] in the early 20th century. Experimentally, adding inorganic electrolytes to water

was shown to increase the surface tension of water. Soon after, the first solvation models were

proposed by Wagner[26] and Onsager & Samaras[27], which predict that ions are expelled (or devoid)

of the interface. The surface tension increase to the Gibbs adsorption isotherm, where the surface

tension increase by electrolytes meant depletion of ions from the interfacial layer. Yet, from the

results of experimental surface tension, there is a clear indication that anions have a stronger

effect on the change in surface tension $d\gamma$ (where $d\gamma = \gamma_{salt} - \gamma_{water}$) relative to their cationic

counterparts.[28] For example, $d\gamma$ for aqueous salts such as NaCl and LiCl is observed to be at 1.73

and 1.65 mN/m respectively.[28] Yet, $d\gamma$ for $NaNO_3$ is 1.23 mN/m.[28] Hence, there appears to be

some specific effect of the anion on the nature of the air–water interface. Indeed, ion specificity

(first outlined by Hofmeister) marks the efficiency of some electrolytes in salting out of proteins

(Figure 1-2).[29–31] Answering the question on the distribution of ions at the air–water interface has

sweeping implications for atmospheric chemistry, biological phenomena, and technology.

Early simulations[32,33] predicted that specific anions have a greater propensity for the air–

aqueous surface over the bulk. The surface enhancement of these anions is duly observed to

correlate with the empirically determined order of the Hofmeister series[30,31,34,35], $F^- \approx SO_4^{2-} >$

$Cl^- > NO_3^- > Br^- > I^- > SCN^-$, where anions on the far left are excluded from the surface, while

anions to the right have an increased surface propensity. Yet, central to the discussion on ion

surface propensity is the extent to which heavier halides (Br^- and I^-) adsorb to aqueous surfaces;

simulations[35–38] and experiments[39–45] have presented varying results and assertions to the

thermodynamic favorability and quantitative enrichment of these halides to the aqueous surface.

$$F^- > SO_4^{2-} > HPO_4^{2-} > Acetate > Citrate > Cl^- > NO_3^- > Br^- > I^- > ClO_4^- > SCN^-$$

- Increase surface tension
- Salt out proteins (aggregate)

HOFMEISTER EFFECTS ON PROTEINS

- Decrease surface tension
- Salt in proteins (solubilize)

$$NH_4^+ > K^+ > Na^+ > Li^+ > Mg^{2+} > Ca^{2+} > guanidinium^+$$
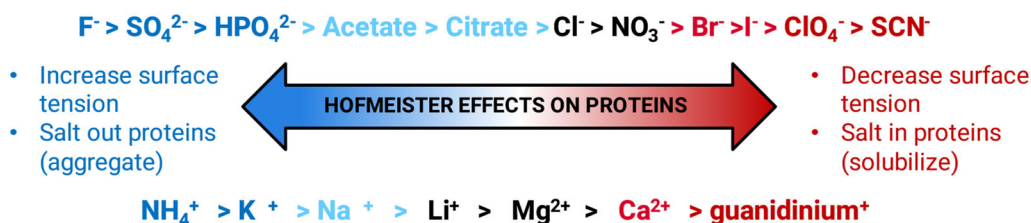
Figure 1-2. Recent version of the anionic and cationic Hofmeister series and their physical properties in their ability to salt out proteins ("stabilize" = protein aggregation, i.e., salting out). Ions that salt out proteins tend to have higher surface tension than their ionic counterparts.

1.2.3 Gas–Liquid Interfaces of Nonaqueous Solvents

Subject to long-standing interest is the solubility of ionic species in aqueous and nonaqueous liquids. As the universal solvent, water remains the primary focus of theoretical[37,46–50] models and experiments[12,40,51–54] in ion-solvation phenomena. Investigations into ion-water solvation hold major implications for atmospheric aerosols[55–58] and biological phenomena[29–31,59] (protein folding and solubility, enzyme activity). Force-field models have demonstrated specific ion adsorption at the air–water interface.[60–69] Experimental work with nonlinear[39–44,70] and X-ray surface scattering[71,72] spectroscopies and electrochemical surface potential measurements[73] also show adsorption behavior of various anions. Moreover, there is also significant interest in understanding the solubilities of ions in nonaqueous solvent media, with particular application to the separation of toxic and radioactive metals from nuclear waste[74], the recovery of critical metal ions[75,76], electrochemical environments systems[77,78], and predicting solubilities of polymers in mixed organic solvents[79] (Figure 1-3).
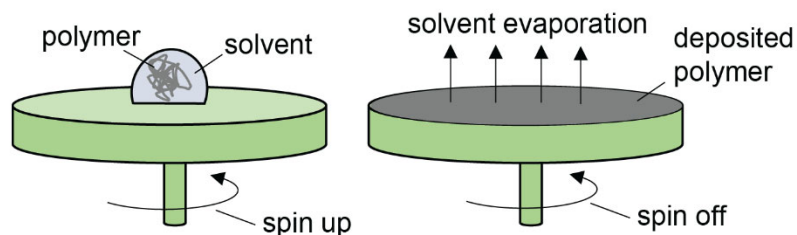
Figure 1-3. The solubility of polymers in solvents is an important factor for the precise polymer film deposition during spin coating process.

1.3. Dissertation Highlights

In this dissertation, Chapter 2 provides a detailed overview of the fundamental theory of surface potentials, the principle and methodology of the ionizing method, and the materials, controls, and calibrations used to characterize our custom-designed Ionizing Surface Potential Sensor (ISPS) instrument.

Chapter 3 involves a study relating to the validation of surface potentials measurement using a circuit model. The robustness of the ionizing circuit model is validated by using the circuit model to derive the respective surface energies of air–solution measurements from the analysis of real-time surface potential data. We successfully validate our model and the robustness of the ionizing surface potential methods by comparison of derived surface energies to established surface tension values.

In Chapter 4, the ionizing surface potential technique is used to quantifying the impact of aqueous halides upon the interfacial electric field of the air–aqueous interface. Given the vulnerability of reporting surface potentials to theoretical estimates of neat water, we recognize and evaluate aqueous ion surface potentials relative to well-known ionic surfactants cetyltrimethylammonium bromide (CTAB) and sodium dodecyl sulfate (SDS). With potential

6

measurements of sodium halide solutions, we show that iodide has a dominant effect on the air–aqueous electric field. Compared to chloride and bromide, iodide is directly observed with a net negatively charged surface electric field at all salt concentrations measured (0.2 to 3.0 mol/kg water). As a result, we use Langmuir and Frumkin-Fowler-Guggenheim adsorption isotherms to quantify the specific adsorption of bromide relative to the iodide.

In Chapter 5, we present ionizing surface potential measurements for water relative to nonaqueous solvents. In order to evaluate the extent of the interfacial dipolar moment on the measured surface potential, we propose a model to predict surface potentials from known quantities (relative permittivity, permanent dipole moment, density). From the comparison of our measurements with the predicted potentials, we show the deviation of protic methanol and water from a proposed dipolar surface potential model. In contrast, pure acetonitrile and propylene carbonate have good agreement with the model indicating their liquid surfaces are highly dipolar.

Chapter 2. Surface Electrical Potential of Gas−Liquid Interfaces

2.1 Defining Potentials at the Air–Aqueous Interface

The definitions for surface potentials have been outlined in the IUPAC.[80] Theoretical aspects of surface potential measurements have been outlined by Parsons[81] and Girault[82]. Presented here is a brief overview of surface potential theory.

For any condensed matter, there is a potential energy difference between molecules at the surface and the bulk. In polar liquids such as water, there is a greater degree of potential energy at its surface (demonstrated by its high surface tension) compared to bulk waters, resulting in its unique molecular surface structure and electrical properties. At the interface of a dilute gas (e.g., air) and water, layers of water molecules with electric dipole (and quadrupole) moments are distributed accordingly to any degree of alignment perpendicular to the surface normal.[3,4,68,81,83] Referred to as the electrical double layer, the distribution of these dipoles results from the preferential arrangement of water molecules, the differential adsorption and desorption of ions, and ion-water structures.[4,81]

Considering the energy transferred as an ideal charge moves from the air and into the liquid, the inner electric potential difference ϕ (Galvani potential difference) describes the total potential difference between its outer (air) and interior (liquid bulk) boundaries.[4,81,82,84] Starting at a point (in the air) outside any electrostatic interactions with the electrical double layer, the ψ or

outer electric potential difference (Volta potential difference) describes the work required to move an ideal charge towards a point just close to the interface itself. Beyond this, the surface electric potential difference χ describes the remaining work necessary to transfer this charge through the electrical double layer itself into the bulk liquid. Altogether, the relationship is described as (also summarized in Figure 2-1),

$$\phi = \chi + \psi \tag{2.1}$$

For the air–aqueous interface, the convention is that χ is positive as the potential changes from the air towards the liquid bulk phase, where the water dipoles are perpendicular to the surface plane (their dipoles moments oriented towards the liquid phase).[4,81,82,85,86] Given the ϕ and χ are conventionally described the same direction, it is also important to note that $\nabla\phi$ relates directly and opposite to the electric field strength $\boldsymbol{E_V}$ within the same interfacial boundaries: $\nabla\phi = -\boldsymbol{E_V}$.

Under the conditions of experimental electrochemical measurement, χ is related to the electrochemical potential difference $\tilde{\mu}_i$ of the interface, such that,

$$\tilde{\mu}_i = \mu_i + z_i\phi$$

$$= \mu_i + z_i\chi + z_i\psi$$

$$= \alpha_i + z_i\psi \tag{2.2}$$

where μ_i is the chemical potential difference, z_i is the charge of the ion, and α_i is the real potential difference. Here, the α_i describes the chemical interactions between z_i and its environment (ion-dipole, ion-induced dipole, dispersion forces, etc.) and the net dipolar alignment of the electrical double layer when $\psi = 0$. Notably, the α_i is also known as the 'real'

free energy of hydration of solvated ions; it is a relevant quantity in many molecular-level simulations.[35,60,68,87,88]

As with any electrochemical techniques, the voltaic potential difference V_M can be measured across any electrochemical cell. In the case of ionizing surface potential, alpha particles from the ionizing electrode interact with gas phase molecules and break down the resistance of the air gap. By ionizing the air gap, the ionizing method can experimentally establish $\psi = 0$. Essentially, V_M is the electromotive force of the air (in contact with Am-241) relative to the aqueous solution (in contact with Pt) when ψ (Volta potential difference) is constant:

$$V_M = \tilde{\mu}_i = \alpha_i = \mu_i + z_i \chi \tag{2.3}$$

while μ_i (chemical potential difference) directly contributes to α_i (real potential difference = measured V_M), χ (surface electric potential difference) is determined by the nature of the surface itself.

NOTE: Hereinafter, the terms "surface potential", "measured surface potential", "surface electric potential", "V_M", and "χ" will be treated synonymously unless stated otherwise.
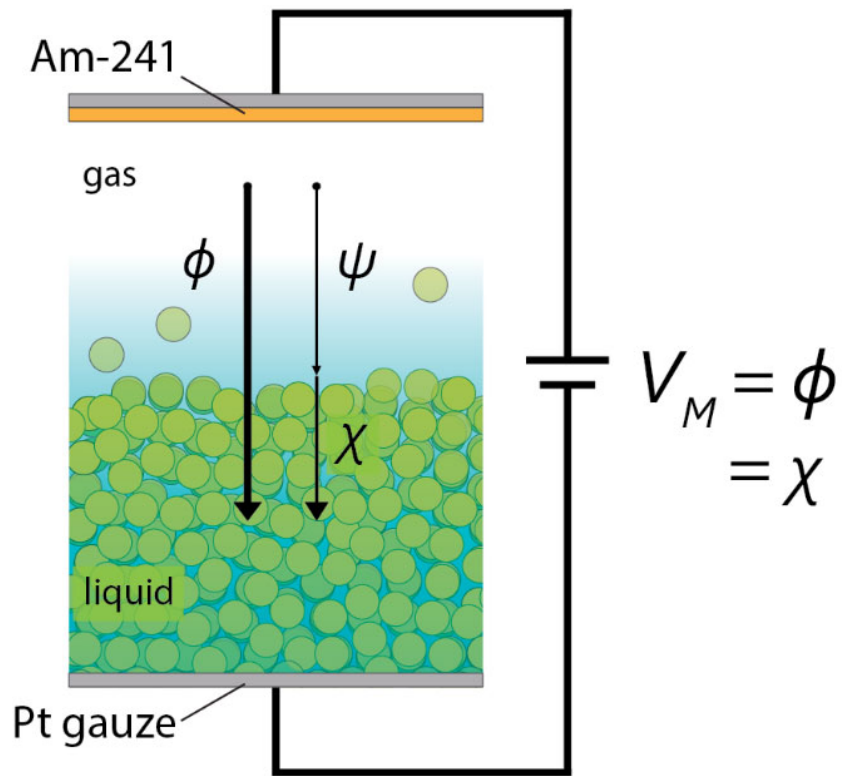
Figure 2-1. The total electrostatic potential difference ϕ of the gas–liquid interface is divided into the outer potential difference and the surface electric potential difference: $\phi = \chi + \psi$.

2.2 Ionizing Surface Potential Method

Surface potential sensing is a real-time and quantitative method to analyze the electric charge properties of a liquid or solid surface. Surface potential is an important phenomenon as it gives information about the composition and orientation of surface molecules, and the degree of interaction of subsurface molecules with those at the surface. Surface potential sensing has a variety of physicochemical applications from nanoparticle sensing, corrosion sensing, catalysis, surfactants, and monolayers sensing etc.[89,90] For liquids, potential sensing can be more problematic as there are fewer charged particles near its surface, i.e., it is more electrically insulated. Current surface potential sensing probes in the commercial market have little or no sensitivity to directly measure the potential activity of surface liquid molecules. In comparison, the Ionizing Surface Potential Sensor (ISPS) is a robust and highly sensitive instrument used to measure the electric charge of molecules at the liquid surface.

Although the ionizing surface potential method was first established by Guyot in 1924, researchers at the U.S. Naval Research Laboratory (Washington, D.C.), namely Jarvis and Scheiman[91] and Bewig[92], further developed the method during the 1960s. In their seminal work, Jarvis and Scheiman showed that the ionizing method can be used to measure the surface potential of inorganic electrolytes.[91,93] Ever since, however, there has been no real attempt to reproduce these experiments until now. In this work, we present the concepts behind the ionizing method, the instrumentation, and methodologies developed for precise measurements. Surface potential sensing is a real-time and quantitative method to analyze the electric charge properties of a liquid or solid surface. Surface potential is an important phenomenon as it gives information about the composition and orientation of surface molecules, and the degree of interaction of subsurface molecules with those at the surface.

2.2.1 Principle of Ionizing Surface Potential Method

The ionizing method requires a radioactive source to ionize air molecules in the gap between the reference electrode submerged in liquid and the water surface. In conjunction, a high impedance electrometer is used as the measuring circuit (i.e., indicator). The measurement is thusly made when the input resistance R_i from the measuring circuit is orders of magnitude greater than the resistivity of the fluid media between the radioactive and reference electrodes. Plainly speaking, the fluid media subject to measurement must be within the detection limits of the indicating device.

Figure 2-2 shows two scenarios with an identical equivalent circuit and with identical measuring circuits. In both cases, the R_i of the measuring circuit is equivalent, and the current i is flowing in the circuit, such that the measured potential V_M is directly proportional to the electrostatic potential ϕ of the fluid media. However, under conditions where there is no ionization, the resistance of R_i is far below the resistivity of the media R_ϕ: $R_i \ll R_\phi$. If one considers two metals separated by an air gap of 1-2 mm, one is hard-pressed to detect any voltage changes with an indicator. This is because the resistivity of air ranges between 1.3×10^{16} and 3.3×10^{16} ÿm (20 °C). Over millimeter distances, the resistivity now approaches 10^{19} Ωm. In contrast, R_i of an industry-grade electrometer range around 10^{14} Ωm. In such scenarios, the need for an ionizing electrode becomes apparent. Alpha particles from a radioactive electrode ionize the air gap, and thus reduces its resistivity. It has been previously shown by Foulkes et al.[94] that the resistivity of an ionized air gap ranges between 10^{10}-10^{11} Ωm. It is well within the range of an industry-grade electrometer. Therefore, under an ionizing environment, the $V_M = \phi$.

NO IONIZATION

WITH IONIZATION

Measuring circuit

R_i

i

V_M

R_ϕ

ϕ

$R_V < R_\phi$

$V_M \neq \phi$

R_i

i

V_M

R_ϕ

ϕ

$R_V > R_\phi$

$V_M = \phi$
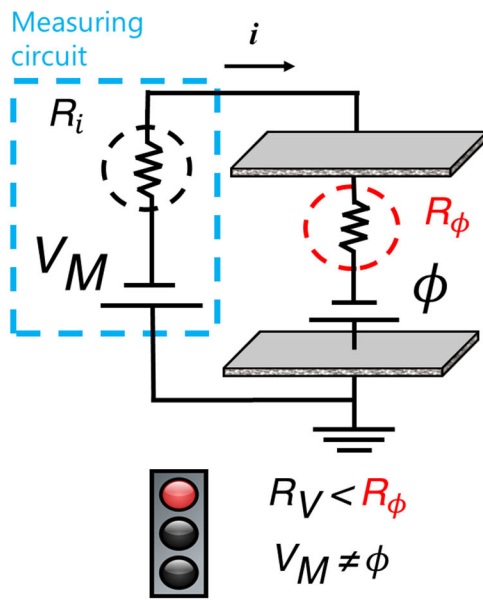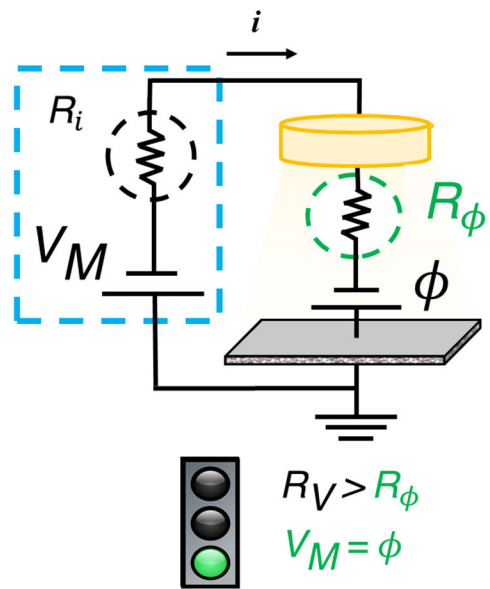
Figure 2-2. Illustration of the ionizing electrode principle. Ionization decreases the high resistivity of the air gap.

2.2.2 Instrumentation

ISPS is a novel and custom-built surface potential sensor based on a radioactive electrode designed to measure surface potentials of electrolyte solutions. Thus, the inspiration in the design of the instrument came first from the description of Jarvis and Scheiman's ionizing cell (a derivative of Guyot's), the known problems with the method as described by Bewig, and the properties of the materials used.

As discussed previously, surface potential sensing can be more problematic at liquid surfaces as there are fewer charged particles near its surface because it is more electrically insulated (high resistivity of air gap above). In fabricating the ISPS, there is the potential overabundance of available materials and various experimental setups. Therefore, what might be required to build such an apparatus that is both safe and convenient to use. From older studies by Kamienski et al., Foulkes et al., and Bewig, we can gain significant insight into the appropriate selection of materials and by adopting certain experimental setups, minimize potential errors.

A significant disadvantage of the technique during the early days was the use of Po-210 to ionize the air, which has a short half-life of 138 days. In 1960, Kamienski et al. used plutonium-239. Initially, a 2 μCi source was used above salt electrolytes, but it was found that the time required to attain steady potential measurements varied between 3-25 mins. Later, Kamienski and co-workers increased the activity of the alpha particle source to 20 μCi. This resulted in greatly reduced time and permitted measurements over much larger air gaps. As the most essential and expensive part of the ISPS, the selection of the radioisotope electrode required the most care. Given its ease of access and use, the americium-241 (Am-241) radioisotope was selected for the studies in this dissertation. An advantage of Am-241 over Po-210 is its extended half-life, whereby a constant flux of alpha radiation is sustained over longer periods.[95,96]

The ISPS utilizes an Am-241 radioisotope as an alpha particle source electrode suspended in the air. The schematic of the electrochemical system and the experimental setup is shown in Figure 2-3. The Am-241 isotope-based electrode was custom-ordered and purchased from Eckert & Ziegler Isotope Products Inc. The Am-241 itself is incorporated into a gold matrix that is incorporated into rolled foiled with an aluminum backing. It boasts a 9.5 mm active diameter and 740 kBq (20μCi) activity, which is a suitable radioactivity for fast response times. The side opposite active has a precision cut thread that can be fastened with a copper screw. The copper screw serves as the point of connection from the Am-241 electrode to the electrometer.

Submerged in liquid is a platinum gauze counter electrode, which is resistant to corrosion from electrolytic solutions. The platinum gauze electrode (99.95% purity, CH Instruments) utilized is commercially available and replaces part of the ISPS. With a surface area of 25 by 35 mm, the Pt gauze (once placed in the solution) is positioned parallel to the Am-241 electrode (at least 15 mm apart). The entire setup is enclosed in a Faraday cage (Thorlabs, NJ). Voltage was measured with a high input impedance Keithley 6517b electrometer (Tektronix/Keithley) through a triaxial cable connected to both electrodes. Real-time compilation of voltage data was collected using a custom-designed program through the LabVIEW (National Instruments) software.

With these implements, a working ISPS prototype was assembled, tested, and validated with palmitic acid surfactant monolayers.[97] Unfortunately, this prototype did not meet the benchmark reproducibility of measured potentials for electrolytic solutions due to contamination. The open-environment cell design of the prototype had samples exposed to contaminants from the environment. Moreover, the open environment around the Am-241 electrode was observed to be further susceptible to capacitive interference from nearby conductive surfaces. As initially pointed out by Bewig[92], potential sources of fault with ionizing electrodes, which can arise with scattered ionization from an unshielded radioactive electrode. Scattering can cause currents to

flow from the air electrode to other nearby surfaces (e.g., surrounding enclosure, the experimenter handling the apparatus), which results in additional voltage from sources apart from the water surface. Thus, minimizing these errors requires insulation of the air electrode mounting. Moreover, the spacing between the electrodes must also be somewhat protected such that the ionization is solely concentrated into the air gap. For the ISPS, these faults were addressed through a redesign of the original prototype, and thus currently utilizes PTFE as an electrically insulating shield around the Am-241 electrode and the space around the air gap. (Figure 2-4)

As shown in Figure 2-5 and 2-6, the positions of the electrodes were fixed within a custom-cut PTFE holder with the PTFE enclosing the experimental space. This includes covering the entire solution surface while providing insulation for the Am-241 electrode to reduce stray capacitance from neighboring conductive materials. The air space above the solution was gently lushed (0.7 L/min) with ultra-high purity nitrogen (99.999% purity, Praxair) at standard pressure prior to placement of the sample (Figure 2-7). Despite these precautions, future experimenters must be wary of other sources of error that can lead to inaccurate measurement during measurement. These are discussed in some detail in the next section.

a.

Working Electrode (WE)

gas

gas-liquid interface

liquid

Counter Electrode (CE)

b.

Am-241

N$_2$ gas

air-solution interface

V_m

NaCl solution

electrode-solution interface

Pt gauze
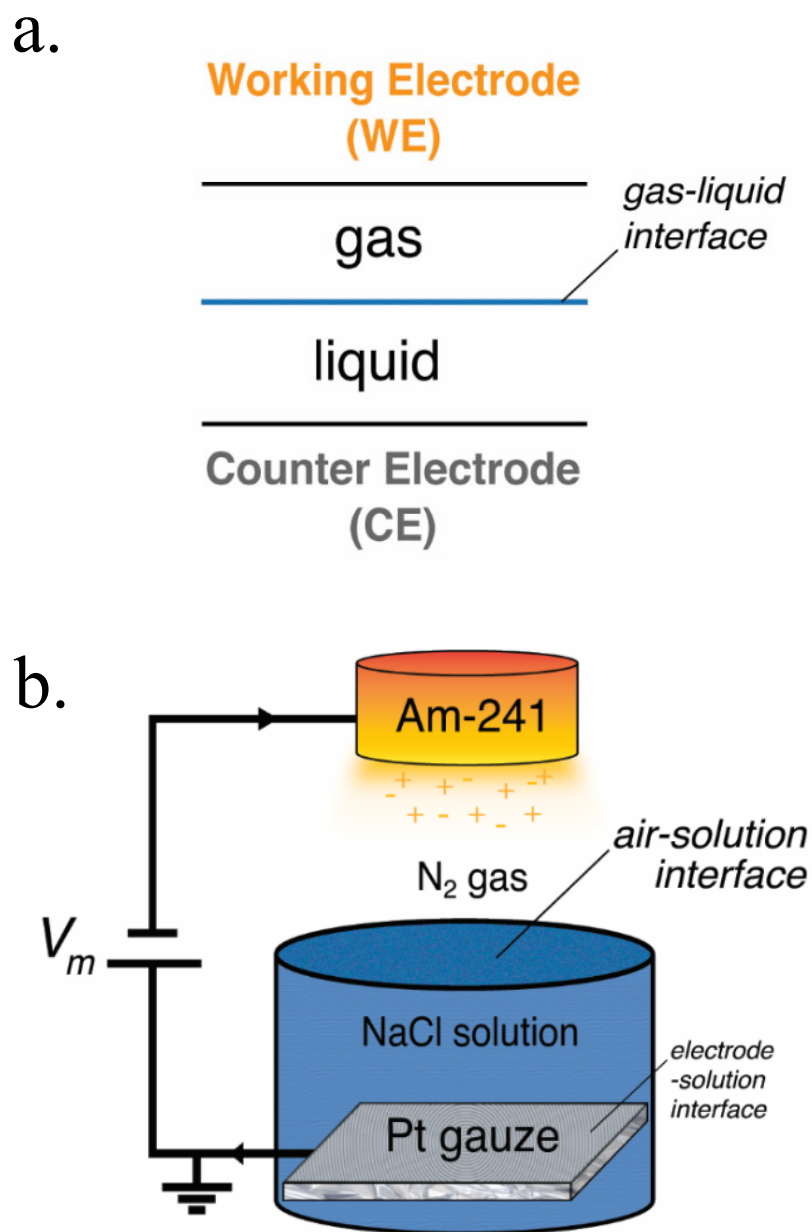
Figure 2-3. Schematic of the (a) electrochemical cell, and (b) experimental setup of the Ionizing Surface Potential Senor (ISPS) that is proven to be extremely sensitive to electrolytic solutions.
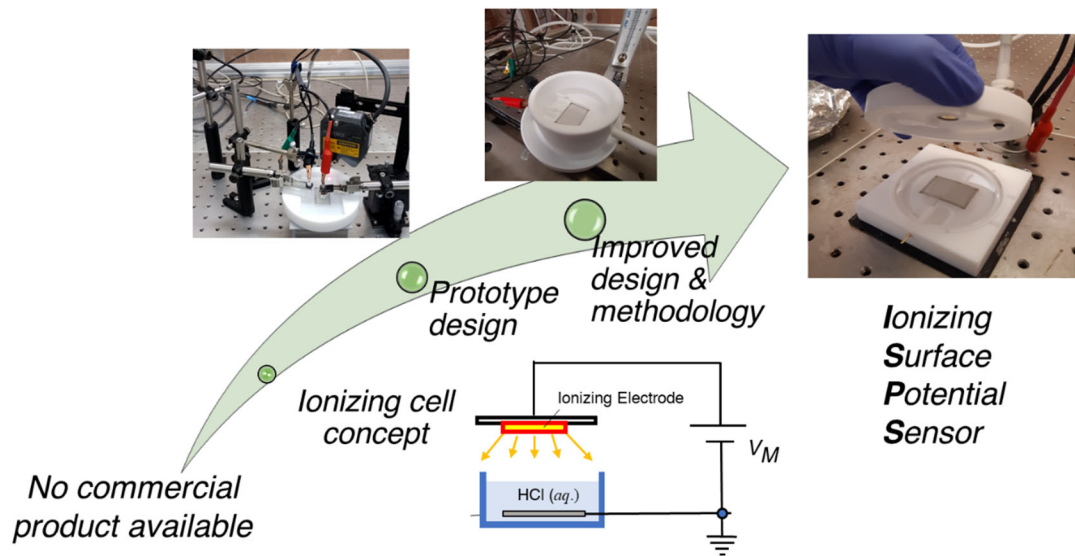
Figure 2-4. Overview of the design process behind Ionizing Surface Potential Sensor (ISPS).
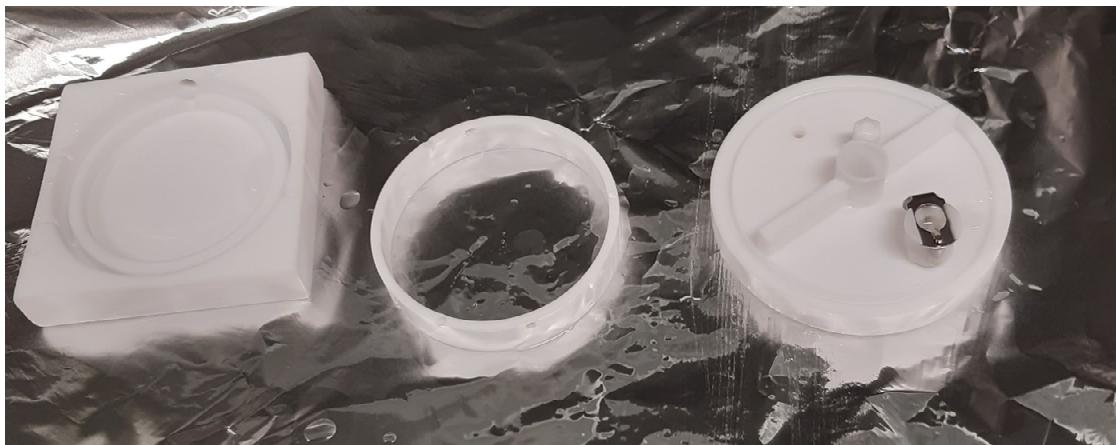
Figure 2-5. Ionizing cell (PTFE) used to house the Am-241, Pt gauze electrode, and liquid samples. From left to right: Left piece is the bottom square used to house the Pt gauze and sample. Middle piece is a clamp for the Pt gauze and to prevent leakage from the cell. Far right piece is the top piece that holds and shielding the Am-241 from its surrounding. An inlet is also present for N_2 gas flow in chamber above the liquid samples. A hole is also present for even exchange of N_2 with air and helps avoid any turbulence due to slight pressure differences.
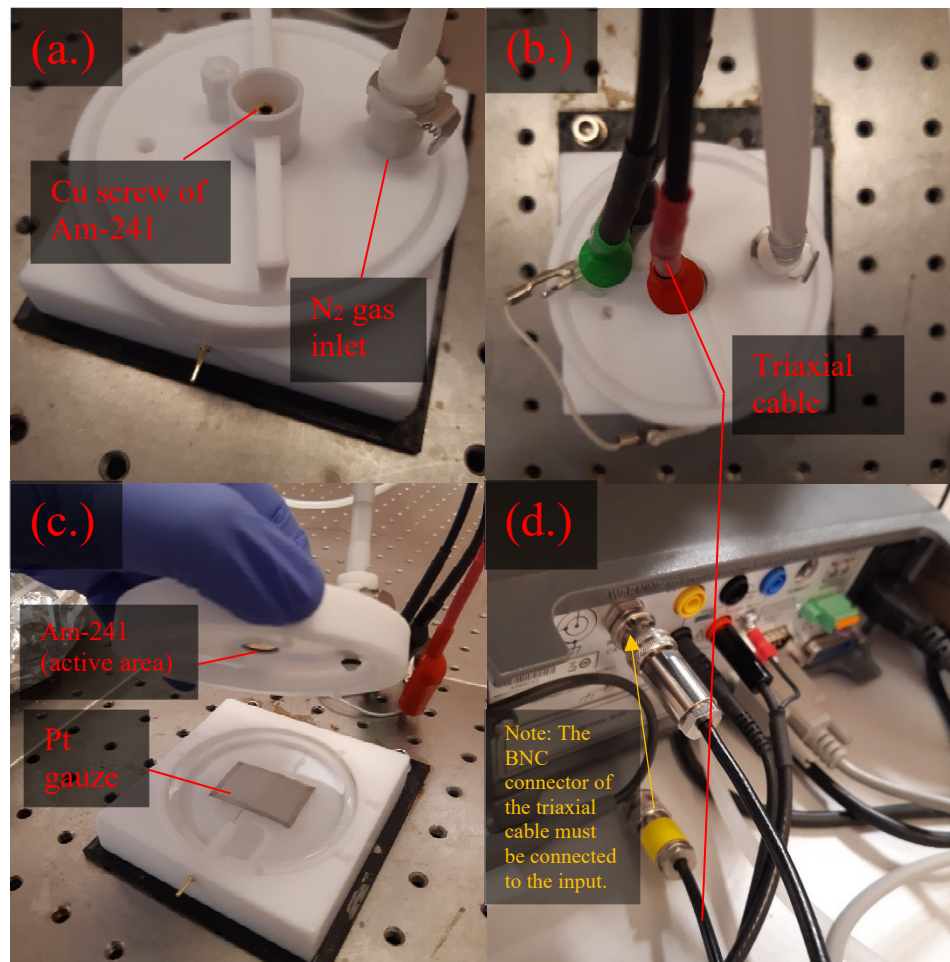
Figure 2-6. Detailed schematic of the ionizing cell in use. (a.) N_2 gently flushes the ionizing chamber following the placement of liquid sample. (b.) Electrodes are connected to the respective electrodes as follows: High-V (red) is connected to the Am-241. Low-V (black) and ground (green) are connected to a second connector wire that is directly clamped to the Pt gauze. (c.) Wires are disconnected when handling electrolytes or moving the cell. (d.) Back panel of the Keithley 6517b electrometer (Tektronix/Keithley) shows the triaxial connection from the cell.
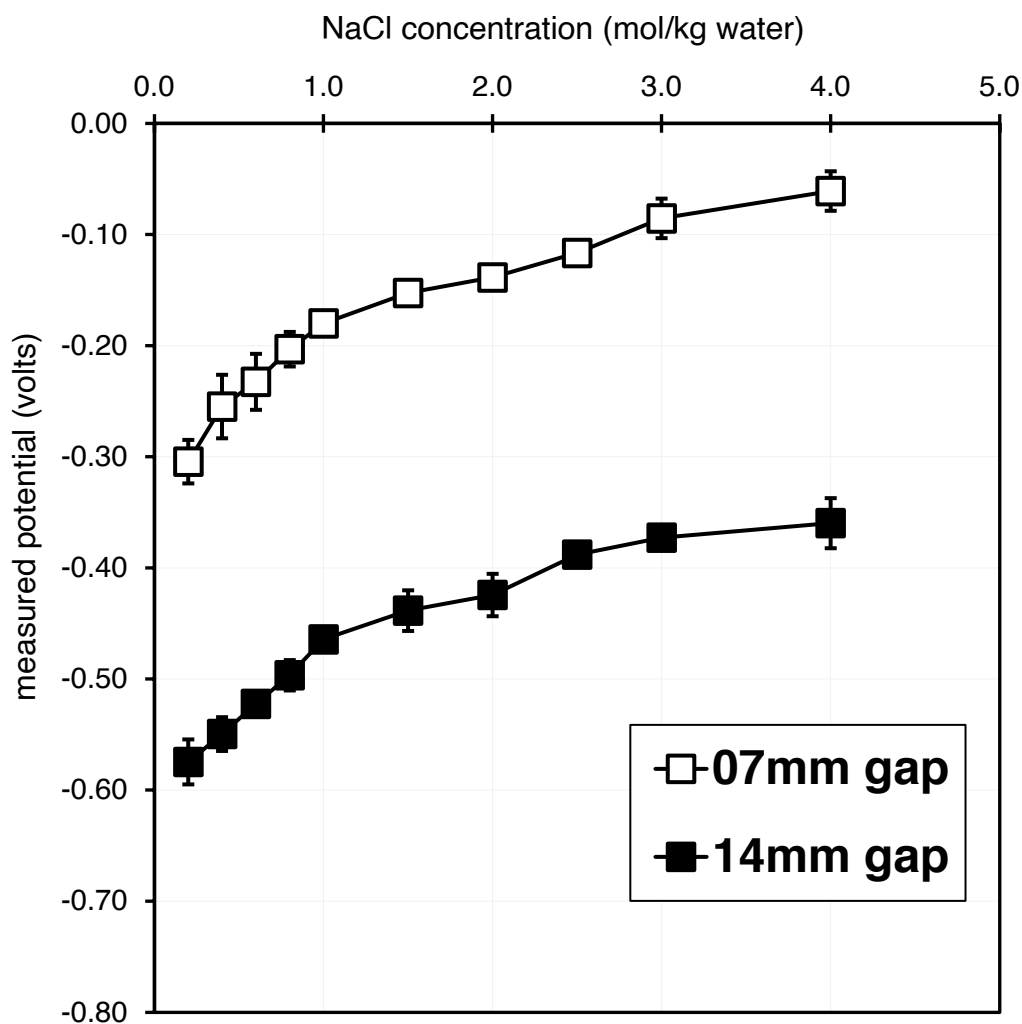
Figure 2-7. The measured potential (volts) is plotted against aqueous NaCl concentrations (mol/kg water). In order to minimize electrical interference from dissolved CO_2 and O_2 during measurement, the aqueous NaCl were degassed for 25 to 35 minutes using argon (99.998% prepurified, Praxair) up to 2 minutes before ionizing surface potential measurement. The gap of 7 mm (open) and 14 mm (filled) between the Am-241 and the solution surface influences the measured potential (capacitance). For optimal coverage of ionizing flux over the solution surface, the 7 mm gap was selected as the ideal for all measurements within or in relation to this work. Lines indicate trends only.

2.2.3 Additional Experimental Methods

Measuring surface potentials is often a tedious measurement due to the susceptibility to contaminants at the water surface. For precise measurements, several additional experimental measures must be put in place, especially as it involves aqueous inorganic electrolytes. The respective cleaning methods used with every salt are outlined in the Methods section for this dissertation. For other salts, the aqueous salt purification has been outlined by Hua et al.[52] In this work, as summarized in Figure 2-8, the error bars are reduced with the combined effort and precautions of surface-level cleaning. The use of aspiration methods and degassing has been previously shown to reduce trace organic contaminants from the surface.[98] Combined with cyclic voltammetry cleaning of the counter electrode (either Pt or Au gauze)[99,100], a necessary action with the ionizing method, allows for good reproducibility and reduction of erroneous results. More details are available in Appendix F.
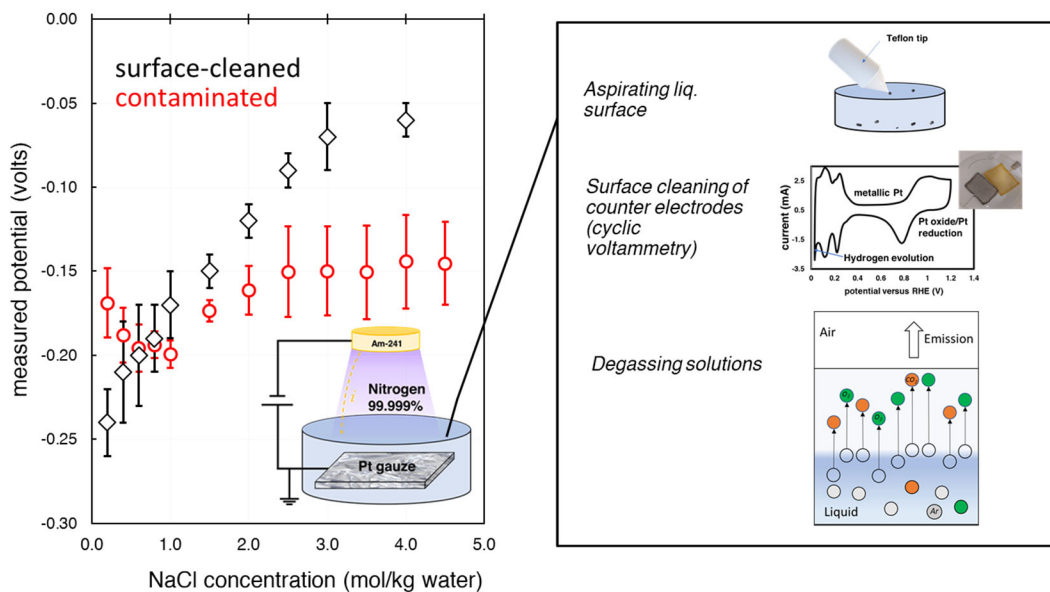
Figure 2-8. Additional cleaning procedures used with ionizing surface potential.

2.3 Ionizing Method vs. Other Electrochemical Surface Potential Methods

For the air–solution interface, the surface potential is commonly measured by three electrochemical techniques. such as the capillary drop method (also called liquid flow method)[84,101–104] and the ionizing electrode method.[91,105] Unlike the more dynamic liquid flow method, the ionizing method is a simpler two-electrode electrochemical setup. The uniqueness of the ionizing method is the use of a radioactive working electrode suspended in air, in conjunction with an inert Pt gauze reference/counter electrode submerged in the electrolyte solution. Previous work by Frumkin[101], Randles[84,102,103], and Jarvis and Scheiman[91] utilized a radioactive working electrode to measure the surface potential of aqueous salt solutions.

The vibrating plate method (Kelvin-Zisman Probe) employs a vibrating plate to detect changes to the capacitance (voltage) between two materials.[106,107] Despite its commercial availability, detection of surface potentials is often limited to interfaces containing surfactant monolayers. Unlike either the vibrating plate or ionizing cell, the Kenrick cell or liquid jet method (also called capillary drop) has been used almost exclusively to measure surface potentials of aqueous interfaces. The basic principle of Kenrick's liquid jet involves a stream of liquid directed down a side of a glass tube, parallel to a "stream" of liquid mercury. Over time, the ψ between the two streaming liquids becomes constant. Thus, α_i is measured indirectly with a high-impedance electrometer connected to the two liquids by their respective reference electrodes. However, the liquid jet is susceptible to errors arising from improper insulation of the liquid mercury and the static charging of the glass tube.[107]

Compared to the liquid jet, the ionization method experimentally establishes $\psi = 0$ by ionizing the gas in between a metal reference electrode and a stationary liquid surface. As with the liquid jet method, a high-impedance electrometer is used to measure $\tilde{\mu}_i = \alpha_i$. Sources for ionizing radiation typically involve alpha particle emitters such as Polonium-210 (Po-210) and

23

Americium-241 (Am-241).[107,108] An advantage of Am-241 over Po-210 is its extended half-life, whereby a constant flux of alpha radiation is sustained over longer periods.[95,96]

Figure 2-9. Overview of the differences in electrochemical surface potential techniques underscoring their respective advantages and disadvantages.

2.4 Experimental Controls and Calibration Measures

Subsequent to solvating ions in water, there is a redistribution of electrical charge at the air/water interface owing to the unequal adsorption of oppositely charged ions, the adsorption and orientation of water molecules, and anisotropic solvation of polarizable ions interacting with the uneven electric field of the air–water interface itself.

2.4.1. Impact of Ionizing Environments

With the ionizing surface potential method, the strength of the radioactive electrode, the volume of the air gap, and the type of gaseous environment can impact the measured potential.[92,94] Figure 2-10 shows the measured surface potentials for cetyltrimethylammonium bromide (CTAB) and sodium dodecyl sulfate (SDS) in three different ionizing gas phase environments of helium (He), nitrogen (N_2), and argon (Ar).

Assuming a steady flux of alpha particles emitted by our (Am-241 electrode, we estimated the extent of gas ionization from known averages of energy required to produce an ion pair for each gaseous environment (Table 2-1).[94,109] The percentage of ionized particles available within the same volume of gas correlates with the order of the molecular mass of the gas: He < N_2 < Ar (Figure 2-11). From the results in Figure 2-10, there is a larger impact on the χ_{CTAB} by the heavier Ar compared to N_2 and He. The appreciable differences in the electric potential within each of the gas-phase environments are based on physical factors that relate to the nature of the gas itself. As investigated in our previous study, variation in the dielectric constant of the gaseous environment is a factor shown to affect the capacitance across the Am-241 electrode and electrolyte solution surface.[96] Additionally, the distinct ionization energies of these gases significantly impact the distribution and strength of the ionization field.[110] Although there is the probability that heavier molecules at the aqueous surface might be ionized,[108] is unlikely given

the weak radioactivity of our Am-241 electrode (at 20 μCi) and large width of the gaseous slab above the aqueous surface[94,96].

   Estimating the Ionization of Inert Gases. As alpha particles pass through a gaseous slab, there is sufficient kinetic energy to produce ionization by collision. This results in the formation of ion pairs, which is often the ejected electron and the positively charged atom. Given that the kinetic energy of the ejected electron is equivalent to the energy lost by the first particle, the resulting ionization potential of the atom is comparatively smaller.[111] This means the ejected electron may have sufficient kinetic energy to cause secondary ionization of gaseous molecules, where the resulting ionization might be several times larger than the first event.[111,112] Therefore, following a simple calculation by Foulkes *et al.*[94], we determine the extent of ionization for three gases (He, N_2, Ar) to understand their effect on measured surface potentials.

   Given the activity of our source at 20 μCi, there is an estimated 7.4E+05 alpha particles emitted per second. Also, considering the dimension of the cylindrical space (dia. 73.1 mm, depth 7 mm) above the aqueous surface, and the relationship of gas volume to the particle of gas (at the conditions specified above), we estimate the number of gas molecules within this space to equal 7.3E+20. Hence, the *number of ion pairs formed per collision with an alpha particle* can be determined from the ratio of the alpha particle energy (5.6 MeV for the Am-241) and the *specific energy per ion pair*[109] for each of the different gases. Factoring Rutherford's constant[113] on the rate of recombination of ion pairs (n = -1.6E-6 ions/cm^3) and the *total number of ions formed per second*, the steady-state concentration of ions (n) can also be estimated from the following equation:

$$n = \sqrt{\frac{N_0}{\alpha}} \qquad (2.4)$$

where N_0 is the *total number of ions formed per second* divided by volume (in cubic meter), which indicates the "current" in the system. Separately, the percentage of ionized gas molecules

26

in the environment is calculated from the ratio of the *total number of ions formed per second divided by volume* to the estimated number of gas molecules.
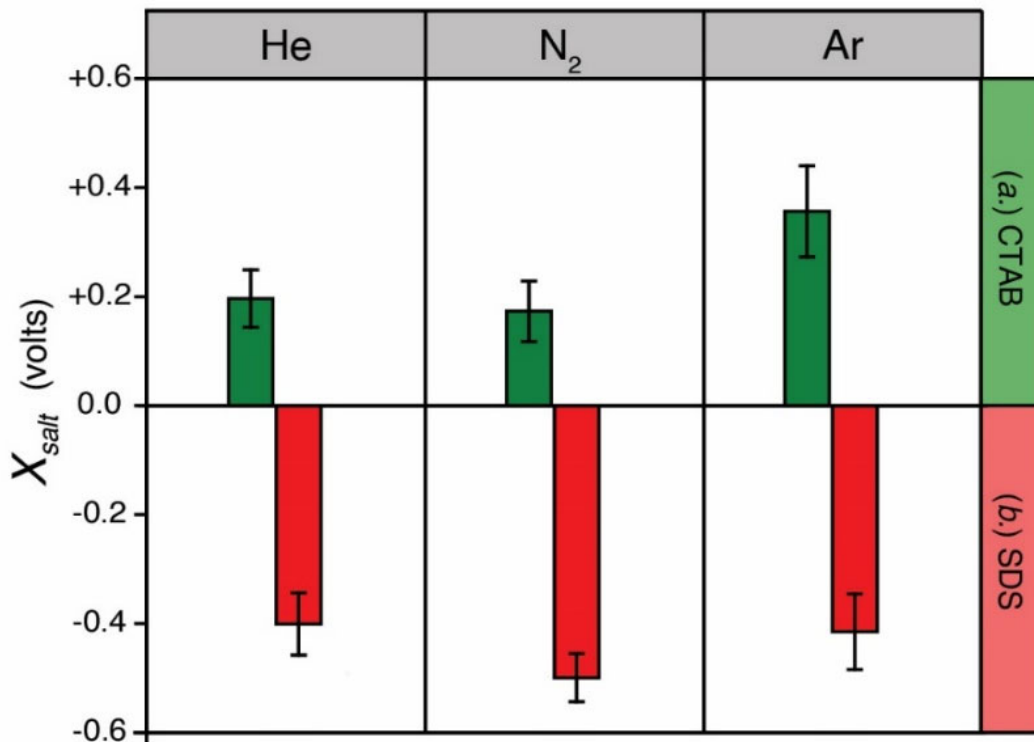
Figure 2-10. Surface potentials of (a.) cetyltrimethylammonium bromide (CTAB) and (b.) sodium dodecyl sulfate (SDS) are measured separately in different ionizing gas phase environments of helium (He), nitrogen (N_2), and argon (Ar) against a fixed position of the Am-241 and Pt gauze electrodes. The gas flux above the solution and solution temperature (295 K) remained constant. Prior to dissolution of CTAB and SDS crystals, the ultrapure water was degassed for 25 to 35 minutes using argon (99.998% prepurified, Praxair) up to 2 minutes.

Table 2-1. Gas dependence of the number of ion pairs, and ions formed either per alpha particle or second, respectively. Energy per ion pair potentials was taken from Harris & Doust [ref. [109]] and are specific to alpha particles emitted from an americium-241 source.

Inert Gas	Energy per Ion Pair (eV)	Number of ion pairs formed per alpha particle, x10^5	Total number of ions formed per second (s^{-1})	Steady-state concentration of ions per cm^3, x10^{10}	Percentage of ionized particles (%, x10^{-32})
Helium (He)	43.5	2.1	2.3E+10	3.5	1.9
Nitrogen (N₂)	36.4	1.5	3.2E+11	7.0	3.8
Argon (Ar)	26.3	1.3	5.7E+11	8.2	4.5
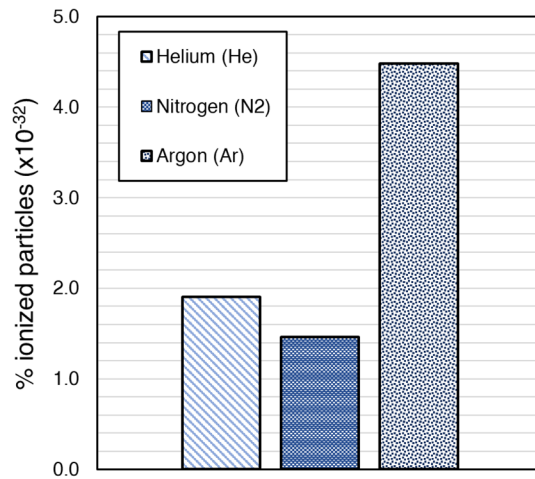
Figure 2-11. Graphical summary on the extent of ionization (percentage of total gaseous particles) by Am-241 in the ISPS cell.

2.4.2 Platinum vs. Gold

In consideration of the large difference in our $\Delta\chi$ compared to the earlier studies, we submit that the choice of the reference electrode is the most probable cause for these magnitude differences. The selection of a Pt gauze electrode in our cell, as opposed to a calomel or Ag-AgCl reference electrode, means there is an increased sensitivity to measuring changes in the DC electric field. Such differences are contingent on the nature and structure of the submerged electrode and other factors that influence electron transferability, particularly the interaction of species on the electrode surface.[99]

As shown in Figure 2-12, the χ_{salt} for aqueous NaCl was measured independently with a Pt and gold (Au) gauze under the same experimental conditions (see Supporting Information for experiment details). Of note, the χ_{salt} with the Au gauze is between 2.2 to 2.8 times the measured potential with Pt under the 1.0 M condition. The lower potential response for the Au/N$_2$ indicates a higher resistivity due to greater charge retention at the Au surface compared to Pt.[96,99] Moreover, contrasting their current exchange properties (overpotentials for hydrogen evolutions) to another metal such as mercury (Hg) which is present in calomel electrodes, Pt and Au demonstrate up to an order of magnitude more efficient in transferring electrons across their solution-electrode interface.[114]

Both Figure 2-13 and Figure 2-14 show the relative impact of Pt and Au gauze electrodes are used separately as the reference electrode submerged in ionic surfactants and aqueous NaCl, respectively. Measured surface potentials of the 0.3mM CTAB and SDS are measured separately in different ionizing gas/counter electrode environments. The results above compare the impact of the ionizing gas relative to the counter electrode (Pt vs. Au). It appears the Au/ N$_2$ has a greater impact on both surfactants relative to the ionizing environment. Experiments were performed against a fixed position of the Am-241 and counter electrode (15 mm apart),

whilst the gas flux above the solution and solution temperature (295 K) remained constant. The Pt/N$_2$ (blue triangles), Au/N$_2$ (red circles), Pt/Ar (green circles) shows the potential is proportional to the salt concentration, thus indicating that the salt behavior is relatively consistent despite the change of environment. The nature of the counter electrode has a greater effect on the value of the measured potential compared to the effect from the different counter electrodes. Although both gas and counter electron have a significant impact on the magnitude of the measured surface potential (volts), the signs of the measured potentials are consistently negative.
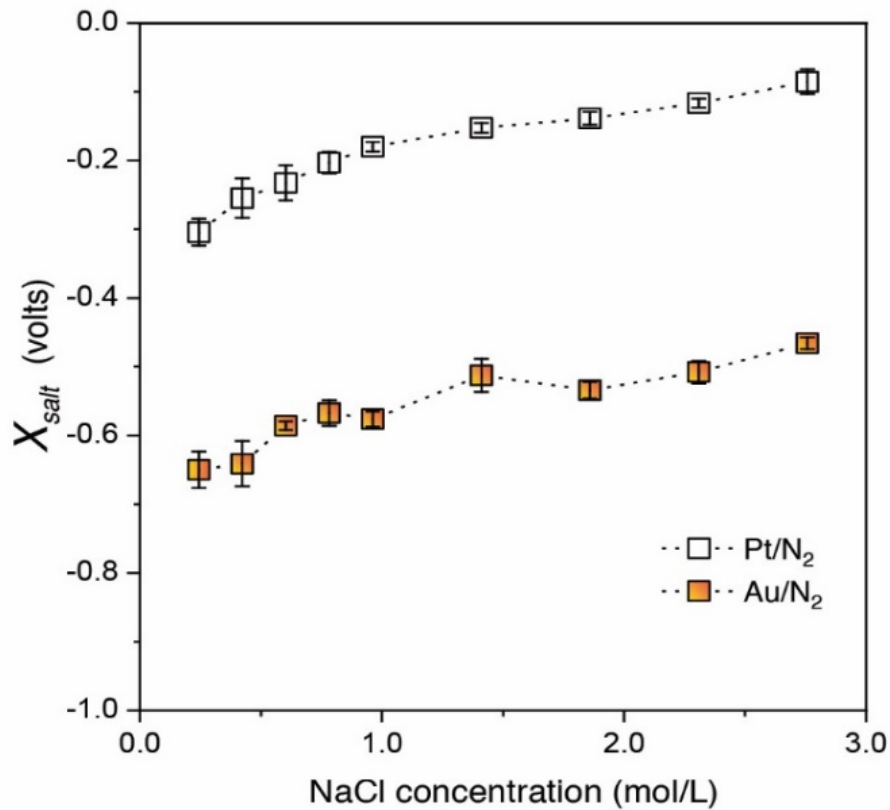
Figure 2-12. Platinum (Pt) and gold (Au) gauze electrodes are used separately as the reference electrode submerged in aqueous NaCl. Nitrogen (N_2) flux above the solution and solution temperature (295 K) remained constant. Dotted lines indicate trend only. In order to minimize electrical interference from dissolved CO_2 and O_2 during measurement, the aqueous NaCl were degassed for 25 to 35 minutes using argon (99.998% prepurified, Praxair) up to 2 minutes before ionizing surface potential measurement.
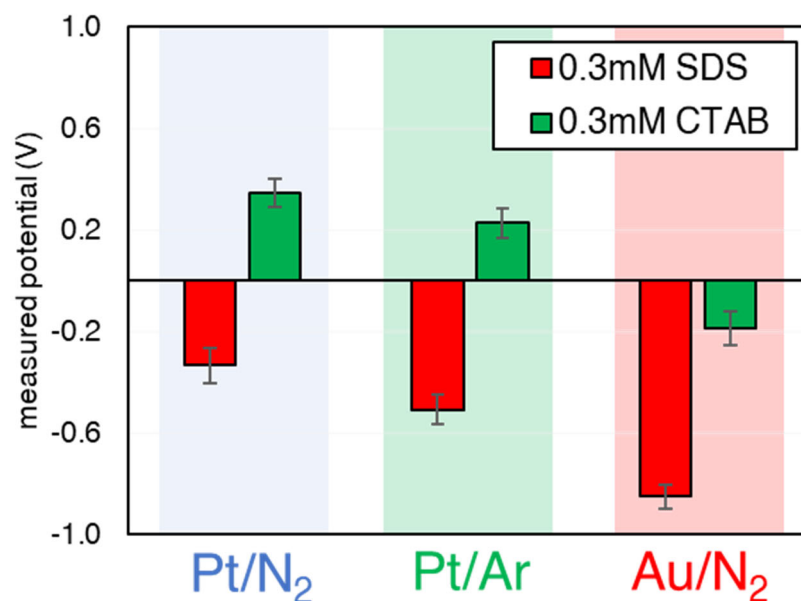
Figure 2-13. Surface potentials of 0.3 mM cetyltrimethylammonium bromide (CTAB) and sodium dodecyl sulfate (SDS) are measured separately in different ionizing gas/counter electrode environments. The results above compare the impact of the ionizing gas relative to the counter electrode (Pt vs. Au). It appears the Au/ N_2 has a greater impact on both surfactants relative to the ionizing environment. Experiments were performed against a fixed position of the Am-241 and counter electrode (15 mm apart), whilst the gas flux above the solution and solution temperature (295 K) remained constant. Prior to dissolution of CTAB and SDS crystals, the ultrapure water was degassed for 25 to 35 minutes using argon (99.998% prepurified, Praxair) up to 2 minutes.

Figure 2-14. Pt and Au gauze electrodes are used separately as the reference electrode submerged in aqueous NaCl. Blue triangles and red circles represent the Pt/ N_2 and Au/ N_2 environment, respectively. Green circles represent the Pt/Ar environment. Although both gas and counter electron have significant impact on the measured surface potential (volts), the nature of counter electrode has the greater relative effect. Gaseous flux above the solution and solution temperature (295 K) remained constant. Dotted lines indicate trend only. The aqueous NaCl were degassed for 25 to 35 minutes using argon (99.998% prepurified, Praxair) up to 2 minutes before ionizing surface potential measurement.

Chapter 3. Circuit Analysis of Ionizing Surface Potential Method

3.1 Introduction

Understanding the potential difference across the gas–liquid interface, also referred to as the surface potential of the gas–liquid interface, is often obscured by the numerous techniques used to quantitatively measure it. Even for the simplest interface, such as the pure water/air interface, the reported surface potentials are disparate and debated in the literature.[3,4,115–117] This has led to some disagreement over the data treatment methodology and accuracy of the electrochemical techniques used to measure the surface potential of liquid surfaces.[4] An analysis of the surface potential can be expected to offer a molecular picture of the electrostatic interactions of charged and neutral species at liquid surfaces[88], which has implications for the fundamental chemical and electrochemical processes in atmospheric chemistry, biochemistry, and technology.

Electrochemical measurements such as the measured surface potential V_m directly relate to macroscopic thermodynamic properties such as the surface electric potential χ, which is proportional to the electric dipole moment μ at the real gas–liquid interface.[85] However, χ is also related to the net charge distribution of molecules across the thickness of the gas–liquid interface.[3,4] Indeed, χ can be related to the dipole and quadrupole moments.[3,4,68,83] In measuring the potential difference across two phases, intrinsic features of the interfacial structure,

particularly the orientation of molecular dipoles and intermolecular interactions of surface molecules, are observed. To the same degree as surface tension is a direct measure of the magnitude of the interfacial intermolecular forces, the surface electrical potential of the gas–liquid interface is a measure of the net distribution of the molecular dipoles and quadrupoles at the liquid surface.[4,68,81,85] Thus, measuring the surface potential at the air–aqueous interface is directly relevant to the real free energies of hydration of solvated ions.[84,88]

Experimental studies by Frumkin[101] and others[84,91,102–104] describe a surface potential change with increasing concentrations of salt electrolytes at the air–water interface. Additionally, theoretical studies are correlated to the experimentally measured surface potential changes of these electrolytes.[35,118] The addition of small quantities of salt electrolytes involves the formation of different interfaces (e.g., the electrode–electrolyte, air–electrolyte) and gives rise to an electrical double layer at each interface. This electrical double layer at an interface results from layer(s) of preferentially oriented dipole moments and the differential adsorption and desorption of ions.[119,120] Various interfacial characteristics are expected to be principally related to the ion constituents and thus to ion size and ion-solvent interfacial structure.[119,120] In dilute solutions, the potential across the double layer is expected to decrease exponentially at a thickness similar to the Debye radius for an ionic atmosphere. As a result, the total potential difference measured between two electrode terminals describes all the ensuing interfacial double layers including the double layer at the air–water interface, dominated by the surface potential of the air–water interface.[3,81,85]

For the air–solution interface, the surface potential is commonly measured by electrochemical techniques such as the liquid flow method (with[84,101–103] or without a radioactive electrode[104]) and the ionizing electrode method.[91,105] Unlike the more dynamic liquid flow method, the ionizing method is a simpler two-electrode electrochemical setup. The uniqueness of the ionizing method is the use of a radioactive working electrode suspended in air, in conjunction

with an inert Pt gauze reference/counter electrode submerged in the electrolyte solution. Previous work by Frumkin[101], Randles[84,102,103], and Jarvis and Scheiman[91] utilized a radioactive working electrode to measure the surface potential of aqueous salt solutions. However, these reported surface potentials are measured electrochemical potentials corrected from an extrapolated value, often referred to as the surface potential of pure water.[91,102,104] Moreover, these prior measurements are obscured by an underdeveloped understanding of the influence of physical experimental parameters, such as the type of radioactive source (Po-210 or Am-241) and spacing between electrodes (a known factor affecting potential measurement[105]), in measuring the potential drop across the electrochemical cell.

In this study, we directly compare real electrochemical potentials using an electrochemical setup similar to Jarvis and Scheiman, which consists of a custom Am-241 ionizing working electrode (as shown in Figure 2-1) and a Pt gauze counter reference electrode to measure the surface potential of pure water and two sodium salts of 1.0 M concentration. We also present a circuit model to characterize the ionizing electrode, which is actively generating gas-phase ions (or a beam of radiation) that determines the total current in the circuit.[94,113,121] The quality of this beam depends on the radioactive source and the distance between the electrodes (Appendix A). Analyzing the real-time potentials using this model, we directly validate real electrochemical potentials from the ionizing surface potential method to predict well-established surface tension values for aqueous electrolytes.

3.2 Materials & Methods

3.2.1. Sample preparation

Sodium chloride (99+% for analysis, ACROS Organics) and sodium sulfate (99+% for analysis, ACROS Organics) were heated in air to 600 °C in a furnace overnight to remove trace organic residue from salts crystals.[52] Electrolyte solutions were then prepared in glassware

previously cleaned with piranha solution (3:1 sulfuric acid with hydrogen peroxide) by dissolving room temperature heat-treated salts in ultrapure deionized water (>18 MΩ.cm, Milli-Q). Solution surfaces were purified by repeated aspiration of stirred solution with a PTFE tip before measurement.[98] Glassware containing solutions were covered with aluminum foil to minimize exposure to light and dust. Solutions were measured within 30 minutes of preparation. Data were collected at 295.15 K ±0.1 and 26.2 ±2.8 relative humidity of the room.

3.2.2. Methods

Prior to cell assembly, the PTFE holder (of the ionizing cell) and Am-241 electrode were rinsed several times with ultrapure water and fully dried under pure nitrogen gas. Separately, Pt gauze was cleaned by cycling in 0.1 M perchloric acid solution (99.999% trace metals basis, Sigma Aldrich) at >50 sweeps, from -0.6 V to +1.8 V at 100 mV/s, until electrochemical features indicating a clean Pt surface was obtained. The cleaned Pt gauze was then rinsed several times with ultrapure water before cell assembly. The solutions placed in the freshly cleaned PTFE holder were equilibrated to the nitrogen gas environment for at least 30 seconds before data collection. The circuit is closed for measurement at t = 0. Ultrapure de-ionized water was measured prior to salt solutions.

The surface potential over time was measured under experimental conditions for pure water, 1.0 M NaCl, and 1.0 M Na_2SO_4 (Figure 3-1). The measured potential (V_m) is assumed to be directly proportional to the surface electric potential (χ) at the air–solution interface. From these temporal experiments, a reproducible exponential decay is observed within the first 30 seconds from an initial potential value of -0.059 ± 0.007 V before plateauing.

3.2.3. Modelling and Regression Analysis

Real-time voltage data were analyzed and fitted to models using scripts written in Python 3.8.5 through Spyder IDE (version 4.0.1) with the *SciPy* package (version 1.5.2) for nonlinear least-squares fitting (Levenberg-Marquardt).[122] Origin 2018 software was used for plotting all graphical figures. The Python code used is available in Appendix C of this work.
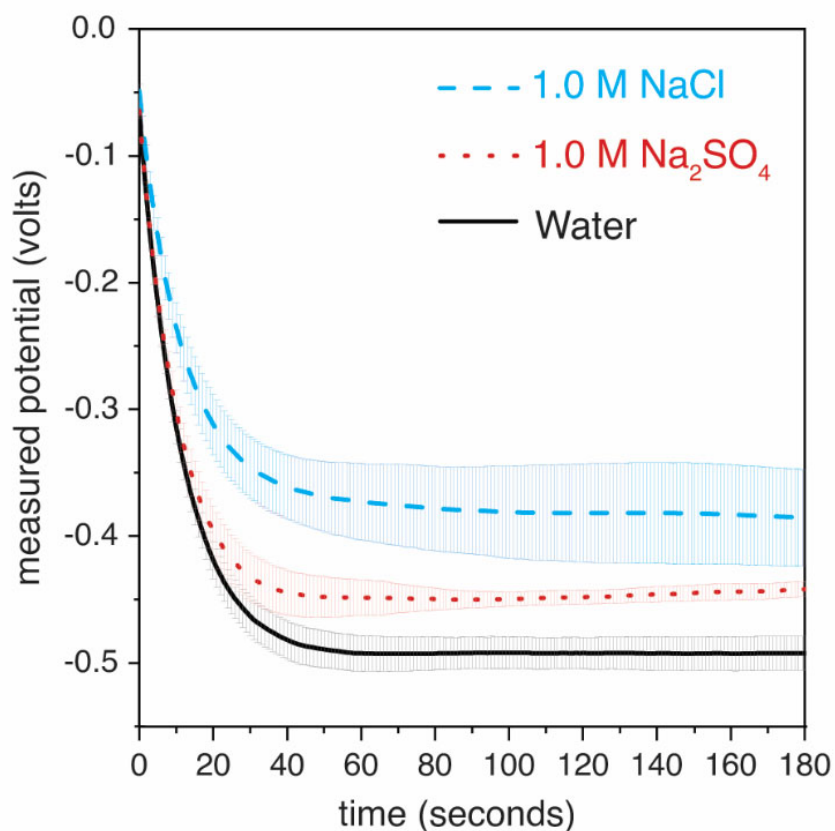
Figure 3-1 Measured potentials (volts) over time (seconds) for (a.) 1.0 M NaCl (dashed -) and (b.) 1.0 M Na$_2$SO$_4$ (dotted …), and (c.) ultrapure water (solid —). Error bars (shaded areas) show that one standard deviation is between 0.01-0.04V.

3.3 Development of the Circuit Model

An equivalent circuit model has often been used to simulate the physical elements involved in an electrochemical system. For the ionizing electrode method, a basic equivalent circuit analysis was described previously by Bewig[92]. As described previously in Bewig's measurement, the measured potential V_M is equivalent to the potential difference across the two electrodes of ionizing surface potential setup. Therefore, the entire electrochemical system is merely represented by two circuit elements: one capacitor and one resistor connected in series. However, the Bewig model is specific to measuring surface potential between two metal surfaces in an ionized gas environment.

In our study, the potential measured varies extensively from that of Bewig due to the unique characteristics of the liquid phase and the solution/Pt gauze interface. Therefore, we propose an ionizing cell model (Figure 3-2), where the capacitance and resistance of the aqueous surface and the bulk solution are taken into consideration. While this model is largely based on an electrified interface theory outlined by Bard and Faulkner[99], Bockris[123], and Parsons[81], our model is more comprehensive as it features non-ideal experimental factors such as the ionization of N_2 molecules and the internal resistance of the Pt gauze electrode, of which the latter is typically not addressed in electrochemical systems. Accounting for the steady flux of ionized particles (i.e., the total current in the system) renders a more accurate model as the number density of gas-phase ions can diminish the high resistivity of the air gap above the liquid.[94]
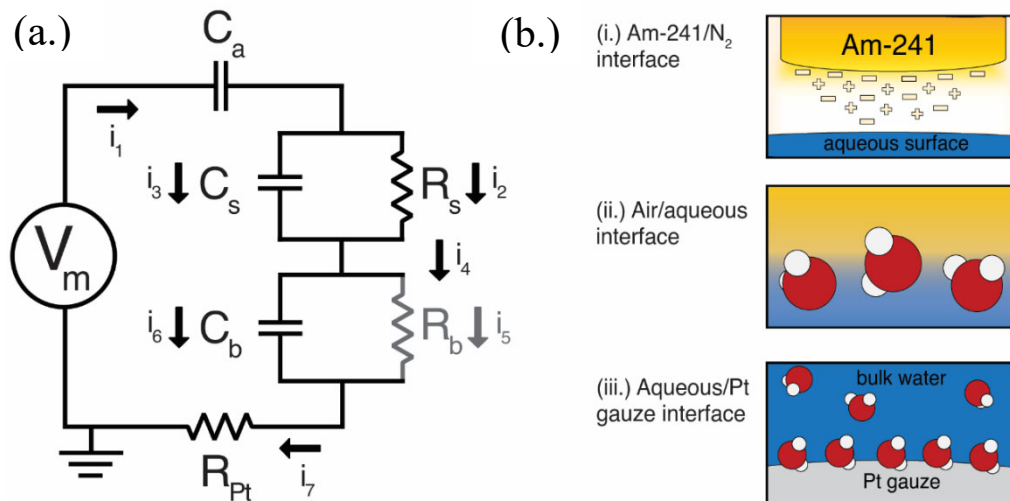
Figure 3-2. (a.) Modified equivalent circuit for the ionizing method electrochemical system in our study. R_b and i_5 (grey) is not included in our regression analysis (Appendix B). (B.) Schematic illustration of the possible molecular interaction at the three different interfaces: (i.) N_2 is ionized by alpha particles giving rise to a substantial capacitive charge C_a at this interface. (ii.) H_2O molecules and ions (not shown) gives rise to an electrical double layer described by a capacitor C_s and resistor R_s. (iii.) H_2O molecules and ions (not shown) from the bulk phase water interact with the Pt surface and is described by the C_b and R_b. Assuming the water molecules form a stable and organized structure on the surface of the Pt gauze, the aqueous/Pt gauze boundary is strongly capacitive. R_b is nearly negligible in this system.

3.3.1 Assumptions in the Circuit Model

As the Am-241 electrode is radioactively decaying, the assumption that it behaves as a typical DC source is oversimplified; the measured potential V_M from the initial part of the measurement is observed to have a decaying exponential form similar to a discharging RC circuit (Figure 3-1). This is the first major difference from the Bewig model as the capacitance across the air gap will depend on several factors involving the interaction of alpha particles with non-ionized gas molecules. From our examination of several alpha particle experiments,[113,121] we use an attenuation model to determine the effective differential charge from the intersection of attenuated alpha particle beam E_α with the aqueous surface (Figure A-1).

A schematic circuit diagram of the ionizing cell is shown in Figure 3-2. In this model, C_a is the junction of Am-241 electrode/N$_2$ attributed to the charge from ionized and non-ionized gas particles across a distance gap Z_1 between the Am-241 electrode and solution surface. The alpha particle beam from the surface of the Am-241 electrode is notably attenuated near the solution surface by factor α (Appendix A). Hence, C_a is described as,

$$C_a = \alpha \left[\frac{\varepsilon_0 \, \varepsilon_{air} \, \pi r^2}{Z_1} \right] \tag{3.1}$$

where ε_0 is permittivity of vacuum, r is the radius of Am-241 electrode and ε_{air} is nearly 1. Typically, electrified interfaces in circuit models are described by a resistor and a capacitor arranged in parallel.[2] However, for our model, the resistance of the nitrogen gas environment is deemed to be too high and will impede current flow. We then simplify this to C_a alone and do without the inclusion of the parallel resistor. A list of the experimental parameters and their values are summarized in Table 3-1 below.

Given the ionization of N_2 molecules, there is a steady-state concentration of ions present[94,113,121] that is functionally considered as the current i_1 in this circuit. With respect to i_1, the air/aqueous interface can be described by a capacitor C_s and resistor R_s in parallel,

$$C_s = \frac{\varepsilon_0 \varepsilon_{H_2O} A_{sol.}}{\kappa^{-1}} \tag{3-2}$$

$$R_s = \frac{1}{\alpha}\left[\frac{\kappa^{-1}}{\sigma_s}\right] \tag{3-3}$$

where $A_{sol.}$ is the area of the solution surface parallel to Am-241 electrode, κ^{-1} is the Debye length, and σ_s is the equivalent conductivity of the electrolyte solution. Both C_s and R_s have key roles in charge transport and depend on the nature of the salt solution. These values are summarized in Table 3-2.

The parameters associated with the solution/Pt interface are similar to the air/aqueous interface. The electrolyte/electrode interface is then described by a capacitor C_b and a resistor R_b in parallel,

$$C_b = \frac{\varepsilon_0 \varepsilon_{H_2O} A_{Pt\,gauze}}{\mathbb{Z}_2} \tag{3.4}$$

$$R_b = \frac{\mathbb{Z}_2}{\sigma_{Pt}} \tag{3.5}$$

where A_{Pt} is the area of the Pt electrode placed parallel to the Am-241 electrode, $\mathbb{Z}_2$ is the distance between the solution surface and the Pt gauze surface, and σ_{Pt} is the exchange current density of ions at the Pt gauze surface. Unlike most metal electrodes, a platinum electrode is an

42

efficient transporter of charge across its electrolyte/electrode boundary. Thus, the surface of platinum retains less overall charge when compared to other metals such as gold.

When compared to the air–aqueous interface, molecules are more restricted in their movement at the electrolyte/Pt gauze largely due to its more organized double layer. Therefore, we consider the electrolyte/Pt gauze as being functionally more capacitive, rather than resistive. For the purpose of this study, we will not include the R_b term in our circuit analysis. Discussion of the assumption associate with R_b of different metal electrodes of varying exchange current densities will be addressed in future work.

For our model, the final element in the circuit is the resistor R_{Pt}. R_{Pt} is assumed to have a constant internal resistance due to the isothermal bulk solution. As the Pt gauze is fully submerged in the solution and also has a greater surface area than the Am-241 electrode, the total internal resistance is described as,

$$R_{Pt} = \rho_{Pt} \left(\frac{d_{gauze}}{A_{gauze}} + \frac{d_{wire}}{A_{wire}} \right) \qquad (3.6)$$

Table 3-1. List of experimental parameters and values used in the model. Rows 2-12 are real values that were part of the experimental setup. Row 1 is calculated from a set of assumptions and experimental parameters as summarized in Appendix A.

Row	Parameter	Description	Values
1	α	attenuation factor for Am-241 electrode	4.0E-06
2	z_1	distance between the Am-241 electrode and solution surface, m	7.2E-03
3	z_2	distance between the solution surface and Pt gauze surface, m	7.8E-03
4	d_{gauze}/d_{wire}	length of the Pt gauze/wire, m	6.0E-03
5	r	radius of Am-241, m	3.6E-03
6	ρ_{Pt}	resistivity of Pt, ohm m	1.1E-07
7	ε_{air}	relative permittivity of air at 295 K	~1
8	ε_{H_2O}	relative permittivity of water at 295 K	79.4
9	$A_{Pt\ gauze}$	surface area of Pt gauze, m^2	8.8E-04
10	$A_{Pt\ wire}$	surface area of Pt wire, m^2	2.0E-07
11	$A_{sol.}$	surface area of solution, m^2	4.4E-03
12	T	temperature, K	295.15

Table 3-2. Calculated values of extracted model parameters for 1.0 M NaCl and Na$_2$SO$_4$ solutions are summarized below. These conditions assume ambient lab temperature and pressure. The formula for calculating the ionic strength I and Debye length κ^{-1} can be found in the List of Abbreviations and Symbols.

Sym.	Description	1.0 M NaCl	1.0 M Na$_2$SO$_4$	Eq.
I	Ionic strength of 1.0M of electrolyte solution, mol/L	1.0	3.0	
κ^{-1}	Debye length for 1.0M electrolyte solution, m	3.1E-10	1.8E-10	
σ	Equivalent conductivity of 1.0M electrolyte solution, Ohm^{-1} cm^{-1}	83.3E-03 [ref. 124]	5.98E-02 [ref. 125]	
C_a	Capacitance at Am-241 electrode/N$_2$ interface, F	1.65E-13	1.60E-13	(3.1)
C_s	Capacitance at air/aqueous interface, F	1.03E-02	1.73E-02	(3.2)
R_s	Resistance at air/aqueous interface, Ohm	66.8	39.4	(3.3)
C_b	Capacitance at solution/Pt interface, F	7.97E-11		(3.4)
R_{Pt}	Internal resistance (Pt gauze electrode), Ohm	0.20		(3.6)

3.3.2 Governing Equations

A system of equations will express the relationship of the terms used to describe the circuit model. The first step to solving this physical system is applying a current balance at a point between C_a and C_s/R_s (Figure 3-2):

$$i_1(t) - i_2(t) - i_3(t) = 0 \tag{3.7}$$

where i_1 is the current of the entire system, i_2 and i_3 is the current at the air–aqueous interface, and t represents the time (in seconds). Using Kirchhoff's voltage law, a separate equation is used to describe the air–aqueous interface,

$$\frac{1}{C_s}\int i_3(t)dt - i_2(t)R_s = 0 \tag{3.8}$$

With exception of R_b and i_5 (excluded for this study), Kirchhoff's law is further applied to the entire loop involving the remaining circuit elements by applying a charge and voltage balance, such that i_4, i_6, and i_7 is exactly equal to i_1 and the overall system is simplified to:

$$\frac{1}{C_a}\int i_1(t)dt + \frac{1}{C_s}\int i_3(t)dt + \frac{1}{C_b}\int i_1(t)dt + i_1(t)R_{Pt} = \Omega e^{-\lambda t} \tag{3.9}$$

where Ω and λ represent the amplitude of the voltage and decaying rate respectively. Following the Laplace transformation of (9), $i_1(t)$ is an unknown variable obtained from a non-linear regression of the real-time potential data (Figure 3-1). The derivations and results of the non-linear regression analysis are summarized in Appendix B.

46

3.3.3 Relating Measured Surface Potential to Surface Tension

In order to determine the interfacial potential across the air–aqueous interface, and to further assess the quality of our circuit model, we relate the electrochemical measurement with the thermodynamic potential. Relating the concept of measured potential to the chemical composition of the system, the Nernst Equation can be introduced to relate the measured cell potential V_m to the $\Delta G_{surface}$ or Gibbs free energy at the solution surface (mJ):

$$\Delta G_{surface} = -zeN_A V_m \tag{3.10}$$

where z, e, N_A are the number of moles of electrons in the circuit, the fundamental charge, and Avogadro's number respectively. If current $i_1(t)$ is known, the number of charges z circulating through the equivalent circuit can be calculated, such that,

$$z = \Delta t \frac{i_1(t)}{e N_A} \tag{3.11}$$

where Δt is the difference of the final and initial experimental time. As V_M is a combination of several circuit elements, an additional term v_i, i.e., the interfacial potential at the air–aqueous interface, is introduced to express V_m and other circuit elements as the following:

$$v_i = V_M - \frac{1}{C_a} \int i_1(t)dt - \frac{1}{C_b} \int i_1(t)dt - i_1(t)R_{Pt} \tag{3.12}$$

Hence, (3.11) and (3.12) can be inserted into (3.10), such that the newly formed Nernst equation will now be:

$$\Delta G_{surface} = -\Delta t \left[i_1(t) \, v_i \right] \tag{3.13}$$

With the aim of determining the surface tension of the air–water interface, the surface tension of the solution $\gamma_{sol.}$ is directly related to the ratio of $\Delta G_{surface}$ (mJ) to the surface area of the solution $A_{sol.}$ (m^2):

$$\gamma_{sol.} = \frac{\Delta G_{surface}}{A_{sol.}} = \frac{-\Delta t \left[i_1(t) \, v_i \right]}{A_{sol.}} = \frac{mJ}{m^2} \tag{3.14}$$

From calculations of extracted parameters and relevant circuit terms, v_i, $i_1(t)$, and $\gamma_{sol.}$ from (3.12) and (3.14) is calculated for $70 \leq \Delta t \leq 80$s (Figure 3-3) and values are summarized in Table 3-3

Literature surface tension* values for 1.0 M NaCl and Na$_2$SO$_4$ were extrapolated based on relative change in solutions reported from several sources by Pegram and Record[28] and experimentally measured surface tension of water[126] at T = 22°C. From equations (3.13) and (3.14), we predict the surface tension γ of the sodium salt electrolytes with relatively good accuracy. Compared to the literature value of 74.2 ± 0.17 mN/m for 1.0 M NaCl, our calculated γ_{NaCl} is 74.9 mN/m (or mJ/m^2). Likewise, our predicted $\gamma_{Na_2SO_4}$ of 77.2 mN/m is nearly equal to 75.3 ± 0.09 mN/m from literature. The closeness of our predicted surface tension values relative to literature strongly indicates the validity of our surface potential measurements and our circuit analysis model.

Table 3-3. Interfacial potential, current, and surface energies for 1.0 M NaCl and Na2SO4 solutions. Values calculated from equations (3.12) to (3.14).

	Experiment	Model			Literature *
	Measured potential, 22°C	Interfacial potential (eqn. 3.12)	Current in the circuit (eqn. 3.13)	Surface tension (eqn. 3.14)	**Surface tension, 22°C**
	V_m	v_i	$i_1(t)$	$\gamma_{sol.}$	
	volts	volts	amperes	mJ/m^2	mN/m
Pure H$_2$O	-0.49 ± 0.01	-	–	–	72.3 ± 0.17
1.0 M NaCl	-0.38 ± 0.03	-0.62	-0.54	74.9	74.2 ± 0.17
1.0 M Na$_2$SO$_4$	-0.45 ± 0.01	-0.74	-0.47	77.2	75.3 ± 0.09
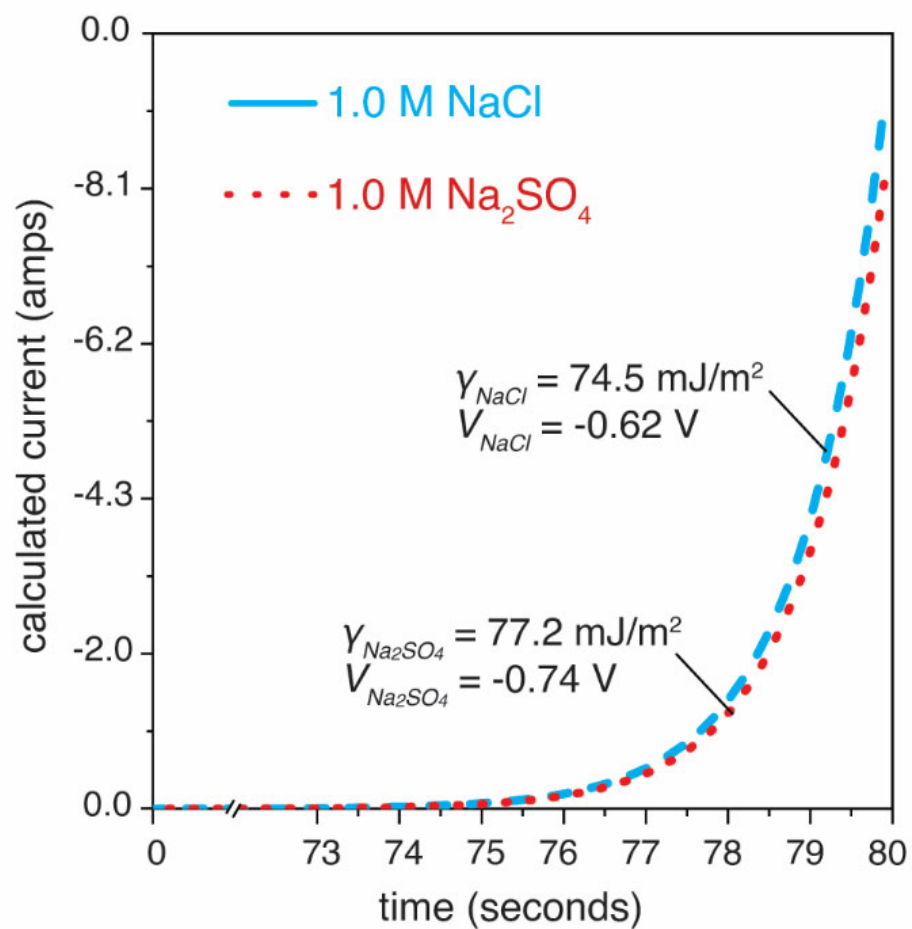
Figure 3-3. Calculations of current (A) vs. time ($70 \leq \Delta t \leq 80$ seconds) for 1.0 M NaCl (--) and 1.0 M Na_2SO_4 (…). The average interfacial potential, current, and surface energies are reported in Table 3-3.

3.4 Results & Discussion

3.4.1 Neat Water

For these experiments, the initial potential value of -0.059V is regarded as a benchmark calibration of the clean surface. The ionizing method surface potential is highly sensitive to contamination and can be ideally utilized for monitoring surface cleanliness over time. Accordingly, we observed more positive values for the initial potential with even the slightest contaminant level. This is a significant point as surface-clean pure water -0.49 ± 0.01 V is observed to have the most negative potential drop over time compared to surface-clean salt solutions. However, the slightest presence of contamination, below levels identified through surface tension means, have large observable effects on its macroscopic surface properties, which has often been debated.[98,127,128] Surfactant impurities are susceptible to creating a long-range large negative electrostatic potential into the bulk solution of either pure water or electrolyte solutions, despite large Debye lengths.[128] Similarly, salt electrolyte impurities are observed to induce orientational order collectively from the water molecules near their respective interface.[127] Therefore, we utilized several surface cleaning techniques repeatedly before measurement including the use of furnace drying and combustion of high purity salts, and repeated surface aspiration of the solutions prior to measurement. Despite the high concentration of electrolytes used, the measured potential of electrolyte solutions in this work is shown to be substantially more positive than that of pure water, indicating the contribution of electrostatic charge from solvated ions at the air–aqueous interface.

3.4.2 Aqueous Electrolytes: NaCl vs. Na$_2$SO$_4$

Surface potential studies by Frumkin[101], Randles[84,87,102], and most recently by Farrell and McTigue[104] describe changes in $\Delta\chi$ (where $\Delta\chi = \chi_{electrolyte} - \chi_{water}$) for simple electrolytes (e.g., NaClO$_4$, KI, KBr) as positive and increasing in magnitude with increasing electrolyte

concentration. However, these $\Delta\chi$ values are conventionally corrected from extrapolated data of measured potentials. This practice is described by Jarvis and Scheiman[91] where the potentials of electrolytes are plotted against their concentrations and fitted to a trendline that is then extrapolated to zero concentration. The extrapolated value at zero concentration is often presumed to be the χ_{water}. As a result, the $\Delta\chi$ reported by Frumkin and others are normalized to an extrapolated point obtained from a trendline of measured potentials plotted against their concentrations. However, it is difficult to assess the accuracy of χ_{water} in this way. Even supposing the extrapolated χ_{water} is close to the true surface potential of water, the precise fitting of trendlines derived from dilute concentrations can vary significantly from trendlines that include slightly higher concentrations.[104] For the purpose of discussion, our reported $\Delta\chi$ is not a result of extrapolation, but instead, a direct subtraction of surface potentials (at t = 60 s) of the aqueous salts from the ultrapure water measurement.

In recent years, several authors have reported theoretical estimates of $\Delta\chi$ for various aqueous salts. Calculations by Ishiyama and Morita[129] and dos Santos et al.[118] for 1.0 M NaCl are +0.001 V and +0.002 V respectively. Dos Santos et al. also estimate +0.010 V for 1.0 M Na_2SO_4. Despite the obvious differences between experimental and theoretical estimates, these calculations are in reasonable agreement with experimental $\Delta\chi$ reported by Frumkin[101,102] and Jarvis and Scheiman[91]. These studies, albeit with slightly different ionizing methods, report -0.001 V at 1.0 M NaCl. Conversely, Frumkin reports +0.003 V at 1.0 M Na_2SO_4 compared to the +0.035 V by Jarvis and Scheiman. Both studies utilize the trendline extrapolation processing of their data and thus it is then expected that their $\Delta\chi$ values would be similar. Utilizing our direct subtraction method, $\Delta\chi$ for 1.0 M NaCl and 1.0 M Na_2SO_4 is observed to be +0.120 V and +0.040 V respectively. Comparing the $\Delta\chi$ for 1.0 M NaCl, there is a major difference, as expected, in our

value compared to the -0.001 V reported by Frumkin. Yet, our $\Delta\chi$ for 1.0 M Na_2SO_4 is unexpectedly closer to Jarvis and Scheiman.

While the distribution of ions, electrons, and the preferential dipolar arrangement of surface water molecules for pure water is shown to be the most negative measured potential, it is consequential that the addition of simple ions leads to a redistribution of charges within the air–water electrical double layer. It has also been suggested that the surface potential depends strongly on the nature of the anions and weakly on the nature of the cation, especially for alkali metal ions.[35,84] From our results, the influence of the anion within the air–water electrical double layer is evident. Consistent with experimental[39–41,51,55,130–133] and theoretical[35,65,134–136] studies using other methods, the larger $\Delta\chi$ for 1.0 M NaCl (+0.120 V) compared to 1.0 M Na_2SO_4 (+0.040 V) demonstrates the greater influence of chloride on the electrical double layer.

Several physical phenomena are likely explanations for the observed surface potential differences between Na_2SO_4 and NaCl. With the formation of the electrical double layer, monovalent anions like chloride strongly approach the surface layer more consistently than cations.[33,41,55,130] Indeed, polarizable anions of certain charge-to-size ratios are considered to have greater propensity for the surface.[41] Unlike chloride, sulfate has a much broader, strongly bound hydration shell (widening the interfacial region[40]) and persists in the subsurface layer towards the bulk phase solution.[133] Apart from anions, water molecules are considered to have dipole and quadrupole contributions to the surface potential[3], which suggests that the dipolar potential drop may have its origin derived from the preferential orientation of these interfacial water molecules. Finally, the presence of solute can change the orientation of interfacial water molecules, such that $\Delta\chi$ is considered evidence of the anion distribution within the interface. Increasing potential corresponds to increasing adsorption of anions at the air–water interface; from our results, it is

evident that chloride anions preferentially favor the air–water interface compared to sulfate anions.

3.4.1. Validation of Circuit Model

The primary objective of the present work is to relate measured potential from real-time ionizing surface potential data (Figure 3-1) with the radioactive decay from the radioactive electrode (Figure B-1). Using the experimental parameters in Table 3-1, non-linear regression analysis of surface potential data was used to obtain the average current $i_1(t)$ (Figure 3-3), and subsequently, both the interfacial potential at the air–water interface v_i, and surface tension $\gamma_{sol.}$ for 1.0 M NaCl and Na$_2$SO$_4$ solutions using (3.12) and (3.14).

In this study, the interfacial potential v_i is distinctive from the surface electric potential χ as it is calculated from the circuit model that describes the air–water interface equations (3.2) and (3.3). A more detailed molecular dynamic study is required to determine the surface potential, which would entail the effects of the molecular interactions and structure of the electric double layer. By considering the v_i, we can draw a close comparison of surface potential data with the instrumentation used to measure it. Relating v_i to the surface tension $\gamma_{sol.}$ offers a different approach to validating data and ionizing surface potential methods.

From the results of the model (Table 3-3), the calculated v_i is shown to have a greater magnitude compared to V_m for both sodium salt electrolytes. For example, compared to the measured potential of -0.38 ± 0.03 V for 1.0 M NaCl, the calculated v_{NaCl} is nearly 1.6 times as negative at around -0.62 V. From a molecular perspective, there are two possible contributions to the value of v_i: the presence of the electrical double layer at this electrified boundary, and the net change in the preferred orientation of interfacial water molecules caused by the presence of ions.[81] Moreover, there is no definitive method of determining the relative input of the two contributions.

It is reasonable to assume the greatest contribution to v_i is from the electrical double layer due to the long-range electrostatic interaction of ion charge with the surface.[81,102,128] Consequentially, the more negative interfacial potential v_i indicates an underestimation of the surface potential value at the air–water interface when compared to its measured potential V_m. Therefore, the smaller magnitude of V_m indicates the screening of electrostatic charge at the top-most interfacial water molecules by a diffuse layer of subsurface water molecules.[128,137] In the presence of ions, screening of the top-most layer by subsurface layers is altered slightly as ions themselves can preferentially adsorb to the surface. Furthermore, this process will depend upon the concentration of ions in the bulk solution. Surface adsorbed ions can be screened by larger numbers of neighboring interfacial water molecules.

3.5 Conclusions

In this work, we presented measured surface potentials of ultrapure water, aqueous sodium chloride, and aqueous sodium sulfate electrolytes. Our measured surface potential difference of the air/water interface is -0.49 V ± 0.01 V. The negative value indicates that the net electric field at the ultrapure water surface is positive, a result consistent with the net dipole moment of interfacial water molecules oriented such that their hydrogens are pointing toward the air phase. Although, the quadrupolar moment from interfacial waters may have a significant contribution to the observed surface potential. With the addition of electrolytes, such as NaCl and Na_2SO_4, a positive increase of the surface potential at the air/water interface is observed. However, interpreting surface potential measurements must also involve an understanding of the impact of radioactive electrodes in measuring the potential drop across the electrochemical cell. Thus, we also propose a circuit model accounting for the different physical elements of this electrochemical cell, particularly the capacitance at Am-241 electrode/N_2 gas interface, the capacitance and resistance at the air–water interface, and the internal resistance from the Pt gauze electrode. We successfully validate our model by comparison of our derived surface tension values for aqueous NaCl and Na_2SO_4 electrolytes to that of the literature.

Chapter 4. Halide Ion Adsorption at Air–Aqueous Interface

4.1 Introduction

Given the prevalence of solvated ions in aqueous environments, quantifying their adsorption behavior is significant to determining their reaction mechanisms at heterogeneous interfaces. In a prominent example, the heterogeneous uptake of ozone (O_3) on surfaces of halide-rich sea salt aerosols releases molecular halogens into the atmosphere[138–141]; while the deposition of sea salt aerosols and other reactive bromine species (*e.g.* $BrONO_2$) on snowpack surface also produces mixed halogens via radicals and/or O_3.[57,142–145] Both bromide and iodide can discretely interact with O_3 to form hypobromous acid (HOBr)[45,146,147] and hypoiodous acid (HOI)[148–150] respectively. HOI has only been recently confirmed to generate interhalogens (e.g., ICl, IBr) after uptake by chloride and bromide-rich aerosols.[151] Despite these discoveries, the mechanisms involved in the direct availability of halides for interfacial reactions are still unresolved. Although some molecular dynamics (MD) simulations[12,33,66] predict the enhancement of both bromide and iodide at the aqueous surface, other studies[152,153] have indicated a depreciative enhancement for both overall. Moreover, there are many examples where mixtures of these ions are not simply the sum of the individual surface properties.[12,37] Presently, results from surface-sensitive spectroscopies such as sum frequency generation (SFG)[39,42,64] and second harmonic generation (SHG)[43,44,132] have a reasonable agreement with MD simulations showing surface enhancement of

both bromide and iodide. Conversely, photoelectron spectroscopy (PES) has revealed different outcomes on the enrichment of aqueous iodide at the surface. While an initial PES study[154] revealed the iodide surface concentration was observed to be nearly 2.5 times the bulk, more recent studies postulate a lesser enrichment at the aqueous surface.[155–157] Interestingly, recent X-ray Reflectivity (XRR) data for $SrCl_2$ and RbBr solutions suggests that both the chloride and bromide are depleted from the surface, respectively.[158]

Per these findings, some inconsistencies of surface activity findings, and an ongoing pursuit of the underlying forces for specific ion effects, there is continuing interest in understanding the surface enrichment, or depletion, of inorganic ions at aqueous surfaces. Additionally, varying and complementary methods that provide additional aqueous surface data such as those described above, and including surface potential measurements, are necessary to refine the understanding of aqueous interfacial phenomena.

4.2 Methods and Materials

4.2.1 Materials and Sample Preparation

Sodium chloride (99+% for analysis, ACROS Organics) and sodium bromide (≥99%, ACROS Organics Extra Pure) were heated in air to 600 °C in a furnace (>7 hours) to remove trace organic residue from salts crystals.[52] All stock solutions (5 mol/kg water) were prepared using ultrapure deionized water (>18 MΩ.cm, Milli-Q) in glassware previously cleaned with piranha solution (3:1 sulfuric acid with hydrogen peroxide). Sodium iodide dihydrate (99+%, for analysis, ACROS Organics) crystals were directly dissolved and thrice filtered through 0.2 μm PVFD Syringe Filters (Non-Sterile, Fisherbrand™ Basix™).

The cleanliness of the salt solutions was verified by Wilhelmy plate surface tension using Sigma 700 Force Tensiometer (Biolin Scientific) (Figure 4-1). All glassware containing solutions was covered with aluminum foil to minimize exposure to light and dust. Successive

molal dilutions from stock were surface purified by repeated aspiration of stirred solution with a

PTFE tip before dilution.[98] In order to minimize electrical interference from dissolved CO_2 and

O_2 during measurement, dilutions were degassed for 25 to 35 minutes using argon (99.998%

prepurified, Praxair) up to 2 minutes before ionizing surface potential measurement. Fresh stocks

of concentrated cetyltrimethylammonium bromide (CTAB), (Sigma-Aldrich, ≥98%) and sodium

dodecyl sulfate (SDC), (Sigma-Aldrich, ACS reagent, ≥99%) were initially prepared by

dissolution in ultrapure water, and then diluted to the 0.3 mM concentration with degassed water.

The 0.3 mM surfactants were used as controls for the ionizing surface potential. Experiments

were performed at 295.15 K ±0.1 and 26.2 ±2.8 percent relative humidity of the room.
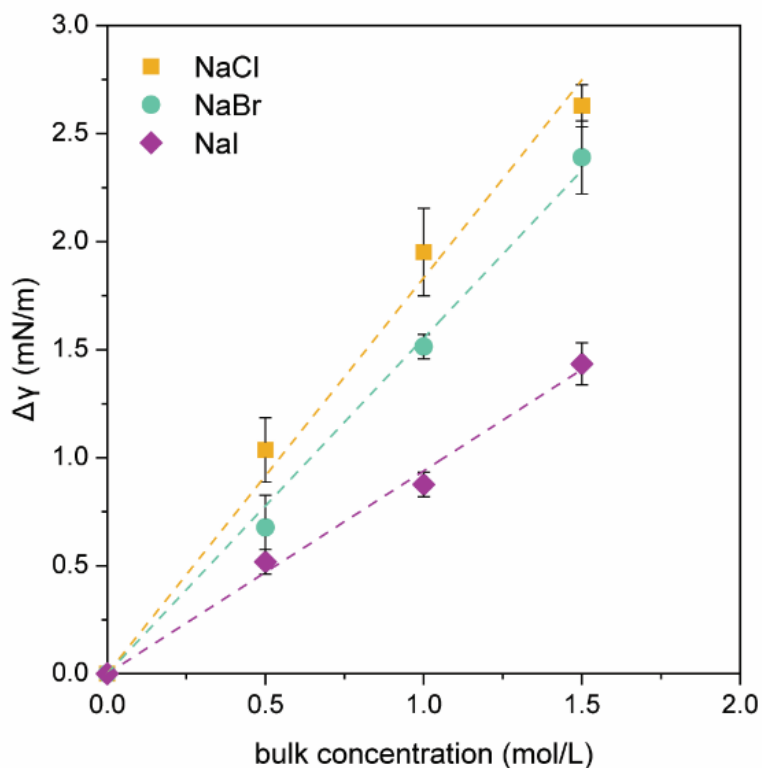
Figure 4-1. The surface tension of aqueous NaCl, NaBr, and NaI relative to neat
water (where $\Delta\gamma = 0$ mN/m). with Pegram and Record (2006) [ref. 28]
demonstrating the relative contaminant-free surface.

4.2.2 Vibrating Plate Surface Potential

Surface potential measurements of 0.3 mM CTAB and SDS aqueous solutions were performed in triplicate on a Teflon Langmuir (KSV NIMA, Biolin Scientific) with a measured area of 549.08 square centimeters. Before measurement, the trough was meticulously cleaned with ultrapure water and reagent alcohol. The Surface Potential Sensor (SPOT) (SPOT I, Biolin Scientific) probe was placed halfway along the length of the trough and about 1-2 mm above the solution surface; leaving enough distance from the edges to reduce interference. The counter electrode was submerged in the aqueous solution parallel to the vibrating probe surface. The SPOT probe was turned on at least 10 min before starting the first experiment. For each surface potential measurement, the trough was filled with neat water. The measured pH of the neat water is 5.6 due to the dissolution of CO_2. For a single measurement lasting ~ 1 hr, the surface potential of neat water is zeroed and taken as the reference value (V_0). The neat water was replaced by a fresh solution of 0.3 mM CTAB (or 0.3mM SDS) and real-time voltage data is obtained. For the voltage data recorded between 15-60 minutes for each sample, the measured voltage was plotted and fitted to a line, where the intercept was taken as the maximum surface potential (V_P). Thus, the reported ΔV (a measured parameter assumed to be equivalent to the abstract parameter of $\Delta \chi$) is equal to the $V_P - V_0$ (where $V_0 = 0$). Between each set of experiments, the trough and counter electrode was cleaned thoroughly with ultrapure water and reagent alcohol.

4.3 Surface Potential Measurement of Inorganic Electrolytes

Over the past 125 years, only a handful of electrochemical techniques have been applied to studying inorganic electrolytes at the air–aqueous interface. The first technique pioneered by Kenrick[159], later developed by Frumkin[101] and others[84,87,103,104,160], is the capillary drop (mercury liquid jet) method. Another technique, introduced by Guyot[161] and adapted by Jarvis and Scheiman[91], involves ionizing radiation to ionize the gas in between a metal reference electrode and a stationary liquid surface. In this section, we present the measured surface potential by these techniques and present some details on these electrochemical techniques.

By convention described by Randles (1963),[1] the χ_{water} is derived from plotting the χ_{salt} (measurable surface potential) of the salt solutions, MX, against their concentrations, $[MX]^{1/2}$, and extrapolating to zero concentration. The dotted lines indicate trend only. Frumkin (1924) and Jarvis & Scheiman's (1968) data were replotted for comparison.[50,56] Consistent with notable measurements of the surface potential of salt solutions, our previously measured surface potential for 1.0 M NaCl and 1.0 M Na_2SO_4 are observed to be more positive than that from neat water.[96] Surface potentials for aqueous electrolytes are often reported in terms of changes in the χ_{salt} (via directly measurable potential V) relative to an extrapolated term at infinite dilution, *i.e.*, the surface potential difference $\Delta\chi$ where $\Delta\chi = \chi_{salt} - \chi_{water}$.[91,101,102] While there have been attempts to determine χ_{water} from an infinite dilution method[104], this extrapolated term should not be considered the real χ_{water} but as a point where there is no dipole reorientation.[115] Nonetheless, keeping with the convention described by Randles[102], we also present our $\Delta\chi$ for aqueous NaCl compared to previous experiments by Frumkin[101] and Jarvis & Scheiman[91]. Thus, with the data shown in Figure 4-2, our $\Delta\chi$ values vastly differ, importantly so, in sign and magnitude next to other empirical $\Delta\chi$ values for aqueous NaCl.

Despite these magnitude differences, Figure 4-2 reveal an obvious increase in $\Delta\chi$ (or χ_{salt}) with increasing presence of chloride ions. In the case of our measurements, this increase of the trends in the positive direction results in a distinct Langmuir adsorption shape that appears to approach a limit of near saturation at higher electrolyte concentrations. Correspondingly, Randles[84] also reports positive $\Delta\chi$ curves for other inorganic salts, *e.g.*, KI, KSCN, $NaNO_3$, $NaClO_4$. Prior to experimental work involving surface-sensitive spectroscopy, the incremental changes in χ have been interpreted as indicative of a partitioning of ions in the electrical double layer where the negatively charge layer is closest to the air phase, and its positive layer toward the bulk solution; thus, this substantiates predictions made by the earliest polarizable force field models.[35,37]
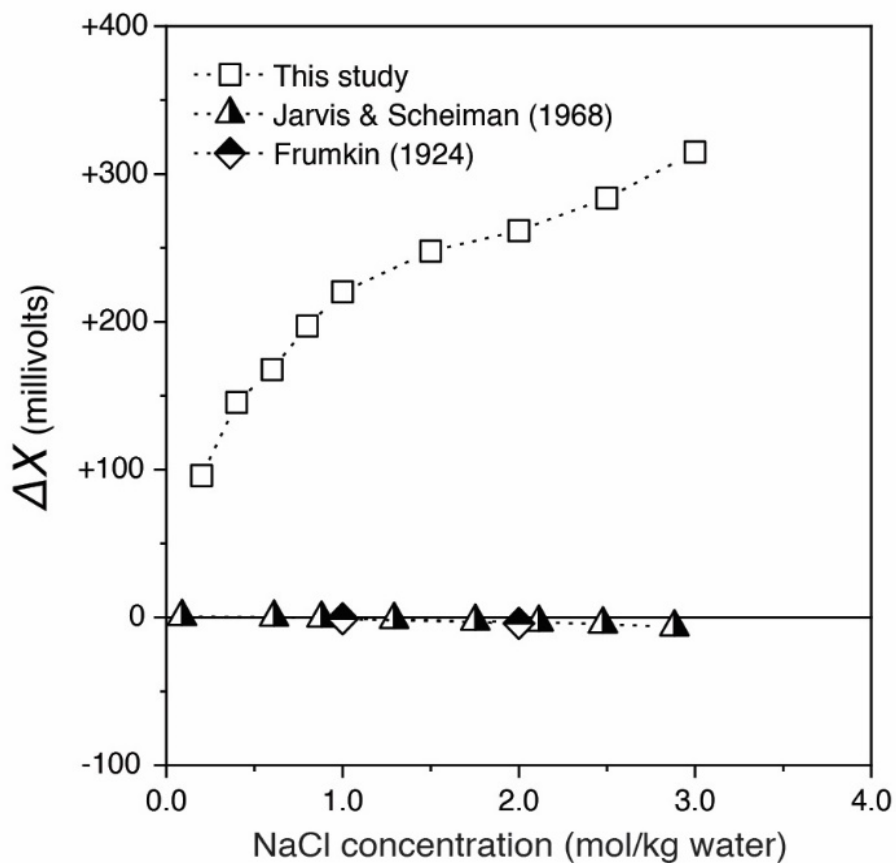
Figure 4-2. Comparison of our surface potential difference $\Delta\chi$ ($\Delta\chi = \chi_{NaCl} - \chi_{H_2O}$) with Frumkin (capillary drop) and Jarvis & Scheiman (ionizing cell) for aqueous NaCl over a range of concentrations. These were plotted using a convention described by Randles.

4.3.1 Calibrating Surface Potential Measurements

As nearly all experimental surface potential studies resort to reporting surface potential in terms of $\Delta\chi$, particularly ionic surfactants, nonaqueous and mixed solvents, etc., an accurate measurement or value of χ_{water} is necessary to validate conclusions.[115] Conversely, as mentioned previously, there is huge variation in χ_{water} values. Although ionic surfactants and aqueous inorganic ions often engender diametrical interfacial structures, comparing their χ (directly measurable potential) can provide a supplementary reference value than mere neat water. For our study, relating surface potentials of ionic surfactants to aqueous inorganic ions permits a useful normalization scale through which we fit our potentials to adsorption isotherm models (next section).

The measurable surface potential for surfactants is often a result of a complex contribution of dipoles from hydrophobic aliphatic carbon chains, the hydrophilic polar headgroup, further induce orientation of interfacial waters.[162,163] Additionally, there is the added effect from counterions which are spatially distributed in solution but also interact with layers of waters near the headgroup.[105,164,165] Predicting surface potentials of ionic and soluble surfactants can be challenging as the interfacial structure transitions from a diffuse double layer to a monolayer with increasing surfactant concentration. Provided the system is sufficiently dilute, Stern-Gouy-Chapman theory is used to model[137,165–168] interactions between the diffuse counterions and adsorbed surfactants at the surface; however, its application to the air–aqueous interface is not sufficiently established.[165]

In Figure 4-3, the χ of two oppositely charged soluble surfactants, (a.) 0.3 mM cetyltrimethylammonium bromide (CTAB) and (b.) 0.3 mM sodium dodecylsulfate (SDS), are matched with $\Delta\chi$ values measured by either ionizing electrode[105,164] or vibrating plate[166,169] methods. In this study, χ_{CTAB} and χ_{SDS} are reported to be +0.17 V ± 0.06 and -0.50 V ± 0.04,

respectively. Again, apart from differences in magnitude, the sign of the χ_{SDS} is directly

comparable to $\Delta\chi_{SDS}$ measured by Nakahara *et al.*[105] (-0.08 V), Baldelli *et al.*[169] (-0.12 V ±0.03),

and our Surface Potential Sensor SPOT (-0.18 V ±0.06) at similar concentrations. Our $\Delta\chi$ SPOT

(Allen Lab) measurement for CTAB (+0.67 V ±0.08) is also in good agreement with the

Nakahara *et al.* (+0.4 V).

Nakahara *et al.* measured a potential minimum at SDS concentrations smaller than the

critical micelle concentration of 8.2 mM. At 0.3 mM SDS, significantly smaller than the critical

micelle concentration, there is an expected 36% surface coverage of DS^-.[170] Our observed low

surface potential is consistent with an equilibrium of a partial DS^- monolayer and an adequately

diffused counterion region. As the SDS progresses to a full monolayer over slightly higher

concentrations, the surface potential is also observed to increase (positive direction). As the

precise nature of the SDS-aqueous interface is still uncertain, we conjecture that the more

adsorbed DS^- suggests a narrower double layer where Na^+ is distributed nearer to the surface.

Alternatively, or co-dependently, the higher concentration of Na^+ can also attract the anionic DS^-

into the inner bulk[105] thereby dampening the full potential effect projected by a fixed negative

charge at the surface. From prior PS-VSFG measurements, the positive sign OH bands of the

imaginary $\chi^{(2)}$ spectrum for SDS is consistent with a positive surface electric field ($\chi_{SDS} < 0$),

i.e., water molecules orient with a hydrogen up configuration at the negatively charged aqueous

surface.[171] Important to note that PS-VSFG measurements of the OH stretch region are limited to

probing the water molecules where the centrosymmetric nature of the bulk solution is broken at

the air–aqueous solution boundary.

Contrary to SDS, CTAB at the same concentration of 0.3 mM forms a near monolayer at

the aqueous surface (cmc ≈ 0.9 mM). Thus, CTAB presents an antithetical scenario where the

positively charged ($\chi_{CTAB} > 0$) is due to the larger excess of the hydrophobic CTA^+ over Br^- at

the surface.[105] Orientation of water molecules orient accordingly, opposite in direction to the SDS case.[171] Despite the dilute SDS and CTAB concentrations, the larger absolute magnitude of χ_{SDS} ($> \chi_{CTAB}$) is likely due to the long-range electrostatic interaction between the fully dissociated ions. For SDS, Na^+ and DS^- are involved within several layers of the interfacial water due to the large Debye length. A similar effect is noted with the addition of trace surfactant impurities to the neat electrolyte solution surface, where the long-range interactions between impurities and the solvated ions result in an electrostatic potential (surface potential) drop relative to the pure electrolyte surface.[128] Yet, the potential scale from χ_{CTAB} to χ_{SDS} offers a different standardizing range, apart from χ_{water}, by which we can compare aqueous ion surface potentials.
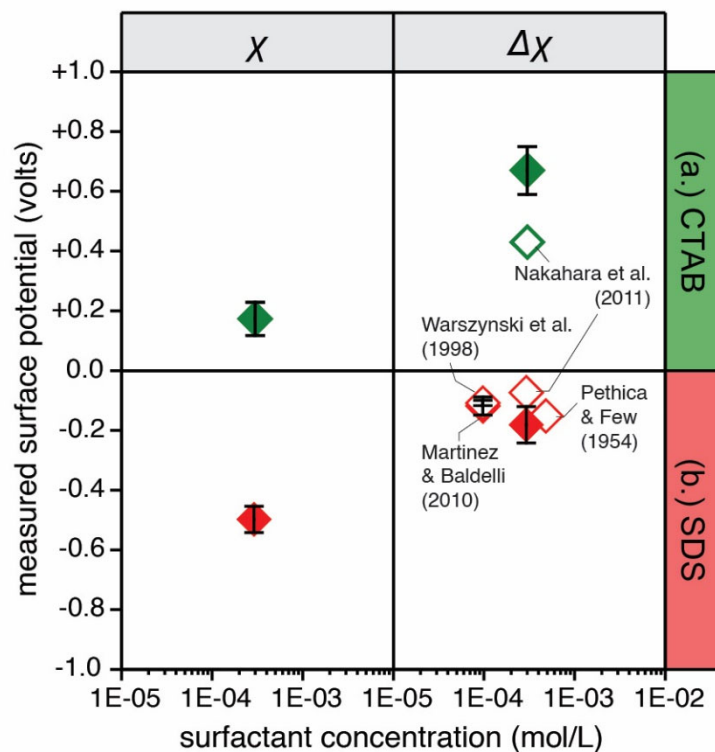
Figure 4-3. Measured χ and $\Delta\chi$ surface potentials for 0.3 mM (a.) CTAB and (b.) SDS (filled symbols). $\Delta\chi$ from refs. 24-27 and plotted as a function of bulk surfactant concentration (open symbols). Our $\Delta\chi$ measurements were made with a KSV NIMA Surface Potential Sensor SPOT (Biolin Scientific AB, Sweden).

4.3.2 Scaling Aqueous Halide Surface Potentials to Ionic Surfactants

In this study, the measured surface potentials (with the ionizing surface potential) of 0.3 mM CTAB and 0.3 mM SDS were used to scale the measured potentials of aqueous NaCl, NaBr, and NaI. This is a necessary step as the observed potentials of these halide salts range from negative to positive, and in the case of NaBr, the negative to positive occurs with increasing concentration. While the archetypal min-max normalization (rescaling) uses a $[0 : 1]$ or $[-1 : 1]$ range, the scatter of halide-potentials against their respective molar concentrations is mismatched with the aforementioned normative ranges. Therefore, we selected $[\chi_{SDS} : \chi_{CTAB}]$ as the target range to rescale our halide potential dataset for non-linear regression analysis and fitting. However, the highest measured potential in our dataset is the 3.0 M NaI (+0.22 V); a value larger than χ_{CTAB} (+0.17 V). To preserve the $[\chi_{SDS} : \chi_{CTAB}]$ range and accommodate the entire scatter range of the halide potential dataset, we shift our target range with an arbitrary number of 0.16. Thus, the normalized potentials χ'_{salt} can be calculated with the following min-max normalization equation:

$$\chi'_{salt} = \frac{\chi_{salt} - (\chi_{SDS} + 0.16)}{(\chi_{CTAB} + 0.16) - (\chi_{SDS} + 0.16)} \tag{4.1}$$
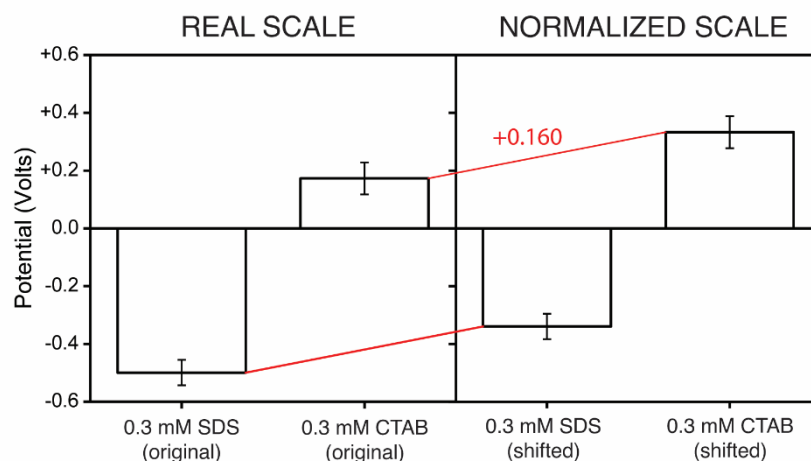
Figure 4-4. Graphical summary of the difference in scales. The "normalized scale" values were used for the fitting of aqueous halide data.

4.4 Ion Adsorption

Surface potential measurements of ions at the air–aqueous interface are significant to ascertaining the real free energies of hydration of solvated ions.[84] From recent studies, the surface potential or net electrostatic potential, generated by the asymmetry of the air–aqueous interface, is regarded as a driving force of ions towards the surface.[46,47,49] Additionally, with recent advancements in computation and experimental methodologies, accurately quantifying ion surface propensies is becoming more of a reality and thus allows for a more complete understanding of electrolyte systems and their associated interfaces.

4.2.1 Surface Potentials of Aqueous Halides Relative to Ionic Surfactants

In literature, estimates for halide adsorption propensity vary substantially among different force field models.[37,38,66,152] Potential of mean force (PMF) calculations from these models can infer the thermodynamic favorability for ion adsorption and the surface concentration of these ions compared to the bulk.[37,172] Among these force field models, the polarizable modes first

identified anion polarizability and size as important factors in surface propensity.[35,173] Hence, MD

polarizable models predict the order of halides approaching the surface as $Cl^- < Br^- < I^-$.[35] In

addition, bromide and iodide were estimated to stabilize by nearly -1 kcal/mol and -1.5 kcal/mol

at the surface.[66] Jungwirth and Tobias also calculated -0.5 kcal/mol and -0.8 kcal/mol for bromide

and iodide respectively.[33] In contrast, nonpolarizable models predicted that iodide alone (at ≈ -0.5

kcal/mol) stabilizes at the surface.[152] Despite these differences, these models confirmed that the

order of halide surface propensity coincides with the Hofmeister order[30,34,35], and that fluoride and

alkali cations are repelled from the interface.[36–38,172] Yet, we continue to note that the surface

propensities of halide ions continue to be debated.[39–45,54,154,156]

On the experimental side, SHG spectroscopy was used to quantify the ion surface

adsorption by Saykally and coworkers.[43,44,132] From fitting concentration-dependent SHG

response to Langmuir adsorption isotherm, the adsorption free energy (dG_{ads}) has been

determined for aqueous bromide and iodide. For a range of 6.0 mM to 7.0 M, the dG_{ads} for

bromide is estimated at nearly -0.3 kcal/mol.[44] Following closely, the dG_{ads} for iodide is

estimated for two concentration regions. In the 0.1 to 2.0 M, the $dG_{ads} \approx$ -6.2 kcal/mol, whereas

concentrations above 2.0 M is close to -0.8 kcal/mol.[43,132] Petersen and Saykally[132] also refitted

PES results for NaI from Faubel et $al.$[174] to the Langmuir model, where the dG_{ads} observed for

the iodide ≈ -0.9 kcal/mol (slightly above Na^+ at -0.8 kcal/mol). Accordingly, the SHG data is

consistent with polarizable models revealing the thermodynamic favorability of bromide and

iodide adsorption at the aqueous surface.

Concerning our surface potential measurements, Figure 4-3 compares the χ_{salt}

measurements of the aqueous halides to 0.3 mM SDS and 0.3 mM CTAB for reference. From our

measurements, we note a positive shift in χ_{salt} that follows the order: $Cl^- < Br^- < I^-$. Here, we

observe that surface potential of iodide is positive relative to the bromide and chloride at 1.0 M

concentration. We submit this as direct evidence that the aqueous iodide surface is, in fact, electrically net negative ($E < 0$).

There are several rationales that might explain the potential field order of halides and the "reversal" of iodide as shown by Figure 4-5. Firstly, at the 1.0 M concentration, the positive directional increase in χ_{salt} coincides with the close approach of the halides relative to the Na^+ counterion.[35,36] However, the spatial separation of charge between halide and sodium can be assumed to be similar to the other salts even at a 1.0 M concentration and does not explain the positive potential of iodide. Hence, halide size and polarizability must be invoked to explain these observations. Secondly, it is likely the iodide is moderately enriched at the surface, although the exact concentration relative to the bulk is yet to be determined.[154,155] The net positive potential (*i.e.*, net negative electric field) suggests a saturation of iodide within the interface such that it collectively contributes a larger negative charge density over interfacial water molecules and Na^+ counterions. Lastly, the induced electric field at the aqueous iodide surface arises from the asymmetric solvation of the spherical iodide.[39,129] Like thiocyanate, the high polarizability of the iodide means a dipole is likely to be induced in the anion at the surface.[41,43,173] Although water organization is predictably influenced by the relative strength of the anion-induced electric field, our results (Figure 4-5) suggest that solvating waters of the iodide dipole possibly assume a net dipole direction (from positive to negative) toward the liquid phase. This molecular picture is marginally consistent with the surface electric field of aqueous perchlorate, where the positive imaginary $\chi^{(2)}$ spectrum is observed relative to the negative $\chi^{(2)}$ of neat water.[53] Though the aqueous iodide surface is likely to be fairly analogous with aqueous perchlorate to some extent, the precise effect of these chaotropic anions on the molecular surface structure may vary owing to their specific shape/geometry at the surface.[53,175]
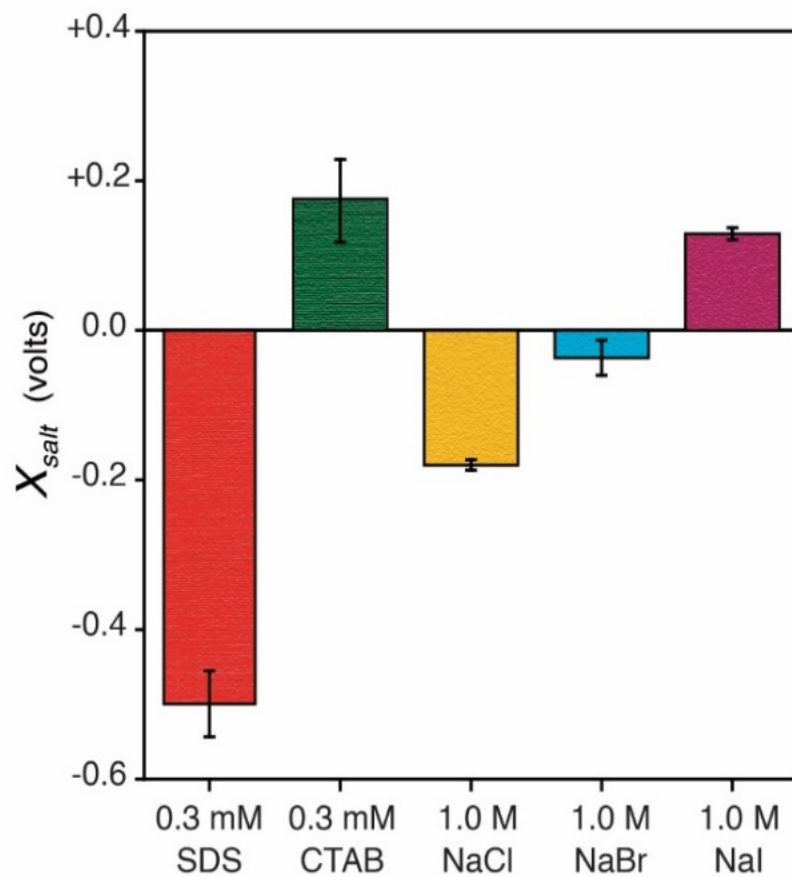
Figure 4-5. Measurable χ_{salt} of 0.3 mM SDS and 0.3 mM CTAB is compared to aqueous NaCl (-0.18 V ± 0.01), NaBr (-0.04 V ± 0.02), and NaI (+0.13 V ± 0.01) at the 1.0 M concentration.

4.4.2 Specific Halide Adsorption at the Air–Aqueous Interface

Precise measurements on the extent of anion adsorption over concentration depend on relating the surface excess of the anion to their surface tension.[36–38] Nevertheless, in this study, we adopt the generalized bulk-to-surface model Langmuir adsorption described by Saykally and coworkers [132,176–178] to extract the Gibbs free energy of adsorption from our surface potential data. In this case, χ_{salt} data were fit to a simple Langmuir adsorption isotherm:

$$\chi_{salt} = \chi_{salt}^{max} \frac{[MX]}{K + [MX]} \tag{4.1}$$

where χ_{salt}^{max} represents the highest measurable surface potential, the adsorption equilibrium, [MX] is the molar bulk concentration, and K is the adsorption equilibrium. By taking the ratio of the $\chi_{salt} / \chi_{salt}^{max} = \theta$, the Frumkin-Fowler-Guggenheim (FFG) adsorption isotherm can also be used as a fit:

$$\frac{\theta}{1 - \theta} e^{-\theta\left(\frac{zu}{RT}\right)} = K[MX] \tag{4.2}$$

where u is the lateral interaction energy between two interacting adsorbed species (at $z = 1$). If $u < 0$, the interacting adsorbed species will repel each other. In order to achieve accurate isotherm fitting of χ_{salt} data, the relative difference of χ_{SDS} - χ_{CTAB} was used to normalize χ_{salt} to an appropriate range between 0 and 1. Origin 2018 (OriginLab Corporation) and Python 3.8.5 (Spyder IDE v.4.0.1; SciPy package v.1.5.2) software were used in the nonlinear least-squares fitting of Langmuir and Frumkin-Fowler-Guggenheim adsorption isotherms, respectively (Appendix D).

Figure 4-6 shows the Langmuir and Frumkin-Fowler-Guggenheim (FFG) adsorption isotherm fits for aqueous NaCl, NaBr, and NaI. Across both models, the dG_{ads} appears to be consistent with the predicted order of increasing surface propensity: Cl⁻ < Br⁻ < I⁻. For the heavier halides, dG_{ads} for bromide and iodide are in good agreement across both Langmuir (Table 4-1) and FFG models (Table 4-2). With the Langmuir fit, the estimated $dG_{ads} \approx$ -2.5 ± 1.2

kcal/mol (FFG: -2.4 ± 1.5 kcal/mol) for the bromide is higher that the $dG_{ads} \approx$ -0.3 kcal/mol

value by Saykally *et al.*[44] Whereas, the estimated $dG_{ads} \approx$ -3.0 ± 1.1 kcal/mol (FFG: -3.2 ± 2.7

kcal/mol) for iodide is smaller than their estimated $dG_{ads} \approx$ -6.2 kcal/mol value.[43] Thus, the

surface potential results are consistent with SHG. However, the closeness in dG_{ads} values using

the Langmuir fit makes it difficult to distinctly conclude the enrichment of one halide over the

other. A similar conclusion is drawn from FFG fitting due to the overlapping errors that exist for

bromide and iodide with the FFG. Despite this, the plotted χ_{salt} versus concentration directly

shows the relative enhancement of the halides per the Hofmeister order, where iodide is most

prevalent over both chloride and bromide. Therefore, we find that iodide is more surface enriched

compared to chloride and bromide, a finding consistent with both polarizable and non-polarizable

models.[36–38]

Additionally, from the FFG fits, the derived lateral interaction or zu from our surface

potential data can provide some insight on interfacial ion interaction. From our results (Table 4-

1), the $zu < 0$ for all halides corresponding to repulsion in the model. Therefore, zu can be an

indicator of the extent of the polarizability of the anion itself. A more positive value suggests that

the highly polarizable iodide (-2.0 ± 1.2 kcal/mol) is likely to induce a dipole in the anion itself,

such that it experiences a lower lateral repulsion compared to a relatively non-polarizable

chloride (-4.8 ± 1.2 kcal/mol); coherent with both polarizable and non-polarizable models.[36–38]
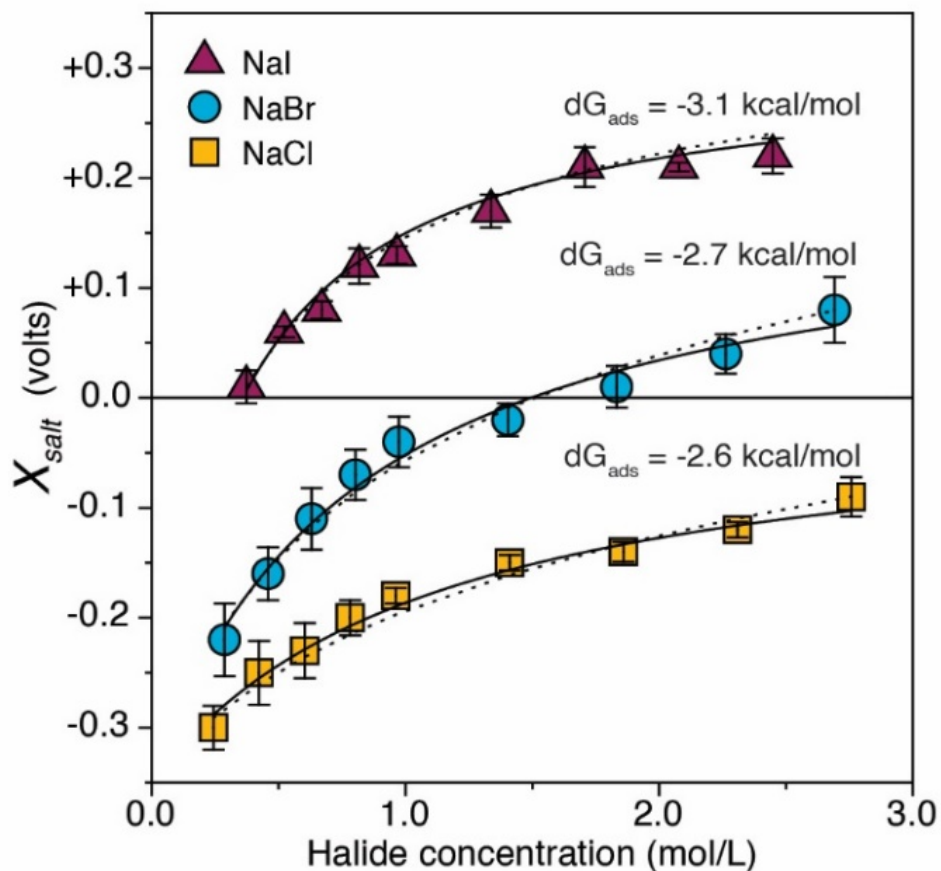
Figure 4-6. Langmuir (straight lines) and Frumkin-Fowler-Guggenheim (FFG) (dotted lines) adsorption isotherm fits of the χ_{salt} (measurable surface potential) for halide salts over their respective concentrations. Also shown, estimates for the free energies of ions adsorption calculated from the Langmuir isotherm fit. Uncertainties in the estimated dG_{ads} for the Langmuir and FFG fits are summarized in Table 4-1.

Table 4-1. Derived parameters from fitting adsorption isotherms Langmuir and Frumkin-Fowler-Guggenheim (FFG) for aqueous NaCl, NaBr, and NaI. Uncertainties are determined from statistical regression analysis.

	Langmuir		Frumkin-Fowler-Guggenheim			
NaCl	K	49.1	K	24.8		
	dG_{ads} (kcal/mol)	-2.3 ± 1.2	dG_{ads} (kcal/mol)	-1.9 ± 0.8	zu (kcal/mol)	-4.8 ± 1.2
NaBr	K	68.3	K	62.4		
	dG_{ads} (kcal/mol)	-2.5 ± 1.2	dG_{ads} (kcal/mol)	-2.4 ± 1.5	zu (kcal/mol)	-2.6 ± 0.9
NaI	K	175.8	K	240.1		
	dG_{ads} (kcal/mol)	-3.0 ± 1.1	dG_{ads} (kcal/mol)	-3.2 ± 2.7	zu (kcal/mol)	-2.0 ± 1.2

4.4 Conclusions

Our ionizing surface potential measurements of aqueous sodium halide solutions provide a fresh perspective on the influence of surface enriched halides at the air–water interface. In this study, the surface potential values are reported without the utilization of prior methods using obscurely derived χ_{water} values as a standard reference given the inherent weakness and probable inaccurate estimations arising from such. Rather, by converging on the relative potentials, including comparisons to surfactant calibrants, better insight is gained into the nature of aqueous halide salts and their inherently generated electric fields. Although the adsorption properties of aqueous halides have been explored in this study and others, there is yet more to learn about their behavior with more extended concentration ranges and in complex mixtures. While our work is limited to a small range of concentrations, halide enrichment, such as that observed for bromide in this study (>2 mol/kg water), correlates to its bulk concentration to some extent. Yet, concentration is only one parameter; temperature effects are relatively less explored.[178] Additionally, there is a need for understanding halide surface adsorption in complex mixtures, not only with other inorganic salts in purely ionic electrolytes solutions but also those with soluble organics. Indeed, much of the current research suggests larger surface enrichment factors for heavier halides (e.g., bromide) in mixed solutions.[12,37]

Chapter 5. Understanding Surface Potentials of Nonaqueous Solvents

5.1 Introduction

Solvent molecules have more short-range order in the liquid phase relative to their gaseous environment. The gas-liquid interface presents an inhomogeneous distribution of interacting molecules, owing to the asymmetric forces acting on these molecules; this unique chemical environment is fundamentally incomparable to either gas or liquid phase.[2–5] Though intrinsic to the surface, the asymmetry in forces experienced by the 1-2 layers of molecules that constitute the interface dictates the chemistry, the favored alignment and structure of interfacial molecules, dielectric properties, and the ability to transfer a solute across an interface.[5] Because of these unique properties, gas–liquid interfaces remain profoundly important to basic sciences[3,4,179], nature[33,35,37,172,180], and technological applications[74–76,79].

Unlike water, nonaqueous molecular solvents such as methanol, acetonitrile, 1,2-dichloroethane have significantly more different chemical and physical properties. Due to their higher vapor pressures relative to water (and not including the propylene carbonate), these solvents tend to evaporate readily under standard conditions resulting in a greater density of solvent molecules in the gas phase (Table 5-1) as compared to neat water. As a result, these solvents have a unique interfacial property that are contingent on solvent related quantities such as the relative permittivity ε_s (or dielectric constant) or permanent dipole moment μ.[2,5] Recently, Flood and co-workers[181] demonstrated the importance of the nature of the dielectric of the solvent on the anion binding to synthetic receptors. Solvent effects also have broad effects on the chemical sciences where organic solvents dominate, given recent advances within anion

recognition in organocatalysis.[182] Although these studies offer tremendous insight at the microscopic level, a fundamental understanding of the gas–liquid interface is not complete without addressing the relationship to quantifiable macroscopic properties. In this work, we present new ionizing surface potential measurements $\boldsymbol{V_M}$ for the neat water χ_{H_2O} (-0.40 ± 0.04 volts) and several nonaqueous solvents (e.g., methanol, acetonitrile, propylene carbonate) summarized in Table 5-2. In stark contrast to historic surface potential measurements of nonaqueous solvents, the results of our measurements show positive sign to the ionizing surface potential measurements, where the positive pole of the dipole is directed towards the liquid interior. To fully evaluate our results, we also correlate our measurements with an empirical calculation of the dipolar surface potential $\boldsymbol{V_D}$ based on the Helmholtz model. We discuss our findings in Section 5.3.

Table 5-1. Vapor pressure (kPa), conductivities (S/cm), and autoprotolysis constants (pK_{auto} = $-\log[K_{auto}/(mol^2 \ L^{-2})]$) for specific solvents at 25 °C. Solvent polarity scale derived from spectroscopic data (25 °C, 101.3 kPa) and normalized to the least polar solvent (tetramethylsilane at 0.000) to the most polar (water at 1.000).

Solvent	Vapor Pressure	Conductivity 25 °C	Auto-protolysis	Solvent Polarity
g/mol	*kPa*	*S/cm*	*pK_{auto}*	*Reichardt Scale*
Diethyl ether (74.1l)	71.7			Non-polar (0.117)
1,2- Dichloroethane (98.96)	10.6	4.0E-11		Aprotic (0.327)
Methanol (32.04)	16.9	1.5E-09	17.2	Protic (0.762)
Acetonitrile (41.05)	11.9	6.0E-10	33.3	Aprotic (0.460)
Propylene carbonate (102.1)	0.05	1E-08		Aprotic (0.472)
Water (18.02)	3.17	6E-08	14	Protic (1.000)

Table 5-2. Our measured surface potential values for methanol, acetonitrile, and water compared to other electrochemical methods. Kenrick cell potentials for nonaqueous solvents by Parsons et al.[183–185] and Trasatti[186] are negative compared to water. Derived surface potentials are taken from other experiments that are not specifically electrochemical surface potential techniques.

| Solvent | Ionizing Cell | Kenrick Cell | | | Derived | |
	This study (std. dev.)	Parsons et al.	Randles et al.	Trasatti, 1987	Parfenyuk, 2004	Krishtalik, 2008
g/mol	*volts*	*volts*			*volts*	
Methanol (32.04)	+0.45 (0.06)	-0.31		-0.18	-0.18	-0.13
Acetonitrile (41.05)	+0.21 (0.07)	-0.10		-0.10	-0.11	-0.10
Water (18.02)	-0.40 (0.04)		+0.03-0.13	+0.13		+0.14

5.2 Methods and Materials

5.2.1 Materials & Sample Preparation

Sample preparation. Diethyl ether (HPLC, 99.9%; inhibitor-free; Sigma Aldrich), 1,2-dichloroethane (HPLC, 99.8%; Sigma Aldrich), acetonitrile (Optima/UHPLC-UV; filtered 0.1 microns, Fisher Scientific), methanol (HPLC/ACS; 0.2 microns filtered; Fisher Scientific), propylene carbonate (Chromasolv/HPLC, 99.7%, Honeywell Riedel-de Haën) were used as received from freshly opened containers. Ultrapure deionized water (>18 MΩ.cm, total organic carbon: ≤ 2 ppb μg/L, Milli-Q) was taken directly from a Milli-Q® IQ 7000 Water Purification system. Solvents were transferred to freshly etched round bottom flasks and weighed on a mass balance to ensure exact volume for the ionizing cell. Pure nitrogen gas (99.999%, Praxair) was used to flush the flasks during and slightly after weighing to slow down the exchange with air. Flasks were stoppered immediately after weighing. All glassware containing solutions were previously cleaned with ultrapure deionized water and piranha solution (3:1 sulfuric acid with hydrogen peroxide). In addition, all glassware was covered with aluminum foil to minimize exposure to light and dust. Fresh stocks of concentrated cetyltrimethylammonium bromide (CTAB), (Sigma-Aldrich, ≥98%) and sodium dodecyl sulfate (SDC), (Sigma-Aldrich, ACS reagent, ≥99%) crystals were dissolved in ultrapure water, and then diluted to the 0.3 mM concentration with additional ultrapure water. All experiments were performed at 295.15 K ±0.1 and 22 ±1.0 percent relative humidity of the room.

5.2.2 Data Collection

Details on the Ionizing Surface Potential setup have been previously described. In this work, three freshly obtained platinum gauze electrodes (80 mesh; 25 x 35 mm, CH Instruments) were used as counter reference electrodes in the ionizing cell. Each gauze electrode was electrochemically cleaned by cycling in 0.10 M perchloric acid solution (99.999% trace metals

basis, Sigma Aldrich) at >50 sweeps (from -0.7 V to +1.9 V) for both electrodes at 100 mV/s. All samples were at a distance of 15 mm from the Am-241 electrode. Before sample placement, the ionizing cell was thoroughly cleaned with ethanol (histological grade; Fisher Scientific) and ultrapure water. Additionally, the space between the Am-241 and solution surface was flushed (0.7 L/min, 1 atm) with pure nitrogen gas (99.999%, Praxair).

Collection and analysis. Before measurement, solvent samples were uncorked and carefully placed in the nitrogen flushed ionizing cell. Measured voltages were then recorded for an experimental period of 3-5 minutes. The resulting voltage vs. time data was averaged between 200-300 seconds and considered one measurement. This process was repeated several times with other solvents. Water (n = 6), 0.3 mM CTAB (n = 4), and 0.3 mM SDS (n = 4) were measured daily and used as a control to ensure reproducibility and cleanness. Measurements collected for pure water samples averaged with three different Pt gauzes as counter electrodes. All other samples (n = 4) were averaged across two electrodes. Both CTAB (+0.282 V ± 0.05) and SDS (-0.428 V ± 0.05) were also averaged across multiple Pt gauze counter electrodes (alongside the solvents).

5.3 Results & Discussion

5.3.1 Surface Potential of the Air–Water Interface (χ_{H_2O})

A central dilemma to theoretical estimates of surface potentials is the accurate representation of the surface charge density associated with interfacial solvent molecules.[4,60,68] Given the fact that the surface potential is a *de facto* measurement of the surface charge density, there have been numerous attempts to interpret the sign and magnitude of surface potential to determine the precise molecular structure of the air–water interface.[3,4,68,115,117,187] Figure 5-1 presents a summary of selected literature[3,4,83,84,104,186,188–193,60,194–199,61–63,65,67–69] that show the numerical values of the surface potential of the air–water interface, i.e., the surface potential of water in contrast to the measurements from our work.

Experimentally, the air–water surface potential has been measured predominantly using the Kenrick cell (capillary drop method) by Frumkin[198,199], Randles and Schiffrin[103], and others[104,186]. In comparison, we have been the first (as far as the authors are aware) to have previously published our value for the χ_{H_2O} using the ionizing surface potential method). The Kenrick method shows a positive surface potential of water between +0 to +260 mV.[186] Methods involving the ionization of the air gap between the water and electrode surfaces have seen limited use by researchers. Despite the successful measurements of χ_{salts} by Jarvis and Scheiman[91], Foulkes et al.[94], and Adel et al.[73] there have been no reports on the χ_{H_2O} at a neat air–water interface with an ionizing cell until recently, in which we reported our first measurement of a χ_{H_2O} = ~0.50 V using an Am-241 based ionizing surface potential.[96] In our current work, we have obtained additional experimental evidence confirming the negative sign of χ_{H_2O} by averaging measurements across several Pt gauze counter electrodes. This is presented alongside measurements by others of a diverse range of simulations and experiments employed to ascertain the χ_{H_2O} (Figure 5-1).

Moreover, it is important to note that the calculated magnitude and sign for the surface electric potential is definition dependent. From Figure 5-1(b.), it is apparent that there is no overlap in either the sign or magnitude of χ_{H_2O} between the Kenrick cell and the ionizing cell measurements. However, with the Kenrick cell, surface potentials are reported as a difference in chemical potential relative to standard electrodes (calomel electrode, Ag/AgCl electrode, liquid Hg electrode).[84,102]   Thus, the Kenrick method uniquely measures differences in ion hydration enthalpies in reference to the solvent from which χ_{H_2O} is then extrapolated.[104,191] In the Kenrick method measurements, the positive sign attributed to the χ_{H_2O} originates from measurements of the negative temperature dependence of the derived surface potential.[103] In contrast, our negative surface potential value is consistent with TIP4P[60,189,200] and SPC/E[3,65,68] molecular dynamics simulations that yielded a range from -0.13 > χ_{H_2O} > -0.65 V. Other *ab initio* molecular dynamics (AIMD) and quantum mechanical (QM) yield a near-zero or positive surface potential.[4,46,201] From convention[82] described for polar dipoles, a negative χ_{H_2O} (corresponding to our χ_{H_2O} measurement) suggests a net dipole oriented with the hydrogens towards the air. However, this dipole orientation is considered not to be the dominant motif reported from spectroscopic studies of the air-aqueous interface.[22,24,202]
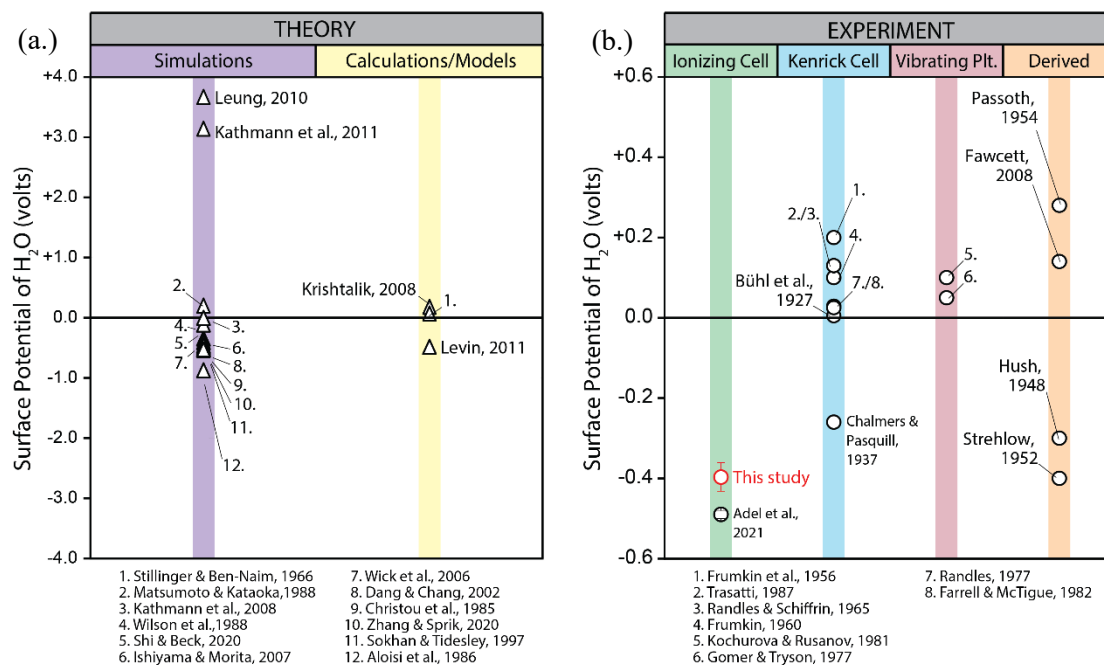
Figure 5-1. (a.) Theoretical models used to establish the χ value for the air-water interface ranges from +3.6 V < χ_{H_2O} < -1.1 V. Partial charge water models (3, 4, 7-9, 11) appear to cluster around -0.5 volts. More recent density functional theory (Leung, 2010) and *ab inito* molecular dynamics coupled to electron holography measurements (Kathmann et al., 2011) predict $\chi_{H_2O} \gg 0$ under conditions where the interfacial depth is experimentally defined. (b.) A sizeable portion of historic experimental χ_{H_2O} measurements have proposed that the χ_{H_2O} is small and positive (+0.2 V < χ_{H_2O} < +0.01 V).

5.3.2 Helmholtz Model: Quantifying the Dipolar Moment Contribution to the Surface Potential

In critical consideration of a more specific understanding of the molecular arrangement of interfacial molecules at that gas–liquid interface, we present a model (Eqn. 5.1) to help understand the orientation of the dipole moment of neat water and other pure organic liquids from our surface potential measurements. The expected surface potential response for a monolayer of molecules can be approximated using Helmholtz's double layer theory.[203] The dipolar surface potential V_D is the expected electric field E_D that arises from molecular dipoles that are aligned perfectly perpendicularly to the normal between two parallel plates (Figure 5-2). The E_D is directly proportional to the liquid surface charge density Q inversely proportional to their relative permittivity ε_s and interfacial area A:

$$V_D = -\int_{gas}^{liquid} E_D \cdot dr_z = -\int_{gas}^{liquid} \left[-\frac{Q}{\varepsilon_0 \varepsilon_s A} \right] \cdot dr_z$$

$$= \frac{Q}{\varepsilon_0 \varepsilon_s A} r_z$$

$$= \frac{\mu_z}{\varepsilon_0 \varepsilon_s A} \tag{5.1}$$

In this model, Q is the sum response from the interfacial dipolar moment μ_z (permanent molecular dipoles) that are perfectly aligned perpendicular to the parallel plates and normalized to their interfacial molecular area. The alignment of μ_z is assumed to be a zero-degree orientation relative to the surface normal when χ is positive (Figure 5-2(a.)). Per these definitions, a water molecule with μ_z with the orientation of $0°$ to the surface normal (assuming the plate is a proxy for the water surface) is where the hydrogen is pointing internally towards the bulk solution. Using this model, we calculate the V_D for 302 solvents including water (Tables D-1 and D-2) using the maximum value of the solvent μ_z. That is, the surface charge density is calculated as the

permanent molecular dipolar contribution normalized to the interfacial molecular area A assuming a zero-degree dipole orientation to the surface normal (Table D-1 and D-2). Figure 5-3 shows the V_D as a function of their relative permittivity of solvent (dielectric constant). Given this assumption, the density of the blue symbols shown in Figure 5-3 represents the maximum possible surface electrical potential for a single monolayer of interfacial solvent molecules where interfacial dipoles are oriented at precisely 0° (largest positive magnitude of surface electrical potential) or 180° (most negative surface electrical potential) with respect to the surface normal. Thus, $V_D = 0$ V represents an average 90° dipole orientation relative to the surface normal, and thus in the plane of the solvent surface.

By mapping measured potentials from 6 solvents to those in Figure 5-3, we gain a more complete perspective of the molecular structure of these solvents at their gas–liquid interface. For a closer examination on the outcomes of V_D relative to V_M, we also replotted the absolute value of the data from Figure 5-3 as a function of solvent polarity (Figure 5-4). Thus, for the least polar solvents diethyl ether (+0.10 V ± 0.07) and 1-2-dichloroethane (+0.03 V ± 0.08) assume an average 90° dipole orientation (aligned parallel to the surface) as their measured surface potentials are closest to 0 V. Potential for the aprotic solvents acetonitrile (+0.21 V ± 0.07) and propylene carbonate (+0.14 V ± 0.07) is placed perfectly within the range of the expected value at the boundary of the 0° orientation indicating the highly dipolar nature of their gas–liquid interface. The protic methanol (+0.45 V ± 0.06) and water (-0.40 V ± 0.04) are far outside the predicted potential range where the gas–liquid interface has neither a significantly dipolar interfacial surface structure nor aligns in a manner that is parallel to the liquid surface. Without a dominating or non-dominating dipolar alignment, the interfacial surface structure for these protic solvents is more complex than previously thought. Furthermore, it is also likely that properties

such as the dielectric or magnitude of the permanent dipole moment are factors that greatly influence the interfacial properties of the protic solvents.

Concerning the divergence of the pure methanol and water from the Helmholtz model, the physiochemical properties that factor into this could relate to the solvent polarity (dielectric, or indeed, the solvent capacity for self-ionization (autoprotolysis). From the solvents selected in this study, the autoprotolysis for water (pK_{auto} = 14), methanol (pK_{auto} = 17.2), and acetonitrile (pK_{auto} = 33.3) have been previously quantified.[204] The smaller pK_{auto} = 14 indicates the greater extent to which ions (acid or bases) can exist within the solvent.[204] It is thus an important criterion for the selection of solvents for titrations in non-aqueous solvents.[204] Essentially, water is the archetypical solvent for the solvation of ions relative to other nonaqueous solvents.

In the ambient environment, atmospheric CO_2 (an acidic gas) can favorably dissolve in water leading to an equilibrium concentration of carbonic acid, and the obvious decrease in pH (often between 5.6-6.3). With recent discussions on the prevalence of surface-active ions,[205–208] such as protons, we suggest that our value of the surface potential for water indicates a hydronium-dominating environment at the neat air–water interface. In contrast, the methanol surface, with its positive value indicates a negatively charged interfacial environment, wherein from the autoprotolysis products of methanol, the CH_3O^- is present at slightly higher concentrations compared to the $CH_3OH_2^+$.
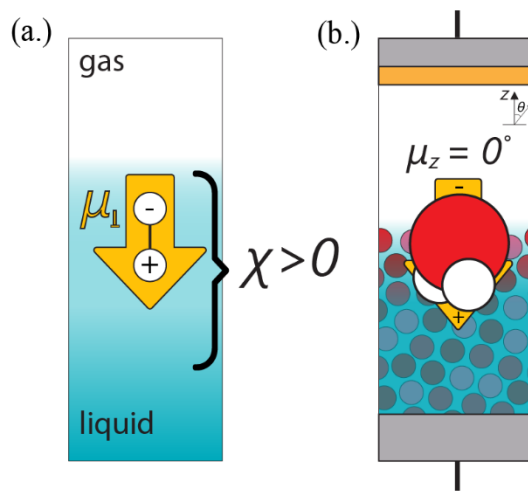
Figure 5-2. (a.) The direction of the dipole moment μ at the gas-liquid interface goes from the gas to the liquid phase when $\chi > 0$. (b.) Based on the assumptions outlined for Eqn. 5.1, the sign of V_D is positive as the interfacial dipole moment μ_z is completely perpendicular to the surface normal ($\mu_z = 0^\circ$).
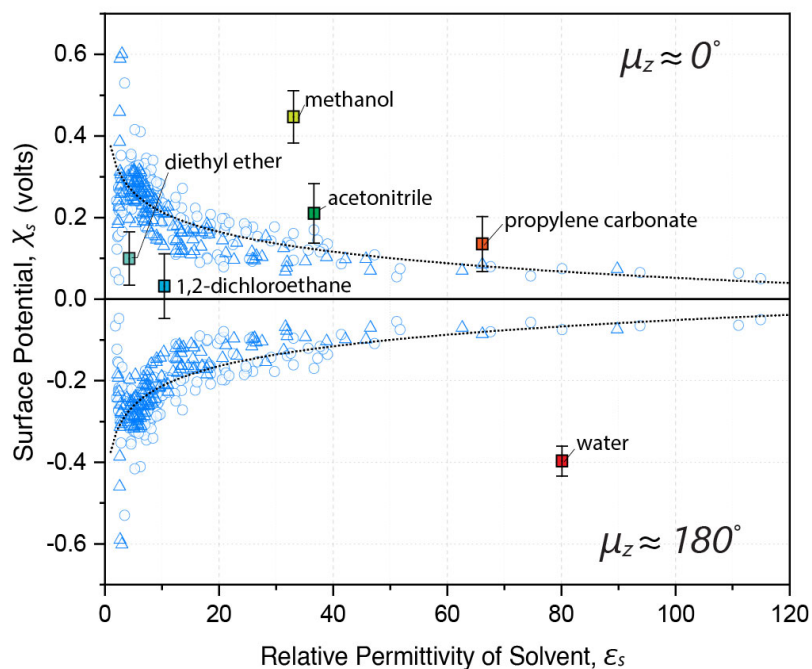
Figure 5-3. Surface potential response of over 300 solvents are shown with respect to dielectric constant (open symbols). Measured surface electrical potential values of 6 solvents represented by filled squares. Error bars indicate std. dev. of n≥4 trials. Estimates for the surface potential response were based on the solvent dielectric and permanent dipole moments (taken from the CRC Handbook). Dipole moment data used with eqn. 5-1 are based on the gas phase (open circles) and the liquid phase (open triangles) and used to establish a fitted boundary (dotted line) in the positive and negative potential region.

Table 5-3. Relative permittivity (ε_S), density (ρ), dipole moments (D), predicted dipolar surface potentials (V_D), and the measurable surface potential (V_M) of select neat solvents including water.

Solvent	ε_S	ρ	μ	V_D	V_M
g/mol		g/cm³	D	volts	volts
Diethyl ether (74.12)	4.3	0.71	1.01 (g)	0.26	+0.10 ± 0.07
1,2- Dichloroethane (98.96)	10.4	1.24	1.83 (l)	0.21	+0.03 ± 0.08
Methanol (32.04)	33.0	0.79	1.68 (g)	0.10	+0.45 ± 0.06
Acetonitrile (41.05)	36.6	0.78	3.91 (g)	0.17	+0.21 ± 0.07
Propylene carbonate (102.1)	66.1	1.20	4.9 (l)	0.09	+0.14 ± 0.07
Water (18.02)	80.1	0.99	1.85 (g)	0.08	-0.40 ± 0.04
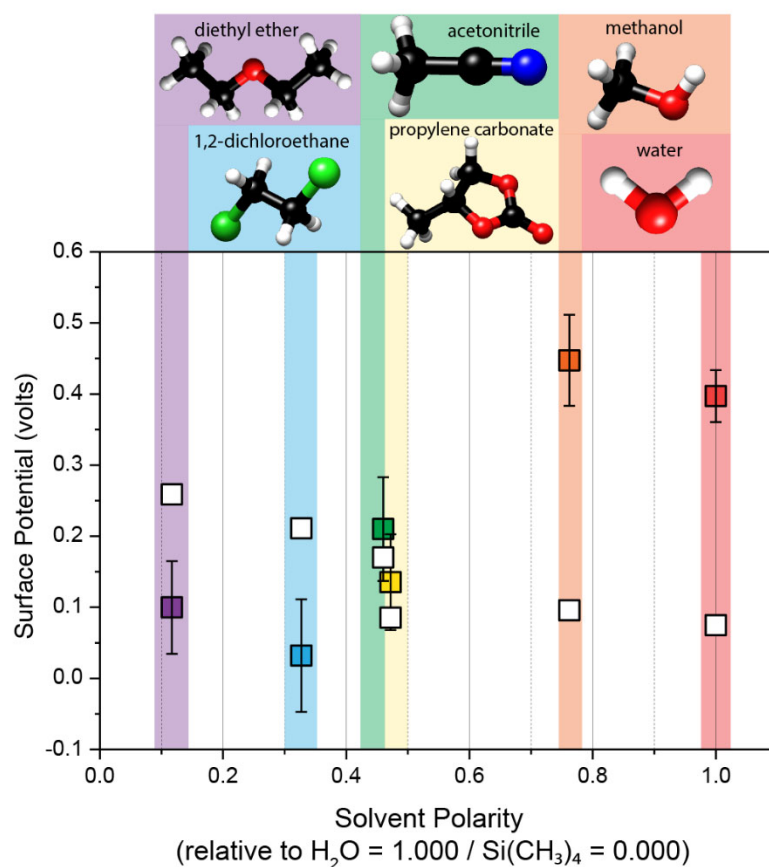
Figure 5-4. Surface potentials for 6 solvents (absolute value for convenience) measured V_M (closed) and expected dipolar potential V_D (open symbols) plotted against the relative solvent polarity (Reichardt scale). Aprotic acetonitrile and propylene carbonate orient at 0° relative to the surface normal (highly dipolar) compared to non-polar diethyl ether and 1,2-dichloroethane that orient closer to 90°. The nonconformity of the protic solvents methanol and water indicates substantial contribution from sources other than dipolar alignment; their surface orientation remains unclear.

5.3.3 Dipolar vs. Quadrupolar Contributions

Although it is widely accepted that there is a prevalent orientation of molecules in the surface layer, there is still no consensus on the exact sign and value of the surface potential of water.[117] Our previous[96] and current (as of this study) results for χ_{H_2O} is within similar range (in sign) and magnitude of χ_{H_2O} values predicted by quantum mechanical water models[4,60,67,68] (Figure 5-1). With respect to the sign and magnitude of the measured potential, the ionizing potential yields surface potentials that are higher and of the opposite sign to potentials measured with the Kenrick cell (Table 5-2). Despite arguments supporting the connection between the sign of χ to the molecular orientation of surface dipoles, the results of this study suggest that evoking a purely dipolar interpretation to measured potentials is far too limiting in application to our ionizing surface potential measurements. Therefore, we recommend a broader but microscopic perspective (with theoretical rigor) is also necessary to interpret surface potential measurements.

To interpret surface potential at the gas–liquid interface, a molecular perspective of the dipolar and quadrupolar contributions to the observable surface potential is essential. In their models, Sokhan and Tildesley[68] and others[3,4,46,60,83] have proposed that the calculated χ_{H_2O} is a net contribution of dipolar and quadrupolar moment of interfacial water molecules. Interfacial dipoles have also been described as an induced property from the ordering of interfacial quadrupoles,[83] and thusly have a significant part in surface potential response. Even so, any theoretical estimates of χ_{H_2O} is notoriously challenging. Kathmann and co-workers[3,209] have appropriately noted the ambiguity in defining the vapor-liquid potential boundary with partial charge models of interfacial water. From coupling AIMD with electron holography measurements[3] yields a surface potential of +3.1 V for liquid water. Electron holography, in contrast to electrochemical measurements, probes the averaged electrostatic potential field across an experimentally defined air–water interface.[3,209] However, these results, do not shed light on the interfacial arrangement of

dipoles and quadrupoles, and therefore do not fully characterize the apparent molecular structure specific to the interfacial environment experienced by a solute or surfactant. As a result, there are limited experimental means by which to explore and/or compare a unified understanding of dipolar and quadrupolar components of the observable surface potential.

5.4 Conclusions

The solubility of ionic species in water and nonaqueous solvents continues to receive considerable attention in recent years. The molecular structure of their interfaces, particularly the gas–liquid, vary significantly and impart unique physicochemical characteristics for ion solvation. Herein, we present fresh ionizing surface potential measurements for water, methanol, acetonitrile, propylene carbonate, 1.2-dichloroethane, and diethyl ether. To assess the contributions of the interfacial dipolar moment to the surface charge of these solvents, we proposed a Helmholtz model that predicted surface potentials solely based on the molecular orientation of the dipoles. In comparing our measurements with the predicted outcomes, we show the divergent nature of protic methanol and water from a proposed dipolar surface potential model while confirming the unique and highly dipolar nature of pure acetonitrile and propylene carbonate liquid surfaces. In contrast, the nonpolar diethyl ether and 1,2-dichloroethane are interpreted to align their dipoles parallel to the surface normal. We discuss possible solvent factors that dictate the observable surface potential, most notably the autoprotolytic abilities of methanol and water. Additionally, we also present a summary of literature concerning surface potentials of the neat air/water interface to our current measurement of neat water and a discussion on the dipolar and quadrupolar contributions to the surface potential. Interpreting surface potential at the gas–liquid interface requires a unified treatment of the dipolar and quadrupolar contributions to the observable surface potential across multiple electrochemical and non-electrochemical techniques.

94

Chapter 6. Conclusion & Outlook

Studies presented here reflect the scope and complexity of the ionizing surface potential method beginning with the initial measurement and the subsequent interpretation of results for gas–liquid interfaces. Herein, we presented a detailed overview of surface potentials, the principle, and the methodology of the ionizing surface potential. Using circuit model analysis, we showed the closeness in results between the predicted surface tension and the derived from the real-time surface potential measurements. Thus, validating the use of this technique to measure the surface electric potentials at the gas–liquid interface. However, understanding the impact of the type of counter electrode (Pt vs. Au) and the ionizing gas environment (N_2 vs. Ar vs. He) warrants future studies that focus on the standardization of measurements and within various environments. Moreover, any series of standardization measurements must go beyond the configuration used with ISPS.

With measurements of aqueous sodium halide solutions that provide a fresh perspective on the influence of surface enriched halides at the air–water interface. The surface potential values were reported without the utilization of prior methods using obscurely derived χ_{water} values as a standard reference due to the inherent weakness and probable inaccurate estimations arising from such. Surfactant calibrants offer a better understanding of the nature of aqueous halide salts and their inherently generated electric fields. Though ionic surfactants remain a convenient choice for calibration, surfactants with a wider difference in the potential range must also be explored as potential calibrants, particularly as ionic surfactants are difficult to simulate within theoretical models at high concentrations ($>\mu$m range).

From the adsorption properties of aqueous halides explored in this work, there is yet more to discover about their behavior with more extended concentration ranges and in complex mixtures (e.g., seas, oceans, rivers). Despite this work being limited to a small range of concentrations, halide enrichment observed for bromide (>2 mol/kg water), correlates to its bulk concentration to some extent. Yet, concentration is only one parameter; temperature effects are relatively less explored.[178] Additionally, there is a need for understanding halide surface adsorption in complex mixtures, not only with other inorganic salts in purely ionic electrolytes solutions but also those with soluble organics. Indeed, much of the current research suggests larger surface enrichment factors for heavier halides (e.g., bromide) in mixed solutions.[12,37] With these considerations, ionizing surface potential measurements on mixed halide solutions might provide estimable features on a presumptive electric field inversion at their air–solution interface.

Interpretation of surface potentials of nonaqueous solvent is not trivial. Although there is a relative agreement between measuring potentials from ionizing cells to theoretical models, the contribution from the quadrupole to the observable surface potential. A unified treatment of the dipolar and quadrupolar contributions to the observable surface potential is necessary to attaining the absolute or standard surface potential (relative to known material) across various electrochemical and non-electrochemical techniques.

Additionally, despite the developments in analysis and reporting of surface potential values as described here, surface potential measurement is tedious; thus, the technology would benefit from further development.[94,96] We believe that there are additional avenues for technological advancements for the radioactive ionizing electrode materials and methodologies to advance interpretation. We also assert that there remains a substantial gap for relating theoretical surface potential values with those experimentally measured. Closing this gap will entail a more dedicated effort of theoretical and experimental collaborations.

Bibliography

(1)   Conway, B. E. The State of Water and Hydrated Ions at Interfaces. *Adv. Colloid Interface Sci.* **1977**, *8* (2–3), 91–211. https://doi.org/10.1016/0001-8686(77)80009-2.

(2)   Eisenthal, K. B. Liquid Interfaces Probed by Second-Harmonic and Sum-Frequency Spectroscopy. *Chem. Rev.* **1996**, *96* (4), 1343–1360. https://doi.org/10.1021/cr9502211.

(3)   Kathmann, S. M.; William Kuo, I.-F.; Mundy, C. J.; Schenter, G. K. Understanding the Surface Potential of Water. *J. Phys. Chem. B* **2011**, *115*, 4369–4377. https://doi.org/10.1021/jp1116036.

(4)   Kathmann, S. M.; Kuo, I. F. W.; Mundy, C. J. Electronic Effects on the Surface Potential at the Vapor-Liquid Interface of Water. *J. Am. Chem. Soc.* **2008**, *130* (49), 16556–16561. https://doi.org/10.1021/ja802851w.

(5)   Benjamin, I. *Chemical Reactions and Solvation at Liquid Interfaces: A Microscopic Perspective*; 1996. https://doi.org/10.1021/CR950230.

(6)   Physical Constants of Organic Compounds. In *CRC Handbook of Chemistry and Physics*; Rumble, J. R., Ed.; CRC Press/Taylor & Francis: Boca Raton, FL, 2020.

(7)   Knipping, E. M.; Lakin, M. J.; Foster, K. L.; Jungwirth, P.; Tobias, D. J.; Gerber, R. B.; Dabdub, D.; Finlayson-Pitts, B. J. Experiments and Simulations of Ion-Enhanced Interfacial Chemistry on Aqueous NaCl Aerosols. *Science (80-.).* **2000**, *288* (5464), 301–306. https://doi.org/10.1126/science.288.5464.301.

(8)   Katrib, Y.; Deiber, G.; Schweitzer, F.; Mirabel, P.; George, C. *Chemical Transformation of Bromine Chloride at the Air/Water Interface*; 2001.

(9)   Clifford, D.; Donaldson, D. J. Direct Experimental Evidence for a Heterogeneous Reaction of Ozone with Bromide at the Air-Aqueous Interface. *J. Phys. Chem. A* **2007**, *111* (39), 9809–9814. https://doi.org/10.1021/jp074315d.

(10)   Laskin, A.; Wang, H.; Robertson, W. H.; Cowin, J. P.; Ezell, M. J.; Finlayson-Pitts, B. J.; Wiley, W. R. A New Approach to Determining Gas-Particle Reaction Probabilities and Application to the Heterogeneous Reaction of Deliquesced Sodium Chloride Particles with Gas-Phase Hydroxyl Radicals. **2006**. https://doi.org/10.1021/jp063263.

(11)   Graham, J. D.; Roberts, J. T.; Anderson, L. D.; Grassian, V. H. The 367 Nm Photochemistry of OClO Thin Films and OClO Absorbed on Ice. *J. Phys. Chem.* **1996**, *100* (50), 19551–19558. https://doi.org/10.1021/jp962054u.

(12)   Gladich, I.; Shepson, P. B.; Carignano, M. A.; Szleifer, I. Halide Affinity for the Water-Air Interface in Aqueous Solutions of Mixtures of Sodium Salts. *J. Phys. Chem. A* **2011**, *115* (23), 5895–5899. https://doi.org/10.1021/jp110208a.

(13)   Griffith, E. C.; Vaida, V. In Situ Observation of Peptide Bond Formation at the Water-Air Interface. *Proc. Natl. Acad. Sci. U. S. A.* **2012**, *109* (39), 15697–15701. https://doi.org/10.1073/pnas.1210029109.

(14)   Giberti, F.; Hassanali, A. A. The Excess Proton at the Air-Water Interface: The Role of Instantaneous Liquid Interfaces. *J. Chem. Phys.* **2017**, *146* (24), 244703. https://doi.org/10.1063/1.4986082.

(15)   Zhao, X.; Subrahmanyan, S.; Eisenthal, K. B. Determination of PKa at the Air/Water Interface by Second Harmonic Generation. *Chem. Phys. Lett.* **1990**, *171* (5–6), 558–562. https://doi.org/10.1016/0009-2614(90)85263-C.

(16)   Bianco, R.; Wang, S.; Hynes, J. T. Infrared Signatures of HNO_3 and NO_3^- at a Model Aqueous Surface. A Theoretical Study. *J. Phys. Chem. A* **2008**, *112* (39), 9467–9476. https://doi.org/10.1021/jp802563g.

(17)   Venkateshwaran, V.; Vembanur, S.; Garde, S. Water-Mediated Ion-Ion Interactions Are Enhanced at the Water Vapor-Liquid Interface. *Proc. Natl. Acad. Sci. U. S. A.* **2014**, *111* (24), 8729–8734. https://doi.org/10.1073/pnas.1403294111.

(18)   Kattirtzi, J. A.; Limmer, D. T.; Willard, A. P. Microscopic Dynamics of Charge Separation at the Aqueous Electrochemical Interface. *Proc. Natl. Acad. Sci. U. S. A.* **2017**, *114* (51), 13374–13379. https://doi.org/10.1073/pnas.1700093114.

(19)   Shen, Y. R. Surface Properties Probed by Second-Harmonic and Sum-Frequency Generation. *Nature* **1989**, *337* (6207), 519–525. https://doi.org/10.1038/337519a0.

(20)   Shen, Y. R.; Ostroverkhov, V. Sum-Frequency Vibrational Spectroscopy on Water Interfaces: Polar Orientation of Water Molecules at Interfaces. *Chem. Rev.* **2006**, *106* (4), 1140–1154. https://doi.org/10.1021/cr040377d.

(21)   Ostroverkhov, V.; Waychunas, G. A.; Shen, Y. R. New Information on Water Interfacial Structure Revealed by Phase-Sensitive Surface Spectroscopy. *Phys. Rev. Lett.* **2005**, *94* (4), 046102. https://doi.org/10.1103/PhysRevLett.94.046102.

(22)   Pezzotti, S.; Galimberti, D. R.; Gaigeot, M. P. 2D H-Bond Network as the Topmost Skin to the Air-Water Interface. *J. Phys. Chem. Lett.* **2017**, *8* (13), 3133–3141. https://doi.org/10.1021/acs.jpclett.7b01257.

(23)   Pezzotti, S.; Serva, A.; Gaigeot, M. P. 2D-HB-Network at the Air-Water Interface: A Structural and Dynamical Characterization by Means of Ab Initio and Classical Molecular Dynamics Simulations. *J. Chem. Phys.* **2018**, *148* (17), 130901. https://doi.org/10.1063/1.5018096.

(24)   Pezzotti, S.; Gaigeot, M. P. Spectroscopic BIL-SFG Invariance Hides the Chaotropic Effect of Protons at the Air-Water Interface. *Atmosphere (Basel).* **2018**, *9* (10), 396. https://doi.org/10.3390/atmos9100396.

(25)   Heydweiller, A. Über Physikalische Eigenschaften von Lösungen in Ihrem Zusammenhang. II. Oberflächenspannung Und Elektrisches Leitvermögen Wässeriger Salzlösungen. *Ann. Phys.* **1910**, *338* (11), 145–185. https://doi.org/10.1002/andp.19103381108.

(26)   Wagner, C. He Surface Tension of Dilute Solutions of Electrolytes. *Phys. Z.* **1924**, 474–

477.

(27) Onsager, L.; Samaras, N. N. T. The Surface Tension of Debye-Hückel Electrolytes. *J. Chem. Phys.* **1934**, *2* (8), 528–536. https://doi.org/10.1063/1.1749522.

(28) Pegram, L. M.; Record, M. T. Partitioning of Atmospherically Relevant Ions between Bulk Water and the Water/Vapor Interface. *Proc. Natl. Acad. Sci.* **2006**, *103* (39), 14278–14281. https://doi.org/10.1073/pnas.0606256103.

(29) Collins, K. D.; Washabaugh, M. W. The Hofmeister Effect and the Behaviour of Water at Interfaces. *Q. Rev. Biophys.* **1985**, *18* (4), 323–422. https://doi.org/10.1017/S0033583500005369.

(30) Jungwirth, P.; Cremer, P. S. Beyond Hofmeister. *Nat. Chem.* **2014**, *6* (4), 261–263. https://doi.org/10.1038/nchem.1899.

(31) Zhang, Y.; Cremer, P. S. Chemistry of Hofmeister Anions and Osmolytes. *Annu. Rev. Phys. Chem.* **2010**, *61*, 63–83. https://doi.org/10.1146/annurev.physchem.59.032607.093635.

(32) Jungwirth, P.; Tobias, D. J. Molecular Structure of Salt Solutions: A New View of the Interface with Implications for Heterogeneous Atmospheric Chemistry. *J. Phys. Chem. B* **2001**, *105* (43), 10468–10472. https://doi.org/10.1021/jp012750g.

(33) Jungwirth, P.; Tobias, D. J. Ions at the Air/Water Interface. *J. Phys. Chem. B* **2002**, *106*, 6361–6373. https://doi.org/10.1021/jp020242g.

(34) Flores, S. C.; Kherb, J.; Cremer, P. S. Direct and Reverse Hofmeister Effects on Interfacial Water Structure. *J. Phys. Chem. C* **2012**, *116* (27), 14408–14413. https://doi.org/10.1021/jp3029352.

(35) Jungwirth, P.; Tobias, D. J. Specific Ion Effects at the Air/Water Interface. *Chem. Rev.* **2006**, *106* (4), 1259–1281. https://doi.org/10.1021/cr0403741.

(36) Netz, R. R.; Horinek, D. Progress in Modeling of Ion Effects at the Vapor/Water Interface. *Annu. Rev. Phys. Chem.* **2012**, *63* (1), 401–418. https://doi.org/10.1146/annurev-physchem-032511-143813.

(37) Tobias, D. J.; Stern, A. C.; Baer, M. D.; Levin, Y.; Mundy, C. J. Simulation and Theory of Ions at Atmospherically Relevant Aqueous Liquid-Air Interfaces. *Annu. Rev. Phys. Chem.* **2013**, *64* (1), 339–359. https://doi.org/10.1146/annurev-physchem-040412-110049.

(38) Levin, Y.; Dos Santos, A. P. Ions at Hydrophobic Interfaces. *J. Phys. Condens. Matter* **2014**, *26* (20), 203101. https://doi.org/10.1088/0953-8984/26/20/203101.

(39) Liu, D.; Ma, G.; Levering, L. M.; Allen, H. C. Vibrational Spectroscopy of Aqueous Sodium Halide Solutions and Air-Liquid Interfaces: Observation of Increased Interfacial Depth. *J. Phys. Chem. B* **2004**, *108* (7), 2252–2260. https://doi.org/10.1021/jp036169r.

(40) Gopalakrishnan, S.; Jungwirth, P.; Tobias, D. J.; Allen, H. C. Air-Liquid Interfaces of Aqueous Solutions Containing Ammonium and Sulfate: Spectroscopic and Molecular Dynamics Studies. *J. Phys. Chem. B* **2005**, *109* (18), 8861–8872. https://doi.org/10.1021/jp0500236.

(41) Mucha, M.; Frigato, T.; Levering, L. M.; Allen, H. C.; Tobias, D. J.; Dang, L. X.;

Jungwirth, P. Unified Molecular Picture of the Surfaces of Aqueous Acid, Base, and Salt Solutions. *J. Phys. Chem. B* **2005**, *109* (16), 7617–7623. https://doi.org/10.1021/jp0445730.

(42) Raymond, E. A.; Richmond, G. L. Probing the Molecular Structure and Bonding of the Surface of Aqueous Salt Solutions. *J. Phys. Chem. B* **2004**, *108* (16), 5051–5059. https://doi.org/10.1021/jp037725k.

(43) Petersen, P. B.; Saykally, R. J. On the Nature of Ions at the Liquid Water Surface. *Annu. Rev. Phys. Chem* **2006**, *57*, 333–364. https://doi.org/10.1146/annurev.physchem.57.032905.104609.

(44) Onorato, R. M.; Otten, D. E.; Saykally, R. J. Measurement of Bromide Ion Affinities for the Air/Water and Dodecanol/Water Interfaces at Molar Concentrations by UV Second Harmonic Generation Spectroscopy. *J. Phys. Chem. C* **2010**, *114* (32), 13746–13751. https://doi.org/10.1021/jp103454r.

(45) Gladich, I.; Chen, S.; Vazdar, M.; Boucly, A.; Yang, H.; Ammann, M.; Artiglia, L. Surface Propensity of Aqueous Atmospheric Bromine at the Liquid-Gas Interface. *J. Phys. Chem. Lett.* **2020**, *11* (9), 3422–3429. https://doi.org/10.1021/acs.jpclett.0c00633.

(46) Beck, T. L. The Influence of Water Interfacial Potentials on Ion Hydration in Bulk Water and near Interfaces. **2013**. https://doi.org/10.1016/j.cplett.2013.01.008.

(47) Arslanargin, A.; Beck, T. L. Free Energy Partitioning Analysis of the Driving Forces That Determine Ion Density Profiles near the Water Liquid-Vapor Interface. *J. Chem. Phys.* **2012**, *136* (10), 104503. https://doi.org/10.1063/1.3689749.

(48) Fulton, J. L.; Schenter, G. K.; Baer, M. D.; Mundy, C. J.; Dang, L. X.; Balasubramanian, M. Probing the Hydration Structure of Polarizable Halides: A Multiedge XAFS and Molecular Dynamics Study of the Iodide Anion. *J. Phys. Chem. B* **2010**, *114* (40), 12926–12937. https://doi.org/10.1021/jp106378p.

(49) Baer, M. D.; Stern, A. C.; Levin, Y.; Tobias, D. J.; Mundy, C. J. Electrochemical Surface Potential Due to Classical Point Charge Models Drives Anion Adsorption to the Air-Water Interface. *J. Phys. Chem. Lett.* **2012**, *3* (11), 1565–1570. https://doi.org/10.1021/jz300302t.

(50) Stern, A. C.; Baer, M. D.; Mundy, C. J.; Tobias, D. J. Thermodynamics of Iodide Adsorption at the Instantaneous Air-Water Interface. *J. Chem. Phys.* **2013**, *138* (11), 114709. https://doi.org/10.1063/1.4794688.

(51) Hua, W.; Verreault, D.; Huang, Z.; Adams, E. M.; Allen, H. C. Cation Effects on Interfacial Water Organization of Aqueous Chloride Solutions. I. Monovalent Cations: Li+, Na+, K+, and NH4+. *J. Phys. Chem. B* **2014**, *118* (28), 8433–8440. https://doi.org/10.1021/jp503132m.

(52) Hua, W.; Verreault, D.; Adams, E. M.; Huang, Z.; Allen, H. C. Impact of Salt Purity on Interfacial Water Organization Revealed by Conventional and Heterodyne-Detected Vibrational Sum Frequency Generation Spectroscopy. *J. Phys. Chem. C* **2013**, *117* (38), 19577–19585. https://doi.org/10.1021/jp408146t.

(53) Hua, W.; Verreault, D.; Allen, H. C. Surface Prevalence of Perchlorate Anions at the Air/Aqueous Interface. *J. Phys. Chem. Lett.* **2013**, *4* (24), 4231–4236.

https://doi.org/10.1021/jz402009f.

(54) Gladich, I.; Chen, S.; Vazdar, M.; Boucly, A.; Yang, H.; Ammann, M.; Artiglia, L. Surface Propensity of Aqueous Atmospheric Bromine at the Liquid− Gas Interface. *J. Phys. Chem. Lett* **2020**, *11*, 3429. https://doi.org/10.1021/acs.jpclett.0c00633.

(55) Piatkowski, L.; Zhang, Z.; Backus, E. H. G.; Bakker, H. J.; Bonn, M. Extreme Surface Propensity of Halide Ions in Water. *Nat. Commun.* **2014**, *5* (1), 4083. https://doi.org/10.1038/ncomms5083.

(56) Finlayson-Pitts, B. J. Multiphase Chemistry in the Troposphere: It All Starts … and Ends … with Gases. *Int. J. Chem. Kinet.* **2019**, *51* (10), 736–752. https://doi.org/10.1002/kin.21305.

(57) Thomas, J. L.; Jimenez-Aranda, A.; Finlayson-Pitts, B. J.; Dabdub, D. Gas-Phase Molecular Halogen Formation from NaCl and NaBr Aerosols: When Are Interface Reactions Important? *J. Phys. Chem. A* **2006**, *110* (5), 1859–1867. https://doi.org/10.1021/jp054911c.

(58) Jungwirth, P.; Rosenfeld, D.; Buch, V. A Possible New Molecular Mechanism of Thundercloud Electrification. *Atmos. Res.* **2005**, *76* (1–4), 190–205. https://doi.org/10.1016/J.ATMOSRES.2004.11.016.

(59) Pegram, L. M.; Record, M. T. Thermodynamic Origin of Hofmeister Ion Effects. *J. Phys. Chem. B* **2008**, *112* (31), 9428–9436. https://doi.org/10.1021/jp800816a.

(60) Wilson, M. A.; Pohorille, A.; Pratt, L. R. Surface Potential of the Water Liquid–Vapor Interface. *J. Chem. Phys.* **1988**, *88* (5), 3281–3285. https://doi.org/10.1063/1.453923.

(61) Stillinger, F. H.; Ben-Naim, A. Liquid-Vapor Interface Potential for Water. *J. Chem. Phys.* **1967**, *47* (11), 4431–4437. https://doi.org/10.1063/1.1701649.

(62) Matsumoto, M.; Kataoka, Y. Study on Liquid–Vapor Interface of Water. I. Simulational Results of Thermodynamic Properties and Orientational Structure. *J. Chem. Phys.* **1988**, *88* (5), 3233–3245. https://doi.org/10.1063/1.453919.

(63) Shi, Y.; Beck, T. L. Absolute Ion Hydration Free Energy Scale and the Surface Potential of Water via Quantum Simulation. *Proc. Natl. Acad. Sci.* **2020**, *117* (48), 30151–30158. https://doi.org/10.1073/PNAS.2017214117.

(64) Ishiyama, T.; Morita, A. Molecular Dynamics Study of Gas - Liquid Aqueous Sodium Halide Interfaces. II. Analysis of Vibrational Sum Frequency Generation Spectra. *J. Phys. Chem. C* **2007**, *111* (2), 738–748. https://doi.org/10.1021/jp065192k.

(65) Wick, C. D.; Dang, L. X.; Jungwirth, P. Simulated Surface Potentials at the Vapor-Water Interface for the KCl Aqueous Electrolyte Solution. *J. Chem. Phys.* **2006**, *125* (2), 024706. https://doi.org/10.1063/1.2218840.

(66) Dang, L. X. Computational Study of Ion Binding to the Liquid Interface of Water. *J. Phys. Chem. B* **2002**, *106* (40), 10388–10394. https://doi.org/10.1021/jp021871t.

(67) Christou, N. I.; Whitehouse, J. S.; Nicholson, D.; Parsonage, N. G. Studies of High Density Water Films by Computer Simulation. *Mol. Phys.* **1985**, *55* (2), 397–410. https://doi.org/10.1080/00268978500101421.

(68)   Sokhan, V. P.; Tildesley, D. J. The Free Surface of Water: Molecular Orientation, Surface Potential and Nonlinear Susceptibility. *Mol. Phys.* **1997**, *92* (4), 625–640. https://doi.org/10.1080/002689797169916.

(69)   Aloisi, G.; Guidelli, R.; Jackson, R. A.; Clark, S. M.; Barnes, P. The Structure of Water at a Neutral Interface. *J. Electroanal. Chem.* **1986**, *206* (1–2), 131–137. https://doi.org/10.1016/0022-0728(86)90262-7.

(70)   Ishiyama, T.; Morita, A. Computational Analysis of Vibrational Sum Frequency Generation Spectroscopy. *Annual Review of Physical Chemistry*. Annual Reviews Inc. May 5, 2017, pp 355–377. https://doi.org/10.1146/annurev-physchem-052516-044806.

(71)   Bu, W.; Schlossman, M. L. Synchrotron X-Ray Scattering from Liquid Surfaces and Interfaces. In *Synchrotron Light Sources and Free-Electron Lasers: Accelerator Physics, Instrumentation and Science Applications*; Springer International Publishing, 2016; pp 1579–1616. https://doi.org/10.1007/978-3-319-14394-1_45.

(72)   Pershan, P. S.; Schlossman, M. *Liquid Surfaces and Interfaces: Synchrotron X-Ray Methods*; Cambridge University Press, 2012; Vol. 9780521814. https://doi.org/10.1017/CBO9781139045872.

(73)   Adel, T.; Ng, K. C.; Vazquez de Vasquez, M. G.; Velez-Alvarez, J.; Allen, H. C. Insight into the Ionizing Surface Potential Method and Aqueous Sodium Halide Surfaces. *Langmuir* **2021**, *37*, 7863–7874. https://doi.org/10.1021/acs.langmuir.1c00465.

(74)   Stevens, G. W.; Perera, J. M.; Grieser, F. Metal Ion Extraction. *Curr. Opin. Colloid Interface Sci.* **1997**, *2* (6), 629–634. https://doi.org/10.1016/s1359-0294(97)80056-8.

(75)   *Solvent Extraction Principles and Practice, Revised and Expanded*, 2nd Editio.; Rydberg, J., Ed.; CRC Press, 2004. https://doi.org/10.1201/9780203021460.

(76)   Guyon, F.; Parthasarathy, N.; Buffle, J. Chemical Separation with Liquid Membranes: An Overview. *Fresenius J. Anal. Chem* **1990**, *11* (2), 1328–1333. https://doi.org/10.1021/ac991047.

(77)   Salomon, M. The Thermodynamics of Ion Solvation in Water and Propylene Carbonate. *J. Phys. Chem.* **1970**, *74* (12), 2519–2524. https://doi.org/10.1021/j100706a019.

(78)   You, X.; Chaudhari, M. I.; Pratt, L. R.; Pesika, N.; Aritakula, K. M.; Rick, S. W. Interfaces of Propylene Carbonate. *J. Chem. Phys.* **2013**, *138* (11), 114708. https://doi.org/10.1063/1.4794792.

(79)   Oss, C. J. V.; Good, R. J. Surface Tension and the Solubility of Polymers and Biopolymers: The Role of Polar and Apolar Interfacial Free Energies. *J. Macromol. Sci. Part A - Chem.* **1989**, *26* (8), 1183–1203. https://doi.org/10.1080/00222338908052041.

(80)   Mills, I.; Cvitas, T.; Homann, K.; Kallay, N.; Kuchitsu, K. *INTERNATIONAL UNION OF PURE AND APPLIED CHEMISTRY PHYSICAL CHEMISTRY DIVISION*.

(81)   Parsons, R. Equilibrium Properties of Electrified Interfaces. In *Modern aspects of electrochemistry, Vol. 1*; Butterworths: London, 1954; Vol. 1, pp 103–179.

(82)   Girault, H. H. *Analytical and Physical Electrochemistry*; EPFL Press, 2004. https://doi.org/10.1201/9781439807842.

(83)   Zhang, C.; Sprik, M. Electromechanics of the Liquid Water Vapour Interface. *Phys. Chem. Chem. Phys.* **2020**, *22* (19), 10676–10686. https://doi.org/10.1039/c9cp06901a.

(84)   Randles, J. E. B. Structure at the Free Surface of Water and Aqueous Electrolyte Solutions. *Phys. Chem. Liq.* **1977**, *7* (1–2), 107–179. https://doi.org/10.1080/00319107708084730.

(85)   Lange, E.; Miscenko, K. P. On the Thermodynamics of Ionic Solvation. *Z. Phys. Chem.* **1930**, *A149* (1).

(86)   Lange, E. Über Elektrochemische Grundbegriffe, Insbesondere Der Elektrode Metall/Lösung. *Zeitschrift für Elektrochemie und Angew. Phys. Chemie* **1951**, *55* (2), 76–92. https://doi.org/10.1002/BBPC.19510550204.

(87)   Randles, J. E. B. The Real Hydration Energies of Ions. *Trans. Faraday Soc.* **1956**, *52* (0), 1573–1581. https://doi.org/10.1039/tf9565201573.

(88)   Croxton, C. A. *Statistical Mechanics of the Liquid Surface*; John Wiley & Sons: New York, 1980.

(89)   Chen, S.; Dong, H.; Yang, J. Surface Potential/Charge Sensing Techniques and Applications. *Sensors (Switzerland)*. MDPI AG March 2, 2020, p 1690. https://doi.org/10.3390/s20061690.

(90)   Israelachvili, J. *Intermolecular and Surface Forces*; Elsevier Inc., 2011. https://doi.org/10.1016/C2009-0-21560-1.

(91)   Jarvis, N. L.; Scheiman, M. A. Surface Potentials of Aqueous Electrolyte Solutions. *J. Phys. Chem.* **1968**, *72* (1), 74–78. https://doi.org/10.1021/J100847a014.

(92)   Bewig, K. W. Ionization Method of Measuring Contact Potential Differences. *Rev. Sci. Instrum.* **1964**, *35* (9), 1160–1162. https://doi.org/10.1063/1.1718986.

(93)   Jarvis, N. L. Effect of Various Salts on the Surface Potential of the Water-Air Interface. *J. Geophys. Res.* **1972**, *77* (27), 5177–5182. https://doi.org/10.1029/jc077i027p05177.

(94)   Foulkes, F. R.; Graydon, W. F.; Garamszeghy, M. An Ionized Air Reference Electrode: I . Principles of Operation. *J. Electrochem. Soc.* **1984**, *131* (6), 1325–1332. https://doi.org/10.1149/1.2115813.

(95)   Steinhauser, G.; Buchtela, K. Gas Ionization Detectors. In *Handbook of Radioactivity Analysis*; L'Annunziata, M. F., Ed.; Elsevier, 2020; Vol. 1, pp 245–305. https://doi.org/10.1016/b978-0-12-814397-1.00002-9.

(96)   Adel, T.; Velez-Alvarez, J.; Co, A. C.; Allen, H. C. Circuit Analysis of Ionizing Surface Potential Measurements of Electrolyte Solutions. *J. Electrochem. Soc.* **2021**, *168* (1), 016507. https://doi.org/10.1149/1945-7111/abd649.

(97)   Reddy, S. K.; Thiraux, R.; Wellen Rudd, B. A.; Lin, L.; Adel, T.; Joutsuka, T.; Geiger, F. M.; Allen, H. C.; Morita, A.; Paesani, F. Bulk Contributions Modulate the Sum-Frequency Generation Spectra of Water on Model Sea-Spray Aerosols. *Chem* **2018**. https://doi.org/10.1016/j.chempr.2018.04.007.

(98)   Okur, H. I.; Drexler, C. I.; Tyrode, E.; Cremer, P. S.; Roke, S. The Jones−Ray Effect Is Not Caused by Surface-Active Impurities. *J. Phys. Chem. Lett* **2018**, *9*, 6739–6743.

https://doi.org/10.1021/acs.jpclett.8b02957.

(99) Bard, A. J.; Faulkner, L. R. *Electrochemical Methods : Fundamentals and Applications*; Wiley, 2001.

(100) Sawyer, D. T.; Sobkowiak, A.; Roberts, J. L. *Electrochemistry for Chemists, 2nd Edition*, Second Edi.; Wiley: New York, 1995.

(101) Frumkin, A. Phasengrenzkräfte Und Adsorption an Der Trennungsfläche Luft. Lösung Anorganischer Elektrolyte. *Zeitschrift für Phys. Chemie* **1924**, *109* (1), 34–48. https://doi.org/10.1515/zpch-1924-10903.

(102) Randles, J. E. B. The Interface Between Aqueous Electrolyte Solutions and the Gas Phase. In *Advances in Electrochemistry and Electrochemical Engineering, Vol. 3*; Delahay, P., Tobias, C. W., Eds.; Wiley: New York, 1963; pp 1–30.

(103) Randles, J. E. B.; Schiffrin, D. J. The Temperature-Dependence of the Surface Potential of Aqueous Electrolytes. *J. Electroanal. Chem.* **1965**, *10* (5–6), 480–484. https://doi.org/10.1016/0022-0728(65)80049-3.

(104) Farrell, J. R.; McTigue, P. Precise Compensating Potential Difference Measurements with a Voltaic Cell: The Surface Potential of Water. *J. Electroanal. Chem. Interfacial Electrochem.* **1982**, *139* (1), 37–56. https://doi.org/10.1016/0022-0728(82)85102-4.

(105) Nakahara, H.; Shibata, O.; Moroi, Y. Examination of Surface Adsorption of Cetyltrimethylammonium Bromide and Sodium Dodecyl Sulfate. *J. Phys. Chem. B* **2011**, *115*, 9077–9086. https://doi.org/10.1021/jp202940p.

(106) Barzyk, W.; Vuorinen, J. Application of the Vibrating Plate (VP) Technique to Measuring Electric Surface Potential, ΔV, of Solutions; the Flow Cell for Simultaneous Measurement of the ΔV and the Surface Pressure, Π. *Colloids Surfaces A Physicochem. Eng. Asp.* **2011**, *385* (1–3), 1–10. https://doi.org/10.1016/j.colsurfa.2011.03.067.

(107) Llopis, J. Surface Potential at Liquid Interfaces. In *Modern Aspects of Electrochemistry No. 6*; Bockris, J. O., Conway, B. E., Eds.; Springer US: Boston, MA, 1971; pp 91–158. https://doi.org/10.1007/978-1-4684-3000-4_2.

(108) Gaines, G. L. *Insoluble Monolayers at Liquid-Gas Interfaces*; Interscience Publishers: New York, NY, 1966.

(109) Harris, S. J.; Doust, C. E. Energy per Ion Pair Measurements in Pure Helium and Helium Mixtures. *Radiat. Res.* **1976**, *66* (1), 11–18. https://doi.org/10.2307/3574351.

(110) Hurst, G. S.; Bortner, T. E.; Glick, R. E. Ionization and Excitation of Argon with Alpha Particles. *J. Chem. Phys.* **1965**, *42* (2), 713–719. https://doi.org/10.1063/1.1695995.

(111) Murray, R. L.; Holbert, K. E. Radiation and Materials. In *Nuclear Energy*; Elsevier, 2020; pp 81–99. https://doi.org/10.1016/b978-0-12-812881-7.00005-8.

(112) WOOD, J. RADIATION QUANTITIES AND UNITS. In *Computational Methods in Reactor Shielding*; Elsevier, 1982; pp 16–55. https://doi.org/10.1016/b978-0-08-028685-3.50005-8.

(113) Rutherford, E. *Radioactive Substances and Their Radiations*; The University Press, 1913.

(114) Holze, R. *Electrochemical Thermodynamics and Kinetics*; Lechner, M. D., Ed.; Springer-

Verlag: Berlin Heidelberg, 2007. https://doi.org/10.1007/978-3-540-45316-1_21.

(115) Parfenyuk, V. I. Surface Potential at the Gas–Aqueous Solution Interface. *Colloid J.* **2002**, *64* (5), 588–595. https://doi.org/10.1023/A:1020614010528.

(116) Paluch, M. Electrical Properties of Free Surface of Water and Aqueous Solutions. *Advances in Colloid and Interface Science*. Elsevier Science Publishers B.V. January 1, 2000, pp 27–45. https://doi.org/10.1016/S0001-8686(99)00014-7.

(117) Paluch, M. Surface Potential at the Water-Air Interface. *Surf. potential water-air interface* **2016**, *70* (2), 1. https://doi.org/10.17951/aa.2015.70.2.1.

(118) Dos Santos, A. P.; Diehl, A.; Levin, Y. Surface Tensions, Surface Potentials, and the Hofmeister Series of Electrolyte Solutions. *Langmuir* **2010**, *26* (13), 10778–10783. https://doi.org/10.1021/la100604k.

(119) Adam, N. K. *The Physics and Chemistry of Surfaces*; Clarendon Press: London, 1930.

(120) Parsons, R. The Electrical Double Layer: Recent Experimental and Theoretical Developments. *Chem. Rev.* **1990**, *90* (5), 813–826. https://doi.org/10.1021/cr00103a008.

(121) Andrews, D. G. H. A Novel Experiment to Investigate the Attenuation of Alpha Particles in Air. *Eur. J. Phys.* **2008**, *29* (5), 1077. https://doi.org/10.1088/0143-0807/29/5/019.

(122) Jones, E.; Oliphant, T.; Peterson, P. SciPy: Open Source Scientific Tools for Python, 2001. 2016.

(123) Bockris, J. O.; Reddy, A. K. N.; Bockris, J. O.; Reddy, A. K. N. The Electrified Interface. In *Volume 2 Modern Electrochemistry*; Springer US, 1970; pp 623–843. https://doi.org/10.1007/978-1-4613-4560-2_1.

(124) Kamcev, J.; Sujanani, R.; Jang, E.-S.; Yan, N.; Moe, N.; Paul, D. R.; Freeman, B. D. Salt Concentration Dependence of Ionic Conductivity in Ion Exchange Membranes. **2017**. https://doi.org/10.1016/j.memsci.2017.10.024.

(125) Lundquist, R. V.; Lewis, R. W. Conductivity of Sodium Sulfate Solutions Containing Sodium Hydroxide or Sulfuric Acid. *Ind. Eng. Chem. - Chem. Eng. Data Ser.* **1957**, *2* (1), 69–72. https://doi.org/10.1021/i460002a019.

(126) Vargaftik, N. B.; Volkov, B. N.; Voljak, L. D. International Tables of the Surface Tension of Water. *J. Phys. Chem. Ref. Data* **1983**, *12* (3), 817–820. https://doi.org/10.1063/1.555688.

(127) Chen, Y.; Okur, H. I.; Gomopoulos, N.; Macias-Romero, C.; Cremer, P. S.; Petersen, P. B.; Tocci, G.; Wilkins, D. M.; Liang, C.; Ceriotti, M.; Roke, S. Electrolytes Induce Long-Range Orientational Order and Free Energy Changes in the H-Bond Network of Bulk Water. *Sci. Adv.* **2016**, *2* (4), e1501891. https://doi.org/10.1126/sciadv.1501891.

(128) Duignan, T. T.; Peng, M.; Nguyen, A. V.; Zhao, X. S.; Baer, M. D.; Mundy, C. J. Detecting the Undetectable: The Role of Trace Surfactant in the Jones-Ray Effect. *J. Chem. Phys.* **2018**, *149* (19), 194702. https://doi.org/10.1063/1.5050421.

(129) Ishiyama, T.; Morita, A. Molecular Dynamics Study of Gas-Liquid Aqueous Sodium Halide Interfaces. I. Flexible and Polarizable Molecular Modeling and Interfacial Properties. *J. Phys. Chem. C* **2007**, *111* (2), 721–737. https://doi.org/10.1021/jp065191s.

(130) Bian, H. T.; Feng, R. R.; Xu, Y. Y.; Guo, Y.; Wang, H. F. Increased Interfacial Thickness of the NaF, NaCl and NaBr Salt Aqueous Solutions Probed with Non-Resonant Surface Second Harmonic Generation (SHG). *Phys. Chem. Chem. Phys.* **2008**, *10* (32), 4920–4931. https://doi.org/10.1039/b806362a.

(131) Levering, L. M.; Roxana Sierra-Hernández, M.; Allen, H. C. Observation of Hydronium Ions at the Air-Aqueous Acid Interface: Vibrational Spectroscopic Studies of Aqueous HCl, HBr, and HI. *J. Phys. Chem. C* **2007**, *111* (25), 8814–8826. https://doi.org/10.1021/jp065694y.

(132) Petersen, P. B.; Saykally, R. J. Probing the Interfacial Structure of Aqueous Electrolytes with Femtosecond Second Harmonic Generation Spectroscopy. *J. Phys. Chem. B* **2006**, *110* (29), 14060–14073. https://doi.org/10.1021/jp0601825.

(133) Götte, L.; Parry, K. M.; Hua, W.; Verreault, D.; Allen, H. C.; Tobias, D. J. Solvent-Shared Ion Pairs at the Air-Solution Interface of Magnesium Chloride and Sulfate Solutions Revealed by Sum Frequency Spectroscopy and Molecular Dynamics Simulations. *J. Phys. Chem. A* **2017**, *121* (34), 6450–6459. https://doi.org/10.1021/acs.jpca.7b05600.

(134) Tobias, D. J.; Jungwirth, P.; Parrinello, M. Surface Solvation of Halogen Anions in Water Clusters: An *Ab Initio* Molecular Dynamics Study of the Cl−(H2O)6 Complex. *J. Chem. Phys.* **2001**, *114* (16), 7036–7044. https://doi.org/10.1063/1.1360200.

(135) Jungwirth, P.; Curtis, J. E.; Tobias, D. J. Polarizability and Aqueous Solvation of the Sulfate Dianion. *Chem. Phys. Lett.* **2003**, *367* (5–6), 704–710. https://doi.org/10.1016/S0009-2614(02)01782-7.

(136) Dang, L. X.; Chang, T.-M. Molecular Dynamics Study of Water Clusters, Liquid, and Liquid–Vapor Interface of Water with Many-Body Potentials. *J. Chem. Phys.* **1998**, *106* (19), 8149. https://doi.org/10.1063/1.473820.

(137) Peng, M.; Duignan, T. T.; Zhao, X. S.; Nguyen, A. V. Surface Potential Explained: A Surfactant Adsorption Model Incorporating Realistic Layer Thickness. *J. Phys. Chem. B* **2020**, *124* (15), 3195–3205. https://doi.org/10.1021/acs.jpcb.0c00278.

(138) Garland, J. A.; Curtis, H. Emission of Iodine from the Sea Surface in the Presence of Ozone. *J. Geophys. Res.* **1981**, *86* (C4), 3183. https://doi.org/10.1029/JC086iC04p03183.

(139) Sakamoto, Y.; Yabushita, A.; Kawasaki, M.; Enami, S. Direct Emission of I 2 Molecule and IO Radical from the Heterogeneous Reactions of Gaseous Ozone with Aqueous Potassium Iodide Solution. *J. Phys. Chem. A* **2009**, *113* (27), 7707–7713. https://doi.org/10.1021/jp903486u.

(140) Hayase, S.; Yabushita, A.; Kawasaki, M.; Enami, S.; Hoffmann, M. R.; Colussi, A. J. Heterogeneous Reaction of Gaseous Ozone with Aqueous Iodide in the Presence of Aqueous Organic Species. *J. Phys. Chem. A* **2010**, *114* (19), 6016–6021. https://doi.org/10.1021/jp101985f.

(141) Hayase, S.; Yabushita, A.; Kawasaki, M.; Enami, S.; Hoffmann, M. R.; Colussi, A. J. Weak Acids Enhance Halogen Activation on Atmospheric Waters Surfaces. *J. Phys. Chem. A* **2011**, *115* (19), 4935–4940. https://doi.org/10.1021/jp2021775.

(142) Foster, K. L.; Plastridge, R. A.; Bottenheim, J. W.; Shepson, P. B.; Finlayson-Pitts, B. J.; Spicer, C. W. The Role of Br2 and Brcl in Surface Ozone Destruction at Polar Sunrise.

Science (80-.). **2001**, *291* (5503), 471–474. https://doi.org/10.1126/science.291.5503.471.

(143) Pratt, K. A.; Custard, K. D.; Shepson, P. B.; Douglas, T. A.; Pöhler, D.; General, S.; Zielcke, J.; Simpson, W. R.; Platt, U.; Tanner, D. J.; Gregory Huey, L.; Carlsen, M.; Stirm, B. H. Photochemical Production of Molecular Bromine in Arctic Surface Snowpacks. *Nat. Geosci.* **2013**, *6* (5), 351–356. https://doi.org/10.1038/ngeo1779.

(144) Custard, K. D.; Raso, A. R. W.; Shepson, P. B.; Staebler, R. M.; Pratt, K. A. Production and Release of Molecular Bromine and Chlorine from the Arctic Coastal Snowpack. *ACS Earth Sp. Chem.* **2017**, *1* (3), 142–151. https://doi.org/10.1021/acsearthspacechem.7b00014.

(145) Halfacre, J. W.; Shepson, P. B.; Pratt, K. A. PH-Dependent Production of Molecular Chlorine, Bromine, and Iodine from Frozen Saline Surfaces. *Atmos. Chem. Phys.* **2019**, *19* (7), 4917–4931. https://doi.org/10.5194/acp-19-4917-2019.

(146) Simpson, W. R.; von Glasow, R.; Riedel, K.; Anderson, P.; Ariya, P.; Bottenheim, J.; Burrows, J.; Carpenter, L. J.; Frieß, U.; Goodsite, M. E.; Heard, D.; Hutterli, M.; Jacobi, H.-W.; Kaleschke, L.; Neff, B.; Plane, J.; Platt, U.; Richter, A.; Roscoe, H.; Sander, R.; Shepson, P.; Sodeau, J.; Steffen, A.; Wagner, T.; Wolff, E. Halogens and Their Role in Polar Boundary-Layer Ozone Depletion. *Atmos. Chem. Phys.* **2007**, *7* (16), 4375–4418. https://doi.org/10.5194/acp-7-4375-2007.

(147) Liu, Q.; Schurter, L. M.; Muller, C. E.; Aloisio, S.; Francisco, J. S.; Margerum, D. W. Kinetics and Mechanisms of Aqueous Ozone Reactions with Bromide, Sulfite, Hydrogen Sulfite, Iodide, and Nitrite Ions. *Inorg. Chem.* **2001**, *40* (17), 4436–4442. https://doi.org/10.1021/ic000919j.

(148) Mössinger, J. C.; Cox, R. A. Heterogeneous Reaction of HOI with Sodium Halide Salts. *J. Phys. Chem. A* **2001**, *105* (21), 5165–5177. https://doi.org/10.1021/jp0044678.

(149) Braban, C. F.; Adams, J. W.; Rodriguez, D.; Cox, R. A.; Crowley, J. N.; Schuster, G. Heterogeneous Reactions of HOI, ICl and IBr on Sea Salt and Sea Salt Proxies. *Phys. Chem. Chem. Phys.* **2007**, *9* (24), 3136–3148. https://doi.org/10.1039/b700829e.

(150) Carpenter, L. J.; MacDonald, S. M.; Shaw, M. D.; Kumar, R.; Saunders, R. W.; Parthipan, R.; Wilson, J.; Plane, J. M. C. Atmospheric Iodine Levels Influenced by Sea Surface Emissions of Inorganic Iodine. *Nat. Geosci.* **2013**, *6* (2), 108–111. https://doi.org/10.1038/ngeo1687.

(151) Jun, Y.; He, X.; Li, Q.; Cuevas, C. A.; Shen, J.; Kalliokoski, J.; Yan, C. Direct Field Evidence of Autocatalytic Iodine Release from Atmospheric Aerosol. *Proc. Natl. Acad. Sci.* **2021**, *118* (4), 1–8. https://doi.org/10.1073/pnas.2009951118.

(152) Horinek, D.; Herz, A.; Vrbka, L.; Sedlmeier, F.; Mamatkulov, S. I.; Netz, R. R. Specific Ion Adsorption at the Air/Water Interface: The Role of Hydrophobic Solvation. *Chem. Phys. Lett.* **2009**, *479* (4–6), 173–183. https://doi.org/10.1016/j.cplett.2009.07.077.

(153) Baer, M. D.; Mundy, C. J. Toward an Understanding of the Specific Ion Effect Using Density Functional Theory. *J. Phys. Chem. Lett.* **2011**, *2* (9), 1088–1093. https://doi.org/10.1021/jz200333b.

(154) Ghosal, S.; Hemminger, J. C.; Bluhm, H.; Mun, B. S.; Hebenstreit, E. L. D.; Ketteler, G.; Ogletree, D. F.; Requejo, F. G.; Salmeron, M. Electron Spectroscopy of Aqueous Solution

Interfaces Reveals Surface Enhancement of Halides. *Science (80-.).* **2005**, *307* (5709), 563–566. https://doi.org/10.1126/science.1106525.

(155) Ottosson, N.; Faubel, M.; Bradforth, S. E.; Jungwirth, P.; Winter, B. Photoelectron Spectroscopy of Liquid Water and Aqueous Solution: Electron Effective Attenuation Lengths and Emission-Angle Anisotropy. *J. Electron Spectros. Relat. Phenomena* **2010**, *177* (2–3), 60–70. https://doi.org/10.1016/j.elspec.2009.08.007.

(156) Olivieri, G.; Parry, K. M.; Powell, C. J.; Tobias, D. J.; Brown, M. A. Quantitative Interpretation of Molecular Dynamics Simulations for X-Ray Photoelectron Spectroscopy of Aqueous Solutions. *J. Chem. Phys.* **2016**, *144* (15), 154704. https://doi.org/10.1063/1.4947027.

(157) Olivieri, G.; Parry, K. M.; D'Auria, R.; Tobias, D. J.; Brown, M. A. Specific Anion Effects on Na+ Adsorption at the Aqueous Solution-Air Interface: MD Simulations, SESSA Calculations, and Photoelectron Spectroscopy Experiments. *J. Phys. Chem. B* **2018**, *122* (2), 910–918. https://doi.org/10.1021/acs.jpcb.7b06981.

(158) Sloutskin, E.; Baumert, J.; Ocko, B. M.; Kuzmenko, I.; Checco, A.; Tamam, L.; Ofer, E.; Gog, T.; Gang, O.; Deutsch, M. The Surface Structure of Concentrated Aqueous Salt Solutions. *J. Chem. Phys.* **2007**, *126* (5), 054704. https://doi.org/10.1063/1.2431361.

(159) Kenrick, F. B. Die Potentialsprünge Zwischen Gasen Und Flüssigkeiten. *Zeitschrift für Phys. Chemie* **1896**, *19* (1), 625–656. https://doi.org/10.1515/zpch-1896-1937.

(160) Borazio, A.; Farrell, J. R.; McTigue, P. Charge Distribution at the Gas-Water Interface the Surface Potential of Water. *J. Electroanal. Chem.* **1985**, *193* (1–2), 103–112. https://doi.org/10.1016/0022-0728(85)85055-5.

(161) Guyot, J. Effet Volta Métal-Électrolyte et Couches Monomoléculaires. *Ann. Phys. (Paris).* **1924**, *10* (2), 506–638. https://doi.org/10.1051/anphys/192410020506.

(162) Rosen, M. J.; Kunjappu, J. T. *Surfactants and Interfacial Phenomena: Fourth Edition*, 4th Editio.; Wiley: Hoboken, 2012. https://doi.org/10.1002/9781118228920.

(163) Casper, C. B.; Verreault, D.; Adams, E. M.; Hua, W.; Allen, H. C. Surface Potential of DPPC Monolayers on Concentrated Aqueous Salt Solutions. *J. Phys. Chem. B* **2016**, *120* (8), 2043–2052. https://doi.org/10.1021/acs.jpcb.5b10483.

(164) Pethica, B. A.; Few, A. V. The Surface Potentials of Long Chain Sulphates and Their Relation to Dispersion Stability. *Discuss. Faraday Soc.* **1954**, *18* (0), 258–267. https://doi.org/10.1039/DF9541800258.

(165) Phan, C. M. Ionization of Surfactants at the Air-Water Interface. In *Physical Chemistry of Gas-Liquid Interfaces*; Elsevier, 2018; pp 79–104. https://doi.org/10.1016/B978-0-12-813641-6.00004-2.

(166) Warszynski, P.; Barzyk, W.; Lunkenheimer, K.; Fruhner, H. Surface Tension and Surface Potential of Na Iz-Dodecyl Sulfate at the Air-Solution Interface: Model and Experiment. *J. Phys. Chem. B* **1998**, *102* (52), 10948–10957. https://doi.org/10.1021/jp983901r.

(167) Adamczyk, Z.; Para, G.; Warszyński, P. Influence of Ionic Strength on Surface Tension of Cetyltrimethylammonium Bromide. *Langmuir* **1999**, *15* (24), 8383–8387. https://doi.org/10.1021/la990241o.

(168) Persson, C. M.; Jonsson, A. P.; Bergström, M.; Eriksson, J. C. Testing the Gouy-Chapman Theory by Means of Surface Tension Measurements for SDS-NaCl-H 2 O Mixtures. *J. Colloid Interface Sci.* **2003**, *267*, 151–154. https://doi.org/10.1016/S0021-9797(03)00761-6.

(169) Martinez, I. S.; Baldelli, S. On the Arrangement of Ions in Imidazolium-Based Room Temperature Ionic Liquids at the Gas−Liquid Interface, Using Sum Frequency Generation, Surface Potential, and Surface Tension Measurements. *J. Phys. Chem. C* **2010**, *114* (26), 11564–11575. https://doi.org/10.1021/jp1039095.

(170) Menger, F. M.; Rizvi, S. A. A. Relationship between Surface Tension and Surface Coverage. *Langmuir* **2011**, *27* (23), 13975–13977. https://doi.org/10.1021/la203009m.

(171) Nihonyanagi, S.; Yamaguchi, S.; Tahara, T. Direct Evidence for Orientational Flip-Flop of Water Molecules at Charged Interfaces: A Heterodyne-Detected Vibrational Sum Frequency Generation Study. *J. Chem. Phys.* **2009**, *130* (20), 204704. https://doi.org/10.1063/1.3135147.

(172) Bastos-González, D.; Pérez-Fuentes, L.; Drummond, C.; Faraudo, J. Ions at Interfaces: The Central Role of Hydration and Hydrophobicity. **2016**. https://doi.org/10.1016/j.cocis.2016.05.010.

(173) Vrbka, L.; Mucha, M.; Minofar, B.; Jungwirth, P.; Brown, E. C.; Tobias, D. J. Propensity of Soft Ions for the Air/Water Interface. *Curr. Opin. Colloid Interface Sci.* **2004**, *9* (1–2), 67–73. https://doi.org/10.1016/j.cocis.2004.05.028.

(174) Weber, R.; Winter, B.; Schmidt, P. M.; Widdra, W.; Hertel, I. V.; Dittmar, M.; Faubel, M. Photoemission from Aqueous Alkali-Metal-Iodide Salt Solutions Using EUV Synchrotron Radiation. *J. Phys. Chem. B* **2004**, *108* (15), 4729–4736. https://doi.org/10.1021/jp030776x.

(175) Tian, C.; Byrnes, S. J.; Han, H. L.; Shen, Y. R. Surface Propensities of Atmospherically Relevant Ions in Salt Solutions Revealed by Phase-Sensitive Sum Frequency Vibrational Spectroscopy. *J. Phys. Chem. Lett.* **2011**, *2* (15), 1946–1949. https://doi.org/10.1021/jz200791c.

(176) Petersen, P. B.; Saykally, R. J. Adsorption of Ions to the Surface of Dilute Electrolyte Solutions: The Jones-Ray Effect Revisited. *J. Am. Chem. Soc.* **2005**. https://doi.org/10.1021/ja053224w.

(177) Otten, D. E.; Petersen, P. B.; Saykally, R. J. Observation of Nitrate Ions at the Air/Water Interface by UV-Second Harmonic Generation. *Chem. Phys. Lett.* **2007**, *449* (4–6), 261–265. https://doi.org/10.1016/j.cplett.2007.10.081.

(178) Otten, D. E.; Shaffer, P. R.; Geissler, P. L.; Saykally, R. J. Elucidating the Mechanism of Selective Ion Adsorption to the Liquid Water Surface. *Proc. Natl. Acad. Sci. U. S. A.* **2012**, *109* (3), 701–705. https://doi.org/10.1073/pnas.1116169109.

(179) Gschwend, G. C.; Olaya, A.; Peljo, P.; Girault, H. H. Structure and Reactivity of the Polarised Liquid–Liquid Interface: What We Know and What We Do Not. *Current Opinion in Electrochemistry*. Elsevier B.V. February 1, 2020, pp 137–143. https://doi.org/10.1016/j.coelec.2019.12.002.

(180) Jungwirth, P.; Winter, B. Ions at Aqueous Interfaces: From Water Surface to Hydrated

Proteins. *Annu. Rev. Phys. Chem.* **2008**, *59*, 343–366.
https://doi.org/10.1146/annurev.physchem.59.032607.093749.

(181) Liu, Y.; Sengupta, A.; Raghavachari, K.; Flood, A. H. Anion Binding in Solution: Beyond the Electrostatic Regime. *Chem* **2017**, *3* (3), 411–427.
https://doi.org/10.1016/j.chempr.2017.08.003.

(182) Milo, A.; Neel, A. J.; Toste, F. D.; Sigman, M. S. A Data-Intensive Approach to Mechanistic Elucidation Applied to Chiral Anion Catalysis. *Science (80-.).* **2015**, *347* (6223), 737–743. https://doi.org/10.1126/science.1261043.

(183) Case, B.; Parsons, R. The Real Free Energies of Solvation of Ions in Some Non-Aqueous and Mixed Solvents. *Trans. Faraday Soc.* **1967**, *63* (0), 1224.
https://doi.org/10.1039/tf9676301224.

(184) Case, B.; Hush, N. S.; Parsons, R.; Peover, M. E. The Real Solvation Energies of Hydrocarbon Ions in Acetonitrile and the Surface Potential of Acetonitrile. *J. Electroanal. Chem.* **1965**, *10* (5–6), 360–370. https://doi.org/10.1016/0022-0728(65)80038-9.

(185) Parsons, R.; Rubin, B. T. The Medium Effect for Single Ionic Species. *J. Chem. Soc. Faraday Trans. 1 Phys. Chem. Condens. Phases* **1974**, *70* (0), 1636–1648.
https://doi.org/10.1039/F19747001636.

(186) Trasatti, S. Interfacial Behaviour of Non-Aqueous Solvents. *Electrochim. Acta* **1987**, *32* (6), 843–850. https://doi.org/10.1016/0013-4686(87)87072-X.

(187) Barraclough, C. G.; McTigue, P. T.; Ng, Y. L. Surface Potentials of Water, Methanol and Water + Methanol Mixtures. *J. Electroanal. Chem.* **1992**, *329* (1–2), 9–24.
https://doi.org/10.1016/0022-0728(92)80205-I.

(188) Leung, K. Surface Potential at the Air-Water Interface Computed Using Density Functional Theory. *J. Phys. Chem. Lett* **2010**, *1*, 496–499.
https://doi.org/10.1021/jz900268s.

(189) Dang, L. X.; Chang, T. M. Molecular Mechanism of Ion Binding to the Liquid/Vapor Interface of Water. *J. Phys. Chem. B* **2002**, *106* (2), 235–238.
https://doi.org/10.1021/jp011853w.

(190) Passoth, G. Über Die Hydratationsenergien Und Die Scheinbaren Molvolumen Einwertiger Ionen. *Zeitschrift für Phys. Chemie* **1954**, *2030* (1), 275–291.
https://doi.org/10.1515/zpch-1954-20320.

(191) Fawcett, W. R. The Ionic Work Function and Its Role in Estimating Absolute Electrode Potentials. *Langmuir* **2008**, *24* (17), 9868–9875. https://doi.org/10.1021/la7038976.

(192) Hush, N. S. The Free Energies of Hydration of Gaseous Ions. *Aust. J. Chem.* **1948**, *1* (4), 480–494. https://doi.org/10.1071/CH9480480.

(193) Strehlow, H. Zum Problem Des Einzelelektronpotentials. *Zeitschrift für Elektrochemie, Berichte der Bunsengesellschaft für Phys. Chemie* **1952**, *56* (2), 119–129.
https://doi.org/10.1002/BBPC.19520560207.

(194) Chalmers, J. A.; Pasquill, F. VII. The Potential Difference at an Air-Water Interface. *London, Edinburgh, Dublin Philos. Mag. J. Sci. Ser. 7* **1937**, *23* (152), 88–96.
https://doi.org/10.1080/14786443708561776.

(195) Randles, J. E. B.; Whiteley, K. S. The Temperature Dependence of the Electrocapillary Maximum of Mercury. *Trans. Faraday Soc.* **1956**, *52* (0), 1509–1512. https://doi.org/10.1039/tf9565201509.

(196) Kochurova, N. N.; Rusanov, A. I. Dynamic Surface Properties of Water: Surface Tension and Surface Potential. *J. Colloid Interface Sci.* **1981**, *81* (2), 297–303. https://doi.org/10.1016/0021-9797(81)90411-2.

(197) Gomer, R.; Tryson, G. An Experimental Determination of Absolute Half-Cell Emf's and Single Ion Free Energies of Solvation. *J. Chem. Phys.* **1977**, *66* (10), 4413–4424. https://doi.org/10.1063/1.433746.

(198) Frumkin, A. N.; Iofa, Z. A.; Gerovich, M. A. The Potential Difference at the Boundary Water-Gas. *Zh. fiz. khim.* **1956**, No. 30, 1455–1468.

(199) Frumkin, A. N. Note on B. Kamieński's Paper 'The Nature of the Electric Potential at the Free Surface of Aqueous Solutions'. *Electrochim. Acta* **1960**, *2* (4), 351–354. https://doi.org/10.1016/0013-4686(60)80031-X.

(200) Cendagorta, J. R.; Ichiye, T. The Surface Potential of the Water-Vapor Interface from Classical Simulations. *J. Phys. Chem. B* **2015**, *119* (29), 9114–9122. https://doi.org/10.1021/jp508878v.

(201) Hofer, T. S.; Hünenberger, P. H. Absolute Proton Hydration Free Energy, Surface Potential of Water, and Redox Potential of the Hydrogen Electrode from First Principles: QM/MM MD Free-Energy Simulations of Sodium and Potassium Hydration. *Journal of Chemical Physics*. American Institute of Physics Inc. June 14, 2018, p 222814. https://doi.org/10.1063/1.5000799.

(202) Pezzotti, S.; Galimberti, D. R.; Shen, Y. R.; Gaigeot, M. P. Structural Definition of the BIL and DL: A New Universal Methodology to Rationalize Non-Linear: χ (2)(ω) SFG Signals at Charged Interfaces, Including χ (3)(ω) Contributions. *Phys. Chem. Chem. Phys.* **2018**, *20* (7), 5190–5199. https://doi.org/10.1039/c7cp06110b.

(203) Helmholtz, H. Ueber Einige Gesetze Der Vertheilung Elektrischer Ströme in Körperlichen Leitern Mit Anwendung Auf Die Thierisch-elektrischen Versuche. *Ann. Phys.* **1853**, *165* (6), 211–233. https://doi.org/10.1002/andp.18531650603.

(204) Reichardt, C.; Welton, T. *Solvents and Solvent Effects in Organic Chemistry: Fourth Edition*; Wiley-VCH, 2010. https://doi.org/10.1002/9783527632220.

(205) Buch, V.; Milet, A.; Vácha, R.; Jungwirth, P.; Devlin, J. P. Water Surface Is Acidic. *Proc. Natl. Acad. Sci. U. S. A.* **2007**, *104* (18), 7342–7347. https://doi.org/10.1073/pnas.0611285104.

(206) Winter, B.; Faubel, M.; Vácha, R.; Jungwirth, P. Behavior of Hydroxide at the Water/Vapor Interface. *Chem. Phys. Lett.* **2009**, *474*, 241–247. https://doi.org/10.1016/j.cplett.2009.04.053.

(207) Enami, S.; Hoffmann, M. R.; Colussi, A. J. Halogen Radical Chemistry at Aqueous Interfaces. *J. Phys. Chem. A* **2016**, *120* (31), 6242–6248. https://doi.org/10.1021/acs.jpca.6b04219.

(208) Petersen, P. B.; Saykally, R. J. Evidence for an Enhanced Hydronium Concentration at the

Liquid Water Surface. *J. Phys. Chem. B* **2005**, *109* (16), 7976–7980. https://doi.org/10.1021/jp044479j.

(209) Yesibolati, M. N.; Laganà, S.; Sun, H.; Beleggia, M.; Kathmann, S. M.; Kasama, T.; Mølhave, K. Mean Inner Potential of Liquid Water. *Phys. Rev. Lett.* **2020**, *124* (6), 065502. https://doi.org/10.1103/PhysRevLett.124.065502.

(210) Knoll, G. F. *Radiation Detection and Measurement*, 4th. Editi.; John Wiley & Sons: New York, 2010.

(211) Kavetskiy, A.; Yakubova, G.; Prior, S. A.; Torbert, H. A. Application of Associated Particle Neutron Techniques for Soil Carbon Analysis. In *AIP Conference Proceedings 2160*; 2019; Vol. 050006. https://doi.org/10.1063/1.5127698.

Appendix A. Mapping Potential of Ionization from Am-241

For any narrow beam of radiation, the radioactive particles will decrease in intensity as it passes through a substance. With the ionizing surface potential method, the alpha particles will decrease in intensity as it passes through the air gap above the solution. A very good approximation of the intensity of alpha particle passing through the air slab at a distance L from the source, is described by Lambert's law:

$$E_L = E_0 e^{-\tau L} \tag{Eq. A-1}$$

where E_L is the attenuated energy of alpha particle, E_0 initial mean energy of alpha particle, and τ is the mass attenuation coefficient for alpha particles in air[210] as shown in Figure A-1(a.).

In addition to the attenuation of radioactively decaying alpha particle beam, the effective area of the attenuated beam overlapping the solution surface, will depend on the Lorentzian shape of the beam diameter and the diameter of the radioactive electrode.[210,211] Therefore, we use the Lorentzian Ł as a function of electrode diameter, r:

$$Ł(r) = E_0 \frac{1}{\pi} \frac{\frac{1}{2}L_0}{(2r - 2r_0)^2 + \left(\frac{1}{2}L_0\right)^2} \tag{Eq. A-2}$$

where E_0 = 5.6 MeV, L_0 = 0.5 mm, and r_0 is the geometric center of the Am-241 radioactive electrode (5 mm) utilized in this study. The results of the profile are plotted in Figure A-1(b.).

With this value of intensity and replacing in the Lorentzian profile, the effective

attenuated area is calculated by the determination of the effective distance at the surface position,

as described in:

$$\alpha = \frac{\text{area of beam near air-water surface}}{\text{area of beam near Am-241 electrode}} = \frac{\pi\left(\frac{1}{2}\Delta(2r)\right)^2}{\pi\left(\frac{1}{2}L_0\right)^2} = 4.0E\text{-}6 \qquad \text{(Eq. A-3)}$$

After performing the calculations, the α obtained for the effective area was 4E-06 times

the value of the active area of the Am-241 electrode. This α value is used in equations (3.1) and

(3.3) of this work. Lorentzian fitting (Appendix C) was done using scripts written in Python 3.8.5

through Spyder IDE (version 4.0.1) with the *SciPy* package (version 1.5.2) for nonlinear least-

squares fitting (Levenberg-Marquardt).[122]

(a.)

$E_0 = 5.6$ MeV where $L = 0.5$ mm

$$E_L = E_0 e^{-\tau L}$$

$E_L = 1.3\text{E-}03$ MeV where $L = 7.2$ mm

(b.)

effective diameter of alpha particle beam at the air-aqueous surface

$r = 7.2$ mm

projected area where $\Delta L \approx 7\text{E-}03$m (top-down view)

$\Delta(2r) = +/- 1.0\text{E-}06$ m
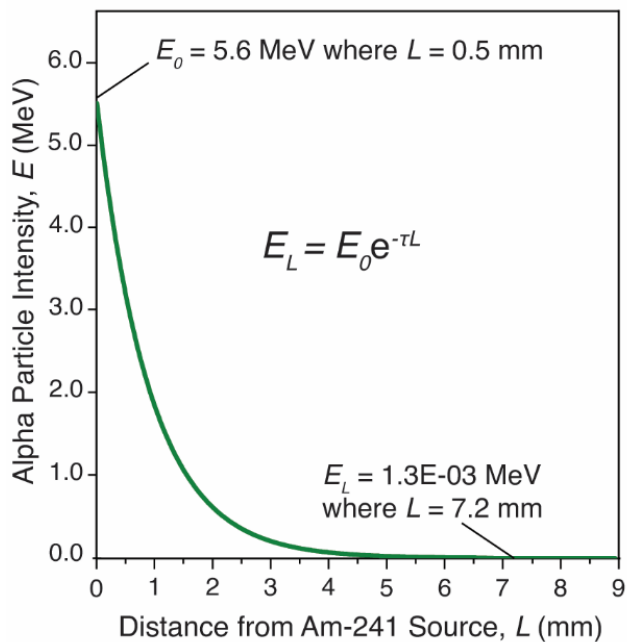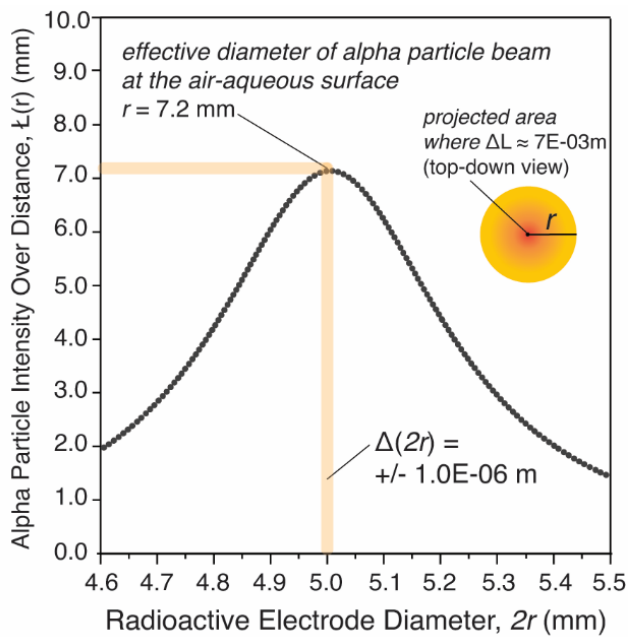
Figure A-1. (a.) Intensity over distance profile for the 5 MeV Am-241 source. (b.) Lorentzian profile for the alpha particles beam of the Am-241 electrode.

115

Appendix B. Laplace Transformation of Real-time Potential Data

In order to solve complex differential functions, the Laplace transform is an integral transform used to convert a function of a real variable, in this study to convert current $i_1(t)$, to a function of a complex variable, $i_1(s)$. This allows us to transform the complex differential form of equation (9) into an algebraic system of equations (Eq. B-1) to (Eq. B-5). Following this transform, Cramer's rule is also applied, such that:

$$\mathcal{L}\{(1), (2), (3)\} \Rightarrow \qquad \text{(Eq. B-1)}$$

$$i_1(s) - i_2(s) - i_3(s) = 0 \qquad \text{(Eq. B-2)}$$

$$\frac{i_3(s)}{sC_S} - i_2(s)R_S = 0 \qquad \text{(Eq. B-3)}$$

$$\frac{i_1(s)}{sC_a} + \frac{i_3(s)}{sC_S} + \frac{i_1(s)}{sC_b} + i_1(s)\,R_{Pt} = \frac{\Omega}{s+\lambda} \qquad \text{(Eq. B-4)}$$

$$i_1(s) = \frac{\begin{vmatrix} 0 & -1 & -1 \\ 0 & -R_S & \frac{1}{sC_S} \\ \frac{\Omega}{s+\lambda} & 0 & \frac{1}{sC_S} \end{vmatrix}}{\begin{vmatrix} 1 & -1 & -1 \\ 0 & -R_S & \frac{1}{sC_S} \\ \frac{1}{sC_a}+\frac{1}{sC_b}+R_{Pt} & 0 & \frac{1}{sC_S} \end{vmatrix}} \qquad \text{(Eq. B-5)}$$

By solving the determinants in (Eq. B-5), we have the following:

$$i_1(s) = \frac{\Omega}{(s+\lambda)} \frac{s\,(R_s+1)\,C_a C_b}{[s^2(R_{Pt}R_s C_a C_s C_b)+ s(R_s C_s C_b + R_s C_s C_a - R_{Pt}C_a C_b) -(C_a+C_b)]} \quad \text{(Eq. B-6)}$$

$$r_{1,2} = \frac{R_{Pt}C_a C_b - R_s C_s C_b - R_s C_s C_a \pm \sqrt{(R_s C_s C_b + R_s C_s C_a - R_{Pt}C_a C_b)^2 + 4\,(R_{Pt}R_s C_a C_s C_b)(C_a+C_b)}}{2(R_{Pt}R_s C_a C_s C_b)} \quad \text{(Eq. B-7)}$$

This leads us to the following linear system,

$$i_1(s) = \frac{\Omega}{(s+\lambda)} \frac{s(R_s+1)C_a C_b}{(s-r_1)(s-r_2)} \quad \text{(Eq. B-8)}$$

From (Eq. B-8), the variables are now redefined in terms of the partial fractions β, ζ, and η such that,

$$i_1(s) = \frac{\beta}{s+\lambda} + \frac{\zeta}{s-r_1} + \frac{\eta}{s-r_2} \quad \text{(Eq. B-9)}$$

$$\beta + \zeta + \eta = 0 \quad \text{(Eq. B-10)}$$

$$-\beta(r_2 + r_1) + \zeta(\lambda - r_2) + \eta(\lambda - r_1) = -\Omega(R_s + 1)C_a C_b \quad \text{(Eq. B-11)}$$

$$\beta(r_1 r_2) + \zeta(\lambda r_2) + \eta(\lambda r_1) = 0 \quad \text{(Eq. B-12)}$$

which gives the following partial fractions:

$$\chi = \frac{\Omega(R_s+1)C_a C_b(\lambda r_1 - \lambda r_2 r_1^2 - \lambda r_2 + \lambda r_1 r_2^2)}{(r_1+\lambda)(\lambda r_1 - \lambda r_2 r_1^2) - (\lambda r_2 - \lambda r_1 r_2^2)(r_2+\lambda)} \quad \text{(Eq. B-13)}$$

$$\zeta = -\frac{\Omega(R_s+1)C_aC_b(\lambda r_1 - \lambda r_2 r_1^2)}{(r_1+\lambda)(\lambda r_1 - \lambda r_2 r_1^2) - (\lambda r_2 - \lambda r_1 r_2^2)(r_2+\lambda)} \qquad \text{(Eq. B-14)}$$

$$\beta = \frac{\Omega(R_s+1)C_aC_b(\lambda r_2 - \lambda r_1 r_2^2)}{(r_1+\lambda)(\lambda r_1 - \lambda r_2 r_1^2) - (\lambda r_2 - \lambda r_1 r_2^2)(r_2+\lambda)} \qquad \text{(Eq. B-15)}$$

Finally, applying the inverse Laplace transform to (Eq. B-9), $i_1(t)$ is defined as,

$$i_1(t) = \mathcal{L}^{-1}\{\frac{\beta}{s+\lambda} + \frac{\zeta}{s-r_1} + \frac{\eta}{s-r_2}\} \qquad \text{(Eq. B-16)}$$

$$i_1(t) = \beta e^{-\lambda t} - \zeta e^{r_1 t} + \eta e^{r_2 t} \qquad \text{(Eq. B-17)}$$

Taking equation (B-17) with a non-linear regression analysis as summarized in Figure B-1, the unknown variables β, ζ, η can be determined (Table B-1) from the fit, which is used to determine the value of $i_1(t)$ (Table 3-3) for each respective salt electrolyte.

Table B-1. Results of non-linear regression analysis on extracted model parameters for 1.0 M NaCl and 1.0 M Na$_2$SO4 solutions from equation (B-17).

		β	ζ	η
1.0 M NaCl	*Fit*	0.35	0.08	-0.38
	Std. dev.	2.0E-03	6.0E-04	3.0E-04
1.0 M Na$_2$SO4	*Fit*	0.39	0.10	-0.45
	Std. dev.	2.4E-03	9.9E-04	3.6E-04
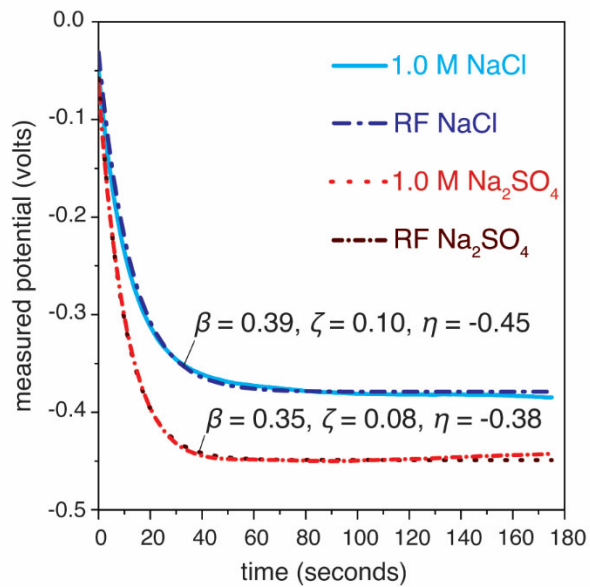
Figure B-1. Using equation (B-17), a non-linear regression of measured potential (volts) vs. time (seconds) is calculated to extract model parameters for (a) 1.0 M NaCl (solid —) with plotted regression (dash dot -.-.) and (b) 1.0 M Na₂SO₄ (dotted …) with plotted regression (dash dot dash -.-).

119

Appendix C. Python Codes for Various Fittings

Codes are color-marked to distinguish convenience. Note that lines marked by "#" do not indicate actual code but a description of the following codes.

C.1 Lorentzian analysis of Am-241 alpha particle ionization

```python
#Step-1. Important Python packages used for the fitting regression analysis
import matplotlib
import numpy as np
import matplotlib.pyplot as plt
import operator
from matplotlib.collections import LineCollection
import matplotlib.pyplot as plt
import pandas as pd
from scipy import integrate
from matplotlib import rcParams

#Step-2. Defining terms as outlined in Appendix A
time = 80
x = np.linspace(4.5, 5.5, 1000
              )
A = np.pi*np.power(0.5e-3/2,2)
Io = 5.6
Alpha = 1.1691 #Mass attenuation coefficient cm-1
D = 0.5 #Effective diamater Am
L = 5.7*(1.0/np.pi)*(0.5*D)/(np.power((x-5),2)+np.power(0.5*D,2))
z = np.linspace(0,9,1000)
I = Io*np.exp(-Alpha*z)

#Step-3. Plot of the Lorentzian profile of the Am-241 radiation with distance to the solution surface
(7 mm away)
fig, ax = plt.subplots()
xy=(7., Io*np.exp(-Alpha*7.0))
bbox = dict(boxstyle ="round", fc ="0.8")
ax.annotate('(%s, %.4f)' % xy,
            xy=(7., Io*np.exp(-Alpha*7)), xycoords='data',
            xytext=(-50, 30), textcoords='offset points', bbox= bbox,
            arrowprops=dict(arrowstyle="->",facecolor = 'green'))

ax.plot(z, I)
ax.set(xlabel='Diameter (mm)', ylabel='Intensity',
       title='Energy Distribution for Am Electrode')
plt.text(2.1, 3.5, r'$I = I_{0} e^{-\mu z} $',fontsize=15,bbox=dict(facecolor='yellow', alpha=0.2))
plt.text(2.1, 4.5, r'$\mu = 1.17$   $I_{0} = 5.5 MeV$',fontsize=12,bbox=dict(facecolor='yellow',
alpha=0.2))
ax.grid()
index, value = max(enumerate(L), key=operator.itemgetter(1))
print(str(index)+' '+str(value))
crit = Io*np.exp(-Alpha*7.0)
value = value-crit*value
xl = []
xj = []
conta = 1
for i,j in zip(x,L):
    if j >= value and j<= (value+0.005*value):
        xl.append(i)
        xj.append(j)
```

```python
                                    # <--
distance = xl[1]-xl[0]
xy=(xl[0],xj[0])
bbox = dict(boxstyle ="round", fc ="0.8")
arrowprops = dict(
    arrowstyle = "->",
    connectionstyle = "angle, angleA = 0, angleB = 90,rad = 10")

fig, axs = plt.subplots()
axs.annotate('(%.4f, %.4f)' % xy,
             xy=(xl[0],xj[0]), xycoords='data',
             xytext=(-41.5, -40), textcoords='offset points', bbox = bbox,
             arrowprops=arrowprops)

axs.annotate('Intersection with Surface' ,
             xy=(xl[0],xj[0]), xycoords='data',
             xytext=(-58, -115), textcoords='offset points', bbox = bbox)

l1 = [(xl[0], xj[0]), (xl[1], xj[1])]
lc = LineCollection([l1], color=["k","red"], lw=4)


axs.plot(x, L)
axs.set(xlabel='Effective Diameter Am (mm)', ylabel='Intensity Over Distance (mm)',
        title='Spatial Energy Distribution for Am Electrode')
axs.grid()
fig.suptitle('Attenuation Estimation')
plt.gca().add_collection(lc)


fig.savefig("test.png")
plt.show()

dataf = np.concatenate((z,I))
df = pd.DataFrame(data=dataf)
df.to_csv (r'export_dataframeEnergyDist.csv', index = False, header=True)

dataf1 = np.concatenate((x,L))
df = pd.DataFrame(data=dataf1)
df.to_csv (r'export_dataframeAttenuationEstimate.csv', index = False, header=True)
```

C.2 Calculation of the Interfacial Surface Potential (NaCl)

```python
#Step-1. Important Python packages used for the fitting regression analysis
import scipy.special as special
import csv
import numpy as np
import matplotlib.pyplot as plt
from scipy import integrate
import pandas as pd
from matplotlib import rcParams
rcParams['figure.figsize'] = (10, 6)
rcParams['legend.fontsize'] = 16
rcParams['axes.labelsize'] = 16


#Step-2. Experimental terms specific to 1.0 M NaCl
elecC = 1 #Concentration of electrolyte M
areaAi=np.pi*np.power((0.5e-3)/2,2)*0.00000279999999499#5.4Mev at 7mm attenuation factor
http://www.pef.uni-lj.si/eprolab/comlab/sttop/sttop-is/TG/Radiation/Alpha.htm
#0.00140092408
Con=1 # concentration of KI
mu = 1.256637062e-6 #magnetic permeability of vacuum
c = 299792458 #Speed of light m/s
e0=1/(mu*np.power(float(c),2)) #permitivitty of Vacuum
er=80.2 #Relative permitivitty of water
kb=1.38064852e-23 #Boltzmann constant m2 kg s-2 K-1
T=21.9+273.15 #Temperature
Na=6.022140857e23# Avogadro
ele=1.602176634e-19 #Fundamental Charge C
I=1# Ionic strenght KI
```

121

```
debyeL=np.power((er*e0*kb*T)/(2e3*Na*np.power(ele,2)*I),0.5)#Debye Length
Ci=(er*e0*(np.power((75e-3)/2,2)*np.pi))/debyeL
cho = 143.32e-4 #m2S mol-1
https://sites.chem.colostate.edu/diverdi/all_courses/CRC%20reference%20data/equivalent%20conductivity%
20of%20electrolytes.pdf
conduc = 83.3e-3*100
#conduc = 10.9e-3*100 #s/m
#conduc = 148.9e-6*100
#cho*elecC/0.01 # Conductivity S/m
Rint=(1/conduc)*debyeL/areaAi
Ca = (e0*(np.power(12.9e-3/2,2)*np.pi))/7e-3
Re=((105e-9)*(25e-3+35e-2)/(25e-3*35e-3))+((105e-9)*(25e-3+35e-2)/(np.pi*np.power(0.5e-3/2,2)))
A=0.322
a=0.078
#ri=3.06e-4
#re=8.11e-3
re=Re
Cb=(er*e0*(25e-3*35e-3))/7.8e-3
#ca=2.49e-14
ca=Ca
#ci=1.85e-6
cb=Cb
#cb=2.44e-10
#rint=180000*0.8e-9/(np.power(0.5e-3/2,2)*np.pi)
#cint=18e-6*(np.power(1.27e-3/2,2)*np.pi)*100*100*100
```

#Step 3 – Calculation of parameters used for calculation of fitting paramaters
```
ci=Ci
ri=Rint
#r1=1.77e9
#r2=-4.96e9
r1=(re*ca*cb-ri*ci*cb-ri*ci*ca+np.power(np.power((ri*ci*cb+ri*ci*ca-
re*ca*cb),2)+4*re*ri*ca*ci*cb*(ca+cb),0.5))/(2*re*ri*ca*ci*cb)
r2=(re*ca*cb-ri*ci*cb-ri*ci*ca-np.power(np.power((ri*ci*cb+ri*ci*ca-
re*ca*cb),2)+4*re*ri*ca*ci*cb*(ca+cb),0.5))/(2*re*ri*ca*ci*cb)
beta=(A*(ri+1)*ca*cb*(r2*a-r1*r1*r2*a))/((r1+a)*(a*r1-r2*a*r1*r1)-(r2*a-r1*r2*r2*a)*(r2+a))
chi =(A*(ri+1)*ca*cb*(r2*a-r1*r1*r2*a-r2*a+r1*r2*r2*a))/((r1+a)*(a*r1-r2*a*r1*r1)-(r2*a-
r1*r2*r2*a)*(r2+a))
```

**#Step 4 – Blue highlighted regions are user specific that follows input of voltage-time data, where x
= time, V = voltage**
```
t_min = 70
t_max = 80
t = np.linspace(t_min, t_max, 100)

x=[]
V=[]
with open('new-circNaCl_Vst.csv') as csv_file:
    csv_reader = csv.reader(csv_file, delimiter=',')
    next(csv_reader)
    for row in csv_reader:
        x.append(float(row[0]))
        V.append(float((row[1]))
x = np.array(x,dtype=float)
V = np.array(V,dtype=float)
V_avg = integrate.simps(V,x,axis=-1)/100
i=-beta*np.exp(r1*t)-chi*np.exp(-a*t)
i_avg = -integrate.simps(i,t)/176

gamma = i_avg*V_avg/(np.pi*np.power((75e-3)/2,2))
```

#Step 4 – This is optional. Use if a graphical plot is required.
```
plt.plot(t, i, 'og', label='data')
plt.grid(True)
plt.text(70, 50.7, r'I_average =
'+str(round(1000*i_avg,2))+'mA',fontsize=12,bbox=dict(facecolor='green', alpha=0.2))
plt.text(70, 30.2, r'V_average =  '+str(round(V_avg,4))+'V',fontsize=12,bbox=dict(facecolor='green',
alpha=0.2))
plt.text(70, 10.45, r'$\gamma =  $'+str(round(gamma,4))+'$
mJ/m^2$',fontsize=12,bbox=dict(facecolor='green', alpha=0.2))

plt.xlabel('$t(s)$')
plt.ylabel('$Current (mA)$')
plt.title('I Vs Time')
```

```python
plt.legend();

#Step 4 – Use if a graphical plot is required. To export data into a .CSV file.
dataf = np.concatenate((t,i))
df = pd.DataFrame(data=dataf)
df.to_csv (r'export_dataframeNaCl_Aug32020.csv', index = False, header=True)


#Step 5 - calculated values for the interfacial current (i_avg), the surface energy (gamma), the
integrated potential over time
print(V_avg)
print(i_avg)
print(gamma)
```

C.3 Fitting regression analysis of Frumkin-Fowler-Guggenheim

```python
#Step-1. Important Python packages used for the fitting regression analysis
import matplotlib.pyplot as plt
from scipy.optimize import curve_fit
import numpy as np
import scipy as sp
from matplotlib import rc
from scipy.optimize import leastsq
from scipy import stats
import pandas as pd
import matplotlib.cm as cm

#Step-2. Important Python The blue highlight region indicates data input by the user for C
(concentration), V (normalized values of measured surface potential), V_err (standard deviation of the
measured surface potentials)
C = np.array([0.2869,0.4587,0.6305,0.8023,0.9741,1.4036,1.8331,2.2626,2.6921],dtype=float)
#concentration in row[0] of FFG file, x
V = np.array([0.178,0.270,0.346,0.400,0.450,0.475,0.520,0.570,0.622],dtype=float) #potential in row[1]
of FFG file, y
V_err = np.array([0.05,0.04,0.04,0.03,0.03,0.02,0.03,0.03,0.04],dtype=float)

#Step-3. The function of for the Frumkin-Fowler-Guggenheim is outlined one the first line below
(equation 4.3).
def func(V, g, K):
    return (V/(1-V)) * np.exp(-g*V) * (55.5/K)
plt.plot(V, C, 'b.', label='NaI measured potential') #plt.plot(xdata, ydata, 'b-', label='data')
plt.axis([0, 2, 0, 3.5])
plt.grid(True)
plt.text(0.35, 2.0, r'$\frac{\theta}{1-\theta}*e^{-g \theta}=\frac{K}{55.5}C
$',fontsize=12,bbox=dict(facecolor='green', alpha=0.2))


#Step-4. Regressional analysis used for the Frumkin-Fowler-Guggenheim can be plotted as follows
popt, pcov = curve_fit(func, V, C)
plt.plot(V, func(V, *popt), 'r-',label='fit: g=%5.3f, K=%5.3f' % tuple(popt)) #plt.plot(xdata,
func(xdata, *popt), 'r-',label='fit: a=%5.3f, b=%5.3f, c=%5.3f' % tuple(popt))

#Step-5. The calculated values for the regression analysis used above
print(popt)
print(pcov)
print(perr)

#Step-6. This is optional, but if a printable plot is desired, the following codes can also be added
to add features to the plot
plt.errorbar(V,C, xerr=V_err, ls ='none')
plt.xlabel(r'$\theta$')
plt.ylabel('Concentration (Mol/L)')
plt.title(r'Non-Linear Regression Concentration vs'+r' $\theta$')
plt.legend()
plt.savefig('ThisIsNaClDoneRight.png')
plt.show()
perr = np.sqrt(np.diag(pcov))

#Step-7. This is also optional. To export data into a .CSV file
dataf = np.concatenate((V,C))
df = pd.DataFrame(data=dataf)
df.to_csv (r'export_dataframe_FFG.csv', index = False, header=True)
```

Appendix D. Calculation of the Estimated Dipolar Surface Potential (V_D)

To assess the dipolar contribution to the surface electric potential of various solvents, we proposed a simple model to estimate the *dipolar surface potential V_D*. As discussed in Section 5.3, the calculation of V_D (equation 5.2) uses the relative permittivity ε_s (dielectric constant) and dipole moment μ for over 300 solvents (taken from the CRC Handbook[6]). Data summarizing the V_D for over 300 solvents are presented in two tables below. The first table consists of dipole moments of organic solvents that were measured in the gas phase (open circles in Figure 5.2). Dipole moment data summarized in the second table were measured in the liquid phase (open triangles in Figure 5.2). The calculation of the surface area per molecules A is,

$$A = \pi \left(\frac{3}{4\pi} \frac{M}{\rho N_A} \right)^{2/3} \tag{D-1}$$

D.1 Selected solvents with dipole moments of molecules (gas phase)

Dipole moments of organic solvents in rows 136-169 have some error associated with the measurement of the dipole.

Table D-1. Solvents with dipole moments of molecules (gas phase)

	Solvent	M	ρ	ε_s	μ	$A\,(\times 10^{-19})$	V_D
		g/mol	g/cm³		D	m²/molecule	volts
1	Acetaldehyde	44.1	0.78	21.02	2.8	2.49	0.198
2	Acetic acid	60.1	1.05	6.20	1.7	2.52	0.411
3	Acetone	58.1	0.79	21.01	2.9	2.97	0.174
4	Acetonitrile	41.1	0.78	36.64	3.9	2.38	0.170
5	Acetophenone	120.1	1.03	17.44	3.0	4.05	0.161
6	Acetyl chloride	78.5	1.11	15.82	2.7	2.91	0.223
7	Acrylonitrile	53.1	0.80	33.02	3.9	2.78	0.161
8	Allyl alcohol gauche	58.1	0.85	19.72	1.6	2.82	0.108
9	Aniline	93.1	1.03	7.06	1.1	3.43	0.176
10	Anisole	108.1	0.99	4.30	1.4	3.86	0.313
11	Benzonitrile	103.1	1.01	25.92	4.5	3.71	0.177
12	Benzyl alcohol	108.1	1.04	11.92	1.7	3.74	0.144
13	Bromobenzene	157.0	1.50	5.45	1.7	3.77	0.311
14	1-Bromobutane	137.0	1.28	7.32	2.3	3.83	0.311
15	2-Bromobutane, (±)-	137.0	1.26	8.64	2.2	3.87	0.251
16	Bromoethane	109.0	1.46	9.01	2.0	3.00	0.284
17	1-Bromopropane	123.0	1.35	8.09	2.2	3.43	0.296
18	2-Bromopropane	123.0	1.31	9.46	2.2	3.49	0.252
19	Butanal	72.1	0.80	13.45	2.7	3.40	0.224
20	Butanenitrile gauche	69.1	0.79	24.83	3.9	3.33	0.178
21	Butanenitrile anti	69.1	0.79	24.83	3.7	3.33	0.170
22	1-Butanol	74.1	0.81	17.84	1.7	3.43	0.102

Table D-1 continued

Table D-1 continued

23	2-Butanone	72.1	0.80	18.56	2.8	3.41	0.165
24	γ-Butyrolactone	86.1	1.13	39.02	4.3	3.05	0.135
25	Chlorobenzene	112.6	1.11	5.69	1.7	3.70	0.303
26	1-Chlorobutane	92.6	0.89	7.28	2.1	3.76	0.282
27	2-Chlorobutane	92.6	0.87	8.56	2.0	3.80	0.236
28	Chlorocyclohexane (equitorial)	118.6	1.00	7.95	2.4	4.09	0.283
29	Chlorocyclohexane (axial)	118.6	1.00	7.95	1.9	4.09	0.221
30	Chloroethane	64.5	0.92	9.45	2.1	2.87	0.284
31	2-Chloroethanol	80.5	1.20	25.80	1.8	2.80	0.093
32	1-Chloro-2-methylpropane	92.6	0.88	7.03	2.0	3.79	0.283
33	2-Chloro-2-methylpropane	92.6	0.84	9.66	2.1	3.89	0.213
34	1-Chloronaphthalene	162.6	1.19	5.04	1.6	4.50	0.260
35	1-Chloropentane	106.6	0.88	6.65	2.2	4.14	0.295
36	1-Chloropropane gauche	78.5	0.89	8.59	2.1	3.36	0.268
37	1-Chloropropane trans	78.5	0.89	8.59	2.0	3.36	0.255
38	2-Chloropropene	76.5	0.90	8.92	1.6	3.27	0.212
39	3-Chloropropene	76.5	0.94	8.22	1.9	3.19	0.279
40	2-Chlorotoluene	126.6	1.08	4.72	1.6	4.05	0.307
41	4-Chlorotoluene	126.6	1.07	6.25	2.2	4.09	0.326
42	Cyclohexanone	98.1	0.95	16.12	3.2	3.74	0.203
43	Cyclohexene half chair	82.1	0.81	2.22	0.3	3.68	0.153
44	Dibromomethane	173.8	2.50	7.77	1.4	2.87	0.242
45	Dibutyl ether	130.2	0.77	3.08	1.2	5.19	0.275
46	o-Dichlorobenzene	147.0	1.31	10.12	2.5	3.95	0.235
47	m-Dichlorobenzene	147.0	1.29	5.02	1.7	3.99	0.324
48	1,1-Dichloroethane	99.0	1.18	10.10	2.1	3.26	0.236
49	1,1-Dichloroethene	96.9	1.21	4.60	1.3	3.15	0.349
50	cis-1,2-Dichloroethene	96.9	1.28	9.20	1.9	3.03	0.257
51	Dichloromethane	84.9	1.32	8.93	1.6	2.72	0.248

Table D-1 continued

Table D-1 continued

52	1,3-Dichloropropane	113.0	1.18	10.27	2.1	3.55	0.215
53	Diethylamine	73.1	0.71	3.68	0.9	3.74	0.252
54	Diethyl carbonate	118.1	0.97	2.82	1.1	4.17	0.353
55	Diethyl ether	74.1	0.71	4.27	1.1	3.75	0.259
56	N,N-Dimethylformamide	73.1	0.94	38.25	3.8	3.08	0.122
57	Dimethyl sulfide	62.1	0.85	6.70	1.6	2.97	0.294
58	Dimethyl sulfoxide	78.1	1.10	47.24	4.0	2.91	0.109
59	Dipropyl ether	102.2	0.75	3.38	1.2	4.50	0.299
60	1,2-Ethanediamine	60.1	0.90	13.82	2.0	2.79	0.194
61	1,2-Ethanediol	62.1	1.11	41.42	2.4	2.47	0.087
62	1,2-Ethanedithiol	94.2	1.23	7.26	2.0	3.05	0.345
63	Ethanol	46.1	0.79	25.32	1.7	2.55	0.099
64	Ethanolamine	61.1	1.02	31.94	3.1	2.60	0.138
65	Ethoxybenzene	122.2	0.97	4.22	1.5	4.27	0.303
66	Ethyl acetate	88.1	0.90	6.08	1.8	3.60	0.306
67	Ethylamine	45.1	0.69	8.70	1.2	2.75	0.192
68	Ethylbenzene	106.2	0.87	2.45	0.6	4.18	0.217
69	Ethyl benzoate	150.2	1.04	6.20	2.0	4.66	0.261
70	Ethyl butanoate	116.2	0.87	5.18	1.7	4.42	0.286
71	Ethyl formate	74.1	0.92	8.57	1.9	3.16	0.269
72	Fluorobenzene	96.1	1.02	5.47	1.6	3.50	0.315
73	Formamide	45.0	1.13	111.02	3.7	1.97	0.064
74	Formic acid	46.0	1.22	51.13	1.4	1.91	0.055
75	Furan	68.1	0.95	2.94	0.7	2.92	0.289
76	Hydrazine	32.0	1.00	51.73	1.8	1.71	0.075
77	Hydrogen cyanide	27.0	0.69	114.92	3.0	1.96	0.050
78	Hydrogen peroxide	34.0	1.44	74.62	1.6	1.40	0.057
79	Iodobenzene	204.0	1.83	4.59	1.7	3.93	0.355
80	Iodoethane	156.0	1.94	7.82	2.0	3.16	0.301
81	Iodomethane	141.9	2.28	6.97	1.6	2.66	0.333
82	1-Iodopropane	170.0	1.75	7.07	2.0	3.58	0.303
83	Isopentane	72.1	0.62	1.85	0.1	4.04	0.066

Table D-1 continued

Table D-1 continued

84	Isopropylamine	59.1	0.69	5.63	1.2	3.30	0.242
85	Isoquinoline	129.2	1.09	11.03	2.7	4.09	0.228
86	Methanol	32.0	0.79	33.02	1.7	2.00	0.096
87	2-Methoxyethanol gauche	76.1	0.96	17.23	2.4	3.12	0.166
88	Methyl acetate	74.1	0.93	7.07	1.7	3.13	0.293
89	2-Methyl-1,3-butadiene	68.1	0.68	2.10	0.3	3.66	0.123
90	N-Methylformamide	59.1	1.01	189.02	3.8	2.55	0.030
91	Methyl formate	60.1	0.97	9.20	1.8	2.65	0.277
92	2-Methylpropanenitrile	69.1	0.77	24.42	4.1	3.40	0.185
93	2-Methyl-2-propanethiol	90.2	0.79	5.48	1.7	3.98	0.287
94	2-Methyl-1-propanol	74.1	0.80	17.93	1.6	3.47	0.099
95	2-Methylpyridine	93.1	0.94	10.18	1.9	3.62	0.189
96	4-Methylpyridine	93.1	0.95	12.22	2.7	3.59	0.232
97	N-Methyl-2-pyrrolidinone	99.1	1.02	32.55	4.1	3.58	0.133
98	Morpholine	87.1	1.00	7.42	1.6	3.33	0.236
99	Nitrobenzene	123.1	1.20	35.62	4.2	3.71	0.120
100	Nitroethane	75.1	1.04	29.11	3.2	2.93	0.143
101	Nitromethane	61.0	1.14	37.27	3.5	2.41	0.145
102	1-Nitropropane	89.1	1.00	24.70	3.7	3.39	0.165
103	2-Nitropropane	89.1	0.98	26.74	3.7	3.42	0.154
104	Oxirane	44.1	0.88	12.42	1.9	2.30	0.249
105	Pentachloroethane	202.3	1.68	3.72	0.9	4.13	0.226
106	cis-1,3-Pentadiene	68.1	0.69	2.32	0.5	3.62	0.224
107	Pentyl acetate	130.2	0.88	4.79	1.8	4.76	0.289
108	Phenol	94.1	1.05	12.40	1.2	3.39	0.110
109	Propanal gauche	58.1	0.87	18.52	2.9	2.80	0.208
110	Propanal cis	58.1	0.87	18.52	2.5	2.80	0.183
111	Propanenitrile	55.1	0.78	29.72	4.1	2.89	0.178
112	Propanoic acid cis	74.1	0.99	3.44	1.5	3.01	0.530
113	1-Propanol gauche	60.1	0.80	20.82	1.6	3.01	0.095
114	1-Propanol trans	60.1	0.80	20.82	1.6	3.01	0.093
115	2-Propanol trans	60.1	0.79	20.18	1.6	3.06	0.097

Continued

Table D-1 continued

Table D-1 continued

116	Propargyl alcohol	56.1	0.95	20.82	1.1	2.57	0.079
117	Propylamine	59.1	0.72	5.08	1.2	3.21	0.270
118	Pyridine	79.1	0.98	13.26	2.2	3.16	0.199
119	Pyrrole	67.1	0.97	8.00	1.8	2.86	0.291
120	Quinoline	129.2	1.10	9.16	2.3	4.07	0.231
121	Salicylaldehyde	122.1	1.17	18.35	3.0	3.76	0.161
122	Styrene	104.2	0.90	2.47	0.1	4.02	0.047
123	1,1,2,2-Tetrachloroethane	167.8	1.60	8.50	1.3	3.78	0.155
124	Tetrahydrofuran	72.1	0.88	7.52	1.8	3.19	0.275
125	Thiophene	84.1	1.06	2.74	0.6	3.12	0.242
126	Toluene	92.1	0.87	2.38	0.4	3.80	0.156
127	Tribromomethane	252.7	2.88	4.40	1.0	3.35	0.253
128	1,1,1-Trichloroethane	133.4	1.34	7.24	1.8	3.64	0.251
129	Trichlorofluoromethane	137.4	1.49	3.00	0.5	3.46	0.167
130	Trichloromethane	119.4	1.49	4.81	1.0	3.15	0.259
131	Triethylamine	101.2	0.73	2.42	0.7	4.55	0.226
132	Trifluoroacetic acid	114.0	1.54	8.42	2.3	3.00	0.340
133	(Trifluoromethyl)benzene	146.1	1.19	9.22	2.9	4.19	0.279
134	Water	18.0	1.00	80.12	1.9	1.17	0.075
135	o-Xylene	106.2	0.88	2.56	0.6	4.14	0.227
136	Acetamide	59.1	1.00	67.60	3.7	2.57	0.080
137	Ammonia	106.1	1.04	16.61	1.5	3.70	0.090
138	1-Bromoheptane	179.1	1.14	5.26	2.2	4.94	0.314
139	Bromomethane	94.9	1.68	9.71	1.8	2.50	0.282
140	1-Chloro-2-nitrobenzene	157.6	1.37	37.70	4.6	4.01	0.116
141	1-Chloro-3-nitrobenzene	157.6	1.34	20.90	3.7	4.06	0.166
142	1-Chloro-4-nitrobenzene	157.6	1.30	8.09	2.8	4.16	0.318
143	4-Chlorophenol	128.6	1.27	11.18	2.1	3.69	0.193
144	N,N-Dimethylaniline	121.2	0.96	5.15	1.7	4.28	0.288
145	2,2-Dimethylpropanal	86.1	0.79	9.05	2.7	3.86	0.287
146	2,2-Dimethylpropanenitrile	83.1	0.76	21.20	4.0	3.88	0.181

Table D-1 continued

Table D-1 continued

147	Divinyl ether	70.1	0.77	3.94	0.8	3.42	0.219
148	Ethyleneimine	43.1	0.83	18.30	1.9	2.35	0.166
149	2-Fluorotoluene	110.1	1.00	4.23	1.4	3.88	0.316
150	3-Fluorotoluene	110.1	1.00	5.41	1.8	3.90	0.326
151	4-Fluorotoluene	110.1	1.00	5.88	2.0	3.90	0.329
152	1-Hexyne	82.1	0.72	2.62	0.8	4.00	0.300
153	2-Iodobutane, (±)-	184.0	1.59	7.87	2.1	4.02	0.252
154	2-Methylfuran	82.1	0.91	2.76	0.7	3.40	0.263
155	Pentyl formate	116.2	0.89	5.70	1.9	4.38	0.287
156	Phenylacetylene	102.1	0.93	2.98	0.7	3.89	0.213
157	2-Pyridinecarbonitrile	104.1	1.08	93.77	5.8	3.56	0.065
158	3-Pyridinecarbonitrile	104.1	1.16	20.54	3.7	3.40	0.197
159	4-Pyridinecarbonitrile	104.1	1.16	5.23	2.0	3.40	0.416
160	1,3,5-Trioxane	90.1	1.17	15.55	2.1	3.07	0.164
161	Acetic anhydride	102.1	1.08	22.45	2.8	3.51	0.134
162	3-Bromopropene	121.0	1.40	7.02	1.9	3.32	0.307
163	Butylamine	73.1	0.74	4.71	1.0	3.62	0.221
164	tert-Butylbenzene	134.2	0.87	2.36	0.8	4.89	0.271
165	Cyclopentanone	84.1	0.95	13.58	3.3	3.37	0.272
166	Isopropylbenzene	120.2	0.86	2.38	0.8	4.56	0.274
167	Methyl isocyanate	57.1	0.96	21.75	2.8	2.58	0.188
168	1-Pentene	70.1	0.64	2.01	0.5	3.88	0.241
169	Diphenyl ether	170.2	1.07	3.73	1.3	4.99	0.263

D.2 Selected solvents with dipole moments of molecules (liquid phase)

Table D-2. Selected solvents with dipole moments of molecules (liquid phase)

	Solvent	M	ρ	ε_s	μ	A (x10^{-19})	V_D
		g/mol	g/cm^3		D	m^2/molecule	volts
1	Benzeneacetonitrile	117.1	1.02	17.87	3.5	4.00	0.184
2	Benzenethiol	110.2	1.08	4.26	1.2	3.71	0.293
3	Benzyl acetate	150.2	1.06	5.34	1.2	4.62	0.186
4	Bis(2-aminoethyl)amine	103.2	0.96	12.62	1.9	3.84	0.147
5	Bis(2-chloroethyl) ether	143.0	1.22	21.20	2.6	4.06	0.113
6	2-Bromo-2-methylpropane	137.0	1.43	10.98	2.2	3.55	0.209
7	1-Bromopentane	151.0	1.22	6.31	2.2	4.22	0.311
8	1,4-Butanediol	90.1	1.02	31.93	2.6	3.37	0.090
9	1-Butanethiol	90.2	0.84	5.20	1.5	3.82	0.290
10	Butanoic acid	88.1	0.95	2.98	1.7	3.47	0.601
11	Butyl acetate	116.2	0.88	5.07	1.9	4.39	0.317
12	sec-Butyl acetate	116.2	0.87	5.14	1.9	4.41	0.311
13	2-Chloroaniline	127.6	1.21	13.40	1.8	3.78	0.132
14	(Chloromethyl)benzene	126.6	1.10	6.85	1.8	4.01	0.249
15	1-Chlorooctane	148.7	0.87	5.05	2.0	5.21	0.286
16	o-Cresol	108.1	1.03	6.76	1.5	3.77	0.214

Table D-2 continued

Table D-2 continued

17	m-Cresol	108.1	1.03	12.44	1.5	3.76	0.119
18	p-Cresol	108.1	1.02	13.05	1.5	3.80	0.112
19	Cyclohexylamine	99.2	0.82	4.55	1.3	4.15	0.252
20	Diacetone alcohol	116.2	0.94	18.23	3.2	4.21	0.159
21	1,2-Dibromoethane	187.9	2.17	4.96	1.2	3.32	0.272
22	Dibutyl phthalate	278.3	1.05	6.58	2.8	7.01	0.230
23	Dibutyl sebacate	314.5	0.94	4.54	2.5	8.17	0.252
24	Dibutyl sulfide	146.3	0.84	4.29	1.6	5.29	0.267
25	1,2-Dichloroethane	99.0	1.25	10.42	1.8	3.13	0.211
26	(Dichloromethyl)benzene	161.0	1.26	6.92	2.1	4.30	0.262
27	1,2-Dichloropropane, (±)-	113.0	1.16	8.37	1.9	3.60	0.231
28	2,4-Dichlorotoluene	161.0	1.25	5.68	1.7	4.33	0.260
29	Diethanolamine	105.1	1.10	25.75	2.8	3.55	0.115
30	Diethylene glycol	106.1	1.12	31.82	2.3	3.52	0.078
31	Diethylene glycol dimethyl ether	134.2	0.94	7.23	2.0	4.62	0.222
32	Diethyl malonate	160.2	1.06	7.55	2.5	4.82	0.263
33	Diethyl oxalate	146.1	1.08	8.27	2.5	4.47	0.254
34	Diiodomethane	267.8	3.32	5.32	1.1	3.16	0.242
35	Diisopentyl ether	158.3	0.78	2.82	1.2	5.87	0.280
36	Diisopropyl ether	102.2	0.72	3.81	1.1	4.62	0.242
37	Dimethoxymethane	76.1	0.86	2.64	0.7	3.37	0.313
38	N,N-Dimethylacetamide	87.1	0.94	38.85	3.7	3.48	0.103

Continued

Table D-2 continued

39	Dimethyl disulfide	94.2	1.06	9.63	1.9	3.37	0.215
40	2,6-Dimethyl-4-heptanone	142.2	0.81	9.91	2.7	5.33	0.190
41	2,6-Dimethylpyridine	107.2	0.92	7.33	1.7	4.04	0.211
42	Dipentyl ether	158.3	0.78	2.80	1.2	5.84	0.277
43	Dipropylamine	101.2	0.74	2.92	1.0	4.50	0.295
44	Epichlorohydrin	92.5	1.18	22.62	1.8	3.10	0.097
45	1,2-Ethanediol, diacetate	146.1	1.10	7.72	2.3	4.40	0.259
46	2-Ethoxyethanol	90.1	0.93	13.38	2.1	3.59	0.163
47	2-Ethoxyethyl acetate	132.2	0.97	7.57	2.3	4.48	0.250
48	Ethyl acrylate	100.1	0.92	6.05	2.0	3.85	0.316
49	Ethyl cyanoacetate	113.1	1.07	31.62	2.2	3.80	0.068
50	2-Ethyl-1-hexanol	130.2	0.83	7.58	1.7	4.92	0.176
51	Ethyl lactate	118.1	1.03	15.43	2.4	3.99	0.147
52	Ethyl propanoate	102.1	0.89	5.76	1.7	4.00	0.284
53	Furfural	96.1	1.16	42.12	3.5	3.22	0.098
54	Furfuryl alcohol	98.1	1.13	16.85	1.9	3.32	0.129
55	Glycerol	92.1	1.26	46.53	2.6	2.96	0.070
56	2-Heptanone	114.2	0.81	11.95	2.6	4.59	0.178
57	3-Heptanone	114.2	0.82	12.72	2.8	4.56	0.181
58	Hexamethylphosphoric triamide	179.2	1.03	31.32	5.5	5.28	0.125
59	Hexanoic acid	116.2	0.93	2.60	1.1	4.24	0.386
60	2-Hexanone	100.2	0.81	14.56	2.7	4.20	0.164

Table D-2 continued

61	1-Iodobutane	184.0	1.62	6.27	1.9	3.98	0.291
62	2-Iodopropane	170.0	1.70	8.19	2.0	3.65	0.246
63	Isobutyl formate	102.1	0.88	6.41	1.9	4.04	0.273
64	Isopentyl acetate	130.2	0.88	4.72	1.9	4.76	0.312
65	Mesityl oxide	98.1	0.87	15.60	2.8	3.97	0.170
66	Methyl acrylate	86.1	0.95	7.03	1.8	3.41	0.278
67	2-Methylaniline	107.2	1.00	6.14	1.6	3.83	0.256
68	3-Methylaniline	107.2	0.99	5.82	1.5	3.85	0.244
69	Methyl benzoate	136.1	1.08	6.64	1.9	4.25	0.259
70	2-Methyl-2-butanol	88.1	0.81	5.78	1.8	3.87	0.307
71	Methyl methacrylate	100.1	0.94	6.32	1.7	3.82	0.261
72	2-Methyl-2,4-pentanediol	118.2	0.92	25.86	2.9	4.31	0.098
73	2-Methylpropanoic acid	88.1	0.97	2.58	1.1	3.43	0.459
74	2-Methyl-2-propanol	74.1	0.79	12.47	1.7	3.50	0.143
75	3-Methylpyridine	93.1	0.96	11.10	2.4	3.59	0.227
76	Methyl salicylate	152.1	1.18	8.80	2.5	4.32	0.244
77	2-Nitroanisole	153.1	1.25	45.75	5.0	4.17	0.099
78	Nonanoic acid	158.2	0.91	2.48	0.8	5.30	0.227
79	cis-9-Octadecenoic acid	282.5	0.89	2.34	1.2	7.87	0.242
80	Octanoic acid	144.2	0.91	2.85	1.2	4.96	0.306
81	1-Octanol	130.2	0.83	10.30	1.8	4.95	0.130
82	2-Octanol	130.2	0.82	8.13	1.7	4.97	0.159

Table D-2 continued

Table D-2 continued

83	2-Octanone	128.2	0.82	9.51	2.7	4.92	0.217
84	1,5-Pentanediol	104.1	0.99	26.22	2.5	3.77	0.095
85	2,4-Pentanedione	100.1	0.97	26.52	2.8	3.72	0.106
86	Pentanoic acid	102.1	0.94	2.66	1.6	3.86	0.590
87	1-Pentanol	88.1	0.81	15.13	1.7	3.85	0.110
88	2-Pentanol	88.1	0.81	13.71	1.7	3.87	0.118
89	3-Pentanol	88.1	0.82	13.35	1.6	3.83	0.121
90	2-Pentanone	86.1	0.81	15.45	2.7	3.81	0.173
91	3-Pentanone	86.1	0.81	17.00	2.8	3.81	0.164
92	Piperidine equitorial	85.1	0.86	4.33	0.8	3.63	0.197
93	Piperidine axial	85.1	0.86	4.33	1.2	3.63	0.285
94	1,2-Propanediol gG't	76.1	1.04	27.53	2.3	2.97	0.104
95	1,3-Propanediol	76.1	1.05	35.12	2.6	2.94	0.093
96	Propyl acetate	102.1	0.89	5.62	1.8	4.01	0.298
97	Propylene carbonate	102.1	1.20	66.14	4.9	3.27	0.085
98	Propyl formate	88.1	0.91	6.92	1.9	3.59	0.287
99	Pyrrolidine	71.1	0.86	8.30	1.6	3.22	0.221
100	2-Pyrrolidone	85.1	1.12	28.18	3.5	3.04	0.154
101	1,1,2,2-Tetrabromoethane	345.7	2.97	6.72	1.4	4.05	0.191
102	Tetrahydrofurfuryl alcohol	102.1	1.05	13.48	2.1	3.58	0.164
103	Tetramethylurea	116.2	0.97	23.10	3.5	4.12	0.138
104	Tributylamine	185.3	0.78	2.34	0.8	6.52	0.193

Table D-2 continued

Table D-2 continued

105	Tributyl borate	230.2	0.86	2.23	0.8	7.06	0.184
106	1,1,2-Trichloroethane	133.4	1.44	7.19	1.4	3.47	0.211
107	Trichloroethene	131.4	1.46	3.39	0.8	3.40	0.262
108	Tri-o-cresyl phosphate	368.4	1.20	6.73	2.9	7.73	0.208
109	Triethyl phosphate	182.2	1.07	13.20	3.1	5.21	0.171
110	Trimethyl phosphate	140.1	1.21	20.62	3.2	4.02	0.145
111	2,4,6-Trimethylpyridine	121.2	0.92	7.81	2.1	4.40	0.225
112	Benzaldehyde	106.1	1.04	17.85	3.0	3.70	0.171
113	Benzyl benzoate	212.2	1.11	5.26	2.1	5.62	0.263
114	1-Bromo-2-chloroethane	143.4	1.74	7.41	1.2	3.21	0.190
115	1-Bromodecane	221.2	1.07	4.07	1.9	5.93	0.301
116	1-Bromonaphthalene	207.1	1.48	4.77	1.6	4.57	0.268
117	1-Chloro-3-methylbutane	106.6	0.88	6.10	1.9	4.17	0.285
118	3-Chlorotoluene	126.6	1.08	5.76	1.8	4.07	0.292
119	1,2-Dibromopropane	201.9	1.93	4.60	1.2	3.76	0.261
120	Dibutylamine	129.2	0.77	2.77	1.0	5.17	0.258
121	Ethylene carbonate	88.1	1.32	89.78	4.9	2.79	0.074
122	2-Heptanol, (±)-	116.2	0.82	9.72	1.7	4.62	0.143
123	3-Heptanol, (S)-	116.2	0.82	7.07	1.7	4.60	0.198
124	Isobutyl acetate	116.2	0.87	5.07	1.9	4.42	0.312
125	4-Methylaniline	107.2	0.96	5.06	1.5	3.93	0.288
126	2-Methyl-1-butanol, (±)-	88.1	0.82	15.63	1.9	3.85	0.118

Continued

Table D-2 continued

Table D-2 continued

127	Succinonitrile	80.1	0.99	62.60	3.7	3.18	0.070
128	Tributyl phosphate	266.3	0.97	8.34	3.1	7.15	0.194
129	2,4-Xylenol	122.2	0.97	5.06	1.4	4.27	0.244
130	2,5-Xylenol	122.2	0.97	5.36	1.5	4.27	0.238
131	2,6-Xylenol	122.2	0.97	4.90	1.4	4.27	0.252
132	3,4-Xylenol	122.2	0.98	9.02	1.6	4.22	0.154
133	3,5-Xylenol	122.2	0.97	9.06	1.5	4.27	0.146

137

Appendix E. Surface Potential Data Tables (Figures in Chapters 2-5)

Entire data sets have been compiled in spreadsheets (Microsoft Excel) which are available in two locations: (1) Allen _Tehseen Adel Data - Allen Data Share (Microsoft Teams) (2) Flash drive labeled "Tehseen Adel Surface Potential".

E.1 Experimental controls

Table E-1. Impact of ionizing environments on the measured potentials of 0.3 mM sodium dodecyl sulfate (SDS) and cetyltrimethylammonium bromide (CTAB).

	0.3 mM SDS		0.3 mM CTAB	
	Avg	*Stdev*	*Avg*	*Stdev*
N$_2$/Pt	-0.499	0.04	+0.173	0.06
He/Pt	-0.400	0.06	+0.196	0.05
Ar/Pt	-0.415	0.07	+0.356	0.08
N$_2$/Au	-0.834	0.10	-0.101	0.11

Table E-2. Measured surface potentials for aqueous NaCl on platinum (Pt) vs. gold (Au).

NaCl	N$_2$/Pt		N$_2$/Au	
mol/L	*Avg*	*Stdev*	*Avg*	*Stdev*
0.24	-0.30	0.02	-0.68	0.02
0.42	-0.25	0.03	-0.61	0.02
0.60	-0.23	0.03	-0.58	0.01
0.78	-0.20	0.02	-0.56	0.01
0.96	-0.18	0.01	-0.51	0.02
1.41	-0.15	0.01	-0.49	0.02
1.86	-0.14	0.01	-0.44	0.02
2.31	-0.12	0.01	-0.42	0.02
2.76	-0.09	0.02	-0.41	0.02

E.2 Real-time voltage data

Table E-3. Real-time voltage data for water and aqueous sodium salts.

t (s)	Water		1.0 M NaCl		1.0 M Na$_2$SO$_4$	
	Avg	Stdev	Avg	Stdev	Avg	Stdev
0	-0.06	0.01	-0.05	0.01	-0.06	0.01
1	-0.10	0.01	-0.08	0.01	-0.10	0.01
2	-0.13	0.01	-0.10	0.01	-0.13	0.01
3	-0.16	0.01	-0.12	0.01	-0.16	0.01
4	-0.19	0.01	-0.15	0.01	-0.19	0.01
5	-0.22	0.01	-0.16	0.01	-0.21	0.01
6	-0.24	0.01	-0.18	0.02	-0.23	0.02
7	-0.26	0.01	-0.20	0.02	-0.25	0.02
8	-0.28	0.01	-0.21	0.02	-0.27	0.02
9	-0.30	0.01	-0.22	0.02	-0.29	0.02
10	-0.31	0.01	-0.24	0.02	-0.30	0.02
11	-0.33	0.01	-0.25	0.02	-0.32	0.02
12	-0.34	0.01	-0.26	0.02	-0.33	0.02
13	-0.35	0.01	-0.27	0.02	-0.34	0.02
14	-0.37	0.01	-0.27	0.02	-0.35	0.02
15	-0.38	0.01	-0.28	0.02	-0.36	0.02
16	-0.39	0.01	-0.29	0.02	-0.37	0.02
17	-0.40	0.01	-0.30	0.02	-0.38	0.02
18	-0.40	0.01	-0.30	0.02	-0.38	0.02
19	-0.41	0.01	-0.31	0.02	-0.39	0.02
20	-0.42	0.01	-0.31	0.02	-0.40	0.02
21	-0.43	0.01	-0.32	0.02	-0.40	0.02
22	-0.43	0.02	-0.32	0.02	-0.41	0.02
23	-0.44	0.02	-0.33	0.02	-0.41	0.02
24	-0.44	0.02	-0.33	0.02	-0.41	0.02
25	-0.45	0.02	-0.33	0.02	-0.42	0.02
26	-0.45	0.02	-0.34	0.02	-0.42	0.02
27	-0.45	0.02	-0.34	0.02	-0.42	0.02
28	-0.46	0.02	-0.34	0.02	-0.43	0.02
29	-0.46	0.02	-0.34	0.02	-0.43	0.02
30	-0.46	0.02	-0.35	0.02	-0.43	0.02
31	-0.47	0.02	-0.35	0.02	-0.43	0.02
32	-0.47	0.02	-0.35	0.02	-0.44	0.02
33	-0.47	0.02	-0.35	0.02	-0.44	0.02
34	-0.47	0.02	-0.35	0.02	-0.44	0.02
35	-0.47	0.02	-0.36	0.02	-0.44	0.02
36	-0.48	0.01	-0.36	0.02	-0.44	0.02

Table E-3 continued

Table E-3 continued

37	-0.48	0.01	-0.36	0.02	-0.44	0.02
38	-0.48	0.02	-0.36	0.03	-0.44	0.02
39	-0.48	0.01	-0.36	0.03	-0.44	0.02
40	-0.48	0.02	-0.36	0.03	-0.44	0.02
41	-0.48	0.02	-0.36	0.03	-0.45	0.02
42	-0.48	0.02	-0.36	0.03	-0.45	0.02
43	-0.49	0.02	-0.36	0.03	-0.45	0.02
44	-0.49	0.02	-0.36	0.03	-0.45	0.02
45	-0.49	0.01	-0.37	0.03	-0.45	0.02
46	-0.49	0.01	-0.37	0.03	-0.45	0.02
47	-0.49	0.01	-0.37	0.03	-0.45	0.02
48	-0.49	0.01	-0.37	0.03	-0.45	0.02
49	-0.49	0.01	-0.37	0.03	-0.45	0.02
50	-0.49	0.01	-0.37	0.03	-0.45	0.02
51	-0.49	0.01	-0.37	0.03	-0.45	0.02
52	-0.49	0.01	-0.37	0.03	-0.45	0.02
53	-0.49	0.01	-0.37	0.03	-0.45	0.02
54	-0.49	0.01	-0.37	0.03	-0.45	0.02
55	-0.49	0.01	-0.37	0.03	-0.45	0.01
56	-0.49	0.01	-0.37	0.03	-0.45	0.01
57	-0.49	0.01	-0.37	0.03	-0.45	0.01
58	-0.49	0.01	-0.37	0.03	-0.45	0.01
59	-0.49	0.01	-0.37	0.03	-0.45	0.01
60	-0.49	0.01	-0.37	0.03	-0.45	0.01
61	-0.49	0.01	-0.37	0.03	-0.45	0.01
62	-0.49	0.01	-0.37	0.03	-0.45	0.01
63	-0.49	0.01	-0.37	0.03	-0.45	0.01
64	-0.49	0.01	-0.37	0.03	-0.45	0.01
65	-0.49	0.01	-0.37	0.03	-0.45	0.01
66	-0.49	0.01	-0.37	0.03	-0.45	0.01
67	-0.49	0.01	-0.37	0.03	-0.45	0.01
68	-0.49	0.01	-0.37	0.03	-0.45	0.01
69	-0.49	0.01	-0.38	0.03	-0.45	0.01
70	-0.49	0.01	-0.38	0.03	-0.45	0.01
71	-0.49	0.01	-0.38	0.03	-0.45	0.01
72	-0.49	0.01	-0.38	0.03	-0.45	0.01
73	-0.49	0.01	-0.38	0.03	-0.45	0.01
74	-0.49	0.01	-0.38	0.03	-0.45	0.01
75	-0.49	0.01	-0.38	0.03	-0.45	0.01
76	-0.49	0.01	-0.38	0.03	-0.45	0.01
77	-0.49	0.01	-0.38	0.03	-0.45	0.01
78	-0.49	0.01	-0.38	0.03	-0.45	0.01

Table E-3 continued

Table E-3 continued

79	-0.49	0.01	-0.38	0.03	-0.45	0.01
80	-0.49	0.01	-0.38	0.03	-0.45	0.01
81	-0.49	0.01	-0.38	0.03	-0.45	0.01
82	-0.49	0.01	-0.38	0.03	-0.45	0.01
83	-0.49	0.01	-0.38	0.03	-0.45	0.01
84	-0.49	0.01	-0.38	0.03	-0.45	0.01
85	-0.49	0.01	-0.38	0.03	-0.45	0.01
86	-0.49	0.01	-0.38	0.03	-0.45	0.01
87	-0.49	0.01	-0.38	0.03	-0.45	0.01
88	-0.49	0.01	-0.38	0.03	-0.45	0.01
89	-0.49	0.01	-0.38	0.03	-0.45	0.01
90	-0.49	0.01	-0.38	0.03	-0.45	0.01
91	-0.49	0.01	-0.38	0.03	-0.45	0.01
92	-0.49	0.01	-0.38	0.03	-0.45	0.01
93	-0.49	0.01	-0.38	0.03	-0.45	0.01
94	-0.49	0.01	-0.38	0.04	-0.45	0.01
95	-0.49	0.01	-0.38	0.04	-0.45	0.01
96	-0.49	0.01	-0.38	0.04	-0.45	0.01
97	-0.49	0.01	-0.38	0.04	-0.45	0.01
98	-0.49	0.01	-0.38	0.04	-0.45	0.01
99	-0.49	0.01	-0.38	0.04	-0.45	0.01
100	-0.49	0.01	-0.38	0.04	-0.45	0.01
101	-0.49	0.01	-0.38	0.04	-0.45	0.01
102	-0.49	0.01	-0.38	0.04	-0.45	0.01
103	-0.49	0.01	-0.38	0.04	-0.45	0.01
104	-0.49	0.01	-0.38	0.04	-0.45	0.01
105	-0.49	0.01	-0.38	0.04	-0.45	0.01
106	-0.49	0.01	-0.38	0.04	-0.45	0.01
107	-0.49	0.01	-0.38	0.04	-0.45	0.01
108	-0.49	0.01	-0.38	0.04	-0.45	0.01
109	-0.49	0.01	-0.38	0.04	-0.45	0.01
110	-0.49	0.01	-0.38	0.04	-0.45	0.01
111	-0.49	0.01	-0.38	0.04	-0.45	0.01
112	-0.49	0.01	-0.38	0.04	-0.45	0.01
113	-0.49	0.01	-0.38	0.04	-0.45	0.01
114	-0.49	0.01	-0.38	0.04	-0.45	0.01
115	-0.49	0.01	-0.38	0.04	-0.45	0.01
116	-0.49	0.01	-0.38	0.04	-0.45	0.01
117	-0.49	0.01	-0.38	0.04	-0.45	0.01
118	-0.49	0.01	-0.38	0.04	-0.45	0.01
119	-0.49	0.01	-0.38	0.04	-0.45	0.01
120	-0.49	0.01	-0.38	0.04	-0.45	0.01

Table E-3 continued

Table E-3 continued

121	-0.49	0.01	-0.38	0.04	-0.45	0.01
122	-0.49	0.01	-0.38	0.04	-0.45	0.01
123	-0.49	0.01	-0.38	0.04	-0.45	0.01
124	-0.49	0.01	-0.38	0.04	-0.45	0.01
125	-0.49	0.01	-0.38	0.04	-0.45	0.01
126	-0.49	0.01	-0.38	0.04	-0.45	0.01
127	-0.49	0.01	-0.38	0.04	-0.45	0.01
128	-0.49	0.01	-0.38	0.04	-0.45	0.01
129	-0.49	0.01	-0.38	0.04	-0.45	0.01
130	-0.49	0.01	-0.38	0.04	-0.45	0.01
131	-0.49	0.01	-0.38	0.04	-0.45	0.01
132	-0.49	0.01	-0.38	0.04	-0.45	0.01
133	-0.49	0.01	-0.38	0.04	-0.45	0.01
134	-0.49	0.01	-0.38	0.04	-0.45	0.01
135	-0.49	0.01	-0.38	0.04	-0.45	0.01
136	-0.49	0.01	-0.38	0.04	-0.45	0.01
137	-0.49	0.01	-0.38	0.04	-0.45	0.01
138	-0.49	0.01	-0.38	0.04	-0.45	0.01
139	-0.49	0.01	-0.38	0.04	-0.45	0.01
140	-0.49	0.01	-0.38	0.04	-0.45	0.01
141	-0.49	0.01	-0.38	0.04	-0.45	0.01
142	-0.49	0.01	-0.38	0.04	-0.45	0.01
143	-0.49	0.01	-0.38	0.04	-0.45	0.01
144	-0.49	0.01	-0.38	0.04	-0.45	0.01
145	-0.49	0.01	-0.38	0.04	-0.45	0.01
146	-0.49	0.01	-0.38	0.04	-0.45	0.01
147	-0.49	0.01	-0.38	0.04	-0.45	0.01
148	-0.49	0.01	-0.38	0.04	-0.44	0.01
149	-0.49	0.01	-0.38	0.04	-0.44	0.01
150	-0.49	0.01	-0.38	0.04	-0.44	0.01
151	-0.49	0.01	-0.38	0.04	-0.44	0.01
152	-0.49	0.01	-0.38	0.04	-0.44	0.01
153	-0.49	0.01	-0.38	0.04	-0.44	0.01
154	-0.49	0.01	-0.38	0.04	-0.44	0.01
155	-0.49	0.01	-0.38	0.04	-0.44	0.01
156	-0.49	0.01	-0.38	0.04	-0.44	0.01
157	-0.49	0.01	-0.38	0.04	-0.44	0.01
158	-0.49	0.01	-0.38	0.04	-0.44	0.01
159	-0.49	0.01	-0.38	0.04	-0.44	0.01
160	-0.49	0.01	-0.38	0.04	-0.44	0.01
161	-0.49	0.01	-0.38	0.04	-0.44	0.01
162	-0.49	0.01	-0.38	0.04	-0.44	0.01

Table E-3 continued

Table E-3 continued

163	-0.49	0.01	-0.38	0.04	-0.44	0.01
164	-0.49	0.01	-0.38	0.04	-0.44	0.01
165	-0.49	0.01	-0.38	0.04	-0.44	0.01
166	-0.49	0.01	-0.38	0.04	-0.44	0.01
167	-0.49	0.01	-0.38	0.04	-0.44	0.01
168	-0.49	0.01	-0.38	0.04	-0.44	0.01
169	-0.49	0.01	-0.38	0.04	-0.44	0.01
170	-0.49	0.01	-0.38	0.04	-0.44	0.01
171	-0.49	0.01	-0.38	0.04	-0.44	0.01
172	-0.49	0.01	-0.38	0.04	-0.44	0.01
173	-0.49	0.01	-0.38	0.04	-0.44	0.01
174	-0.49	0.01	-0.38	0.04	-0.44	0.01
175	-0.49	0.01	-0.38	0.04	-0.44	0.01
176	-0.49	0.01	-0.38	0.04	-0.44	0.01
177	-0.49	0.01	-0.39	0.04	-0.44	0.01
178	-0.49	0.01	-0.39	0.04	-0.44	0.01
179	-0.49	0.01	-0.39	0.04	-0.44	0.01
180	-0.49	0.01	-0.39	0.04	-0.44	0.01

E.3 Halide ion adsorption data

Table E-4. Measured surface potentials for aqueous halide salts (as per 4.2)

REAL			
(a.) _Real "measured surface potential"_ NaCl			
Concentration (mol/kg water)	Concentration (mol/L)	Measured Potential (volts)	Error ($n \geq 3$) (volts)
0.20	0.24	-0.304	0.020
0.40	0.42	-0.255	0.029
0.60	0.60	-0.233	0.025
0.80	0.78	-0.203	0.016
1.00	0.96	-0.180	0.007
1.50	1.41	-0.153	0.007
2.00	1.86	-0.139	0.009
2.50	2.31	-0.117	0.007
3.00	2.76	-0.085	0.018

Continued

Table E-4 continued

Table E-4 continued

(b.) _Real_ "_measured surface potential_" _NaBr_

Concentration (mol/kg water)	Concentration (mol/L)	Measured Potential (volts)	Error (n ≥ 3) (volts)
0.20	0.29	-0.220	0.033
0.40	0.46	-0.158	0.024
0.60	0.63	-0.107	0.028
0.80	0.80	-0.071	0.023
1.00	0.97	-0.037	0.023
1.50	1.40	-0.020	0.015
2.00	1.83	0.011	0.019
2.50	2.26	0.044	0.018
3.00	2.69	0.079	0.030

(c.) _Real_ "_measured surface potential_" _NaI_

Concentration (mol/kg water)	Concentration (mol/L)	Measured Potential (volts)	Error (n ≥ 3) (volts)
0.20	0.37	0.013	0.015
0.40	0.52	0.057	0.005
0.60	0.67	0.083	0.008
0.80	0.82	0.117	0.016
1.00	0.97	0.129	0.008
1.50	1.34	0.167	0.015
2.00	1.71	0.211	0.018
2.50	2.08	0.210	0.004
3.00	2.45	0.223	0.016

Table E-5. Normalized surface potentials for aqueous halide salts (as described in 4.3)

NORMALIZED			
(a.) _Normalized_ "measured surface potential" NaCl			
Concentration (mol/kg water)	Concentration (mol/L)	Measured Potential (volts)	Error (n ≥ 3) (volts)
0.20	0.243	0.052	0.029
0.40	0.423	0.126	0.042
0.60	0.603	0.159	0.038
0.80	0.782	0.203	0.023
1.00	0.962	0.237	0.010
1.50	1.411	0.278	0.011
2.00	1.860	0.299	0.014
2.50	2.309	0.331	0.010
3.00	2.758	0.378	0.027
(b.) _Normalized_ "measured surface potential" NaBr			
Concentration (mol/kg water)	Concentration (mol/L)	Measured Potential (volts)	Error (n ≥ 3) (volts)
0.20	0.287	0.178	0.049
0.40	0.459	0.270	0.035
0.60	0.631	0.346	0.041
0.80	0.802	0.400	0.034
1.00	0.974	0.450	0.035
1.50	1.404	0.475	0.022
2.00	1.833	0.520	0.028
2.50	2.263	0.570	0.027
3.00	2.692	0.622	0.045
(c.) _Normalized_ "measured surface potential" NaI			
Concentration (mol/kg water)	Concentration (mol/L)	Measured Potential (volts)	Error (n ≥ 3) (volts)
0.20	0.373	0.524	0.023
0.40	0.522	0.589	0.007
0.60	0.670	0.628	0.012
0.80	0.818	0.678	0.024
1.00	0.966	0.697	0.012
1.50	1.337	0.753	0.022
2.00	1.707	0.818	0.027
2.50	2.078	0.817	0.006
3.00	2.448	0.836	0.024

E.4 Solvent real-time voltage data (Figure 5-2 & 5-3)
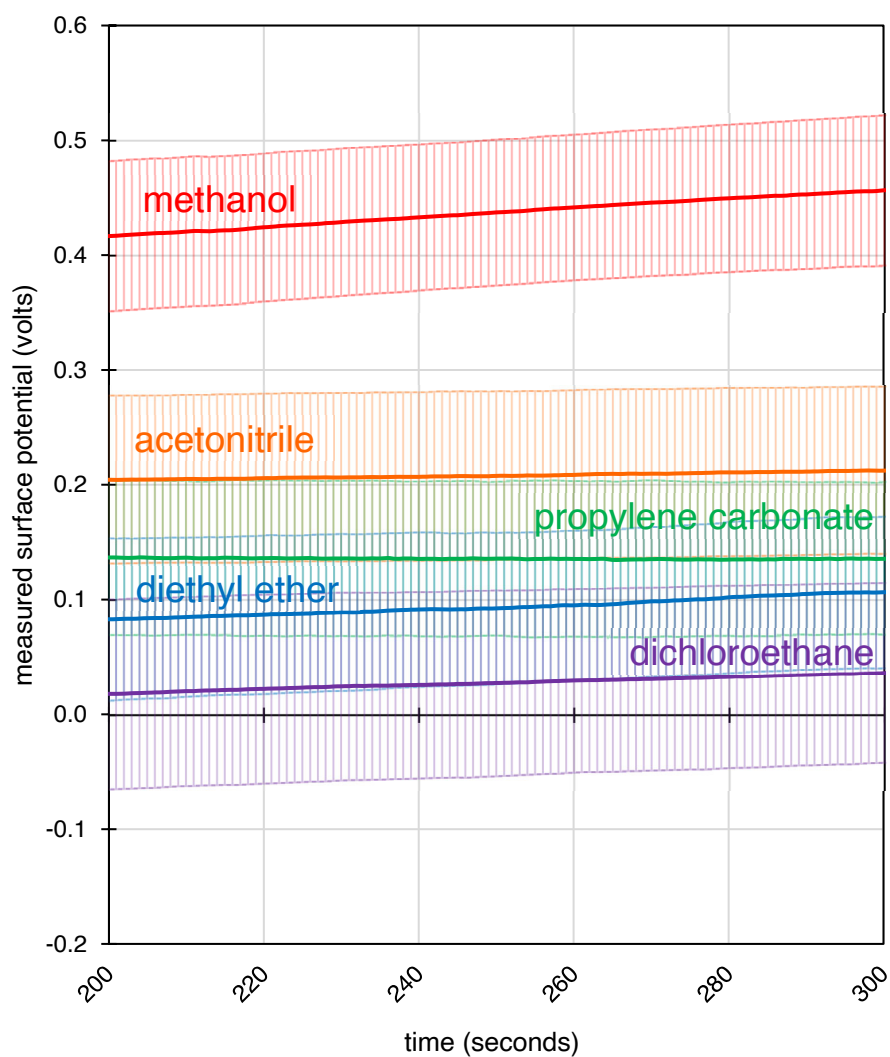

Figure E-1. Averaged measured surface potential (volts) vs. time (seconds) for solvents (n = 4). Error bars indicate standard deviation. Reported surface potentials (Table 5-1) are real-time values averaged between 200 and 300 seconds.

Appendix F. Supplementary Surface Potential (Figures & Tables)

The data shown within this section is supplemental to the published work (presented within the chapters of this dissertation). The data (presented as figures) are categorized in two sub-sections: (1) surface-level clean, and (2) solution-level clean. Under "surface-level clean", data has been collected under the strictest of cleaning regiments which include (i.) purification of the stock salt solution (using methods outlined in Table F-1), (ii.) rigorous rinsing of the ionizing cell with ultrapure water and reagent alcohol, (iii.) electrochemical cleaning of the Pt gauze surface, (iv.) degassing of ultrapure water with Ar (99.998% prepurified, Praxair) for nearly 2 mins before diluting a stock concentration to the appropriate concentration and (v.) aspiration of the solution surface before measurement. "Solution-level clean" simply involves steps (i.), (ii.), and (v.) before measurement.

Entire data sets have been compiled in spreadsheets (Microsoft Excel) which are available in two locations: (1) Allen _Tehseen Adel Data - Allen Data Share (Microsoft Teams) (2) Flash drive labeled "Tehseen Adel Surface Potential".

Table F-1. Summary of aqueous salt purification methods used in this dissertation. For a more comprehensive list, refer to Hua et al. (ref. 52)

| Aqueous Salt	Purification
Na$_2$SO$_4$ (99%, extra pure, anhydrous, ACROS Organics) **NaCl** (99+% for analysis, ACROS Organics) **NaBr** (≥99%, ACROS Organics Extra Pure)	Heated in the air to 600 °C in a furnace (>7 hours)
NaNO$_3$ (99+%, ACS reagent, ACROS Organics) **NaI.2H$_2$O** (99+%, for analysis, ACROS Organics)	0.2 μm PVFD Syringe Filters (Non-Sterile, Fisherbrand™ Basix™)
NaSCN (98+%, for analysis, ACROS Organics) **MgCl$_2$.6H$_2$O** (99%, for analysis, ACROS Organics) **MgSO$_4$** (99%, for analysis, anhydrous, ACROS Organics) **Mg(NO$_3$)$_2$.6H$_2$O** (99+%, for analysis, ACROS Organics)	Activated carbon with HEPA cartridge (Whatman 6704-1500 Carbon Cap 150)
FeCl$_3$.6H$_2$O (99+%, for analysis, ACROS Organics) **Fe(NO$_3$)$_3$.9H$_2$O** (99+%, for analysis, ACROS Organics)	Crystals directly dissolved in ultrapure water without further purification

F.1 Surface-level clean aqueous Na salts
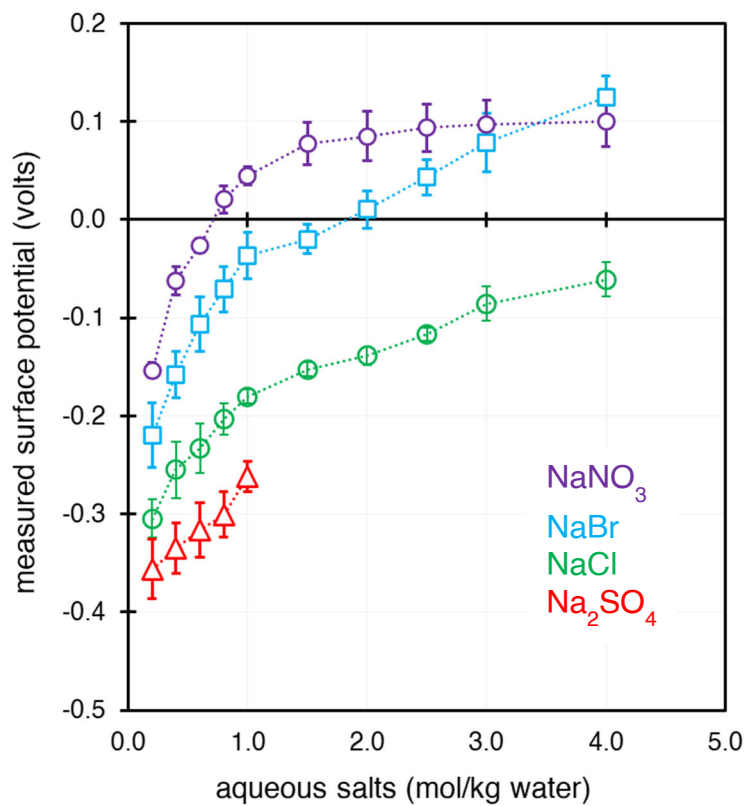
Figure F-1. Surface potentials for aqueous NaNO₃ and Na₂SO₄ were measured alongside aqueous sodium halides (Figure 4-6) and use the same 0.3 mM SDS and CTAB values as Figure 4-5. Lines indicate trend only.

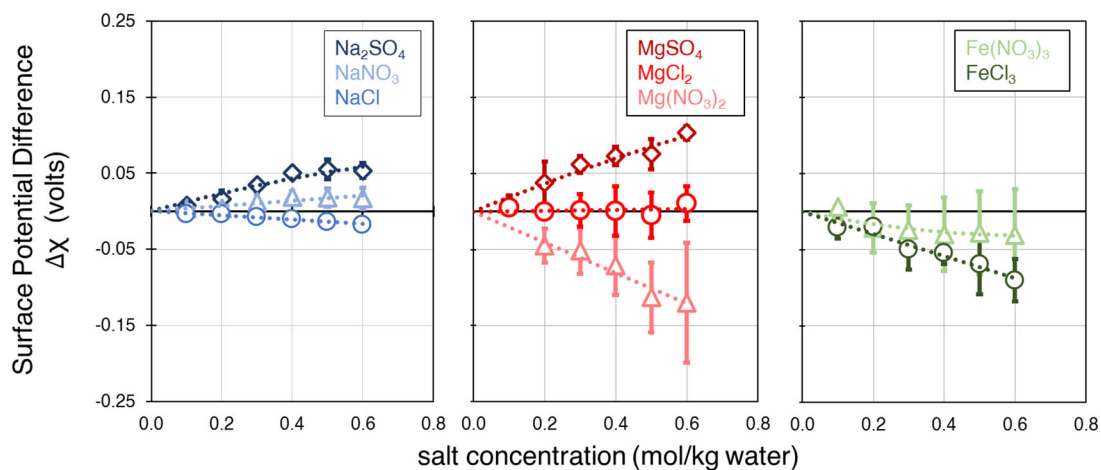## F.2 Solution-level clean data for aqueous the following Na, Mg, and Fe(III) salts

Figure F-2. Surface potential difference ($\Delta\chi$ where $\Delta\chi = \chi_{salt} - \chi_0$) versus salt concentration (mol/kg water) for 3 metal cations from 0.1 to 0.6 molal concentration. The $\Delta\chi$ reported are in terms of changes in the χ_{salt} (via directly measurable potential V_M) relative to an extrapolated term at infinite dilution (χ_0). Lines indicate trend only. The lack of electrochemical cleaning of electrodes and degassing of the solutions has resulted in larger than usual error bars, which is strikingly noticeable for the aqueous Mg and Fe(III) salts.
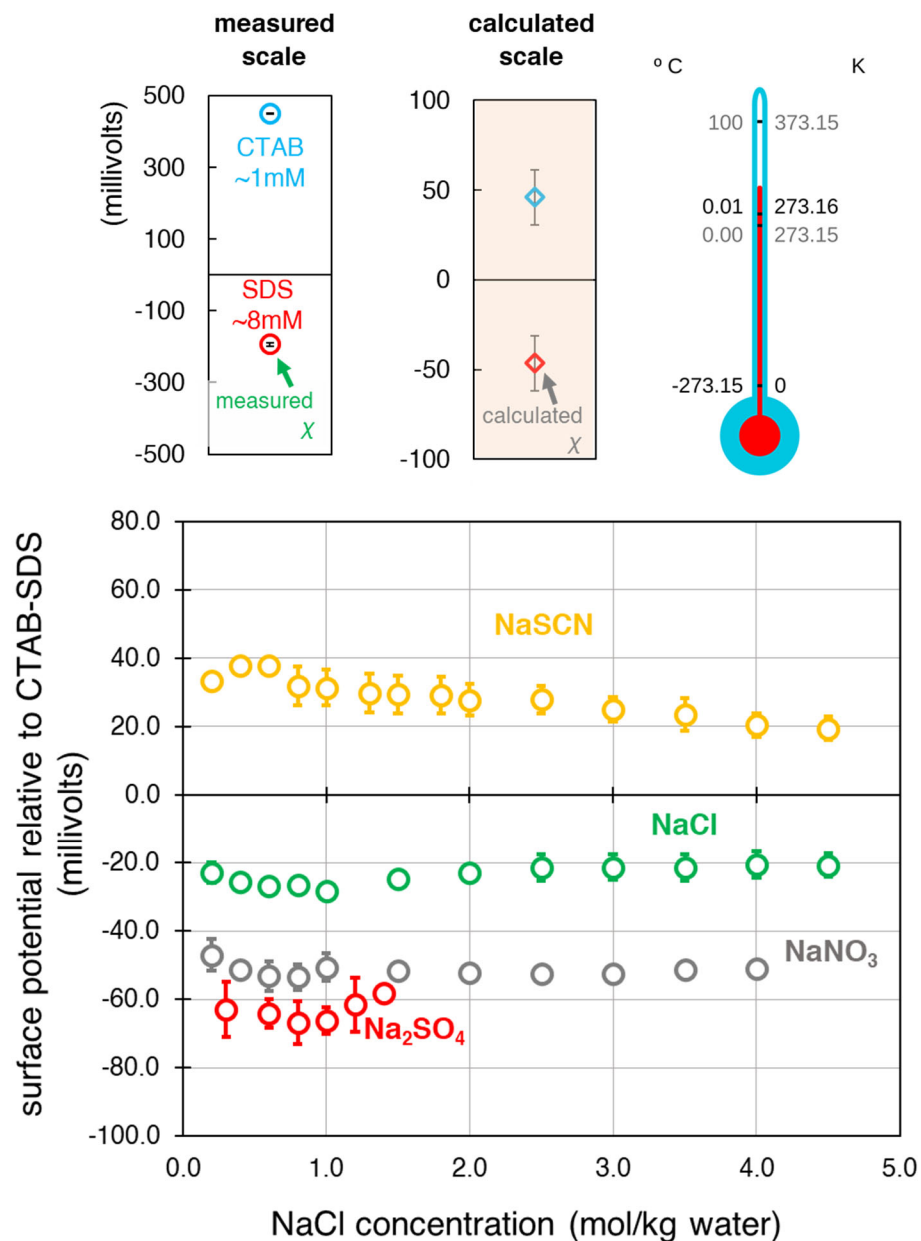
Figure F-3. The reported surface potential for these aqueous salts is relative to theoretical calculations of ~8.0 mM SDS and 1.0 mM CTAB. The theoretical value is scaled relative to the measured data which is applied to the aqueous salts. Again, the lack of electrochemical cleaning of electrodes and degassing of solutions affects the measured potential in the region < 1.0 M. The ideal plot of measured potentials vs. concentration is shown in Figure F-1.

Appendix G. Cleaning Procedures/Protocols

G.1 Preparation of the ionizing cell prior to experiments

Figure G-1. Sequence of ionizing cell being prepared by rinsing with ultrapure water and being placed in a large acid-cleaned beaker (1000 mL). The inlet for the gas must be unscrewed prior to placement in the beaker. The ionizing cell is soaked in a piranha solution (3:1 sulfuric acid with hydrogen peroxide) for nearly 10-20 mins before quenching in ultrapure water for over 30 mins. The cell is quenched for a total of two 30 min intervals with fresh ultrapure water. The third and final quenching period with fresh ultrapure water is overnight. This process only needs to be done once every couple of weeks before start of a sequence of experiments.
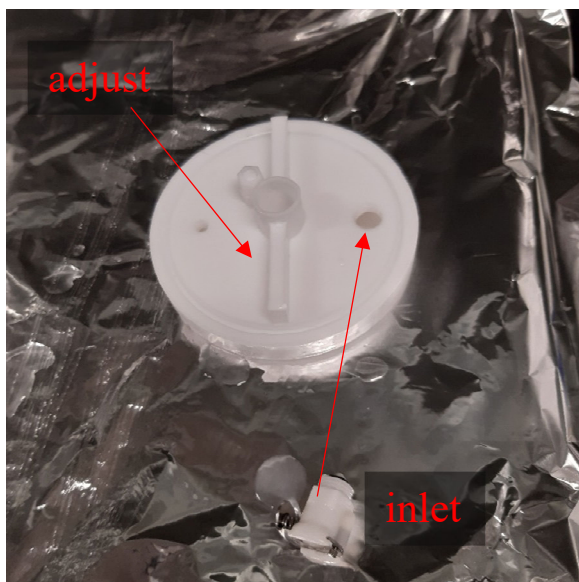
Figure G-2. Screw in the inlet and adjust the screw-top (top where Am-241 sits) to be at a height of 7 mm (from the bottom) before use in experiments.

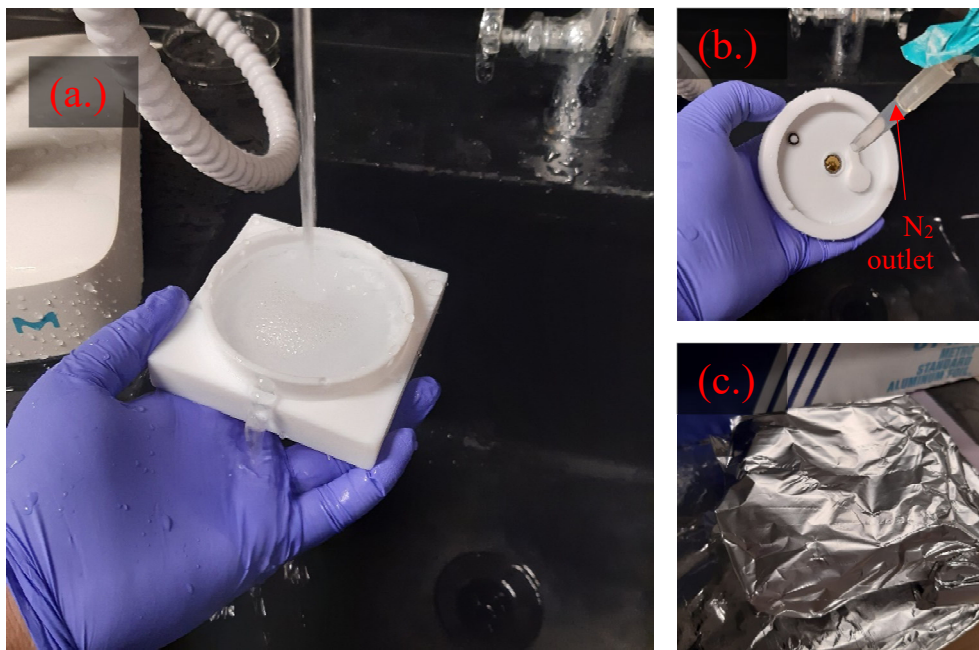## G.2 Preparation of the ionizing cell & Pt gauze prior to measurement

Figure G-3. The following process is performed before and in between consecutive measurements: (a.) The ionizing cell (must be rinsed several times with ultrapure water from the MilliQ and rinsed thoroughly with reagent alcohol. It is then completely dried (no lingering water droplets) with nitrogen gas. (b.) The Am-241is washed/rinsed/dried separately and inserted into top part of the fully dried cell. The underside of the top and Am-241 is dried again. (c.) The entire clean and dry cell is covered with aluminum foil.
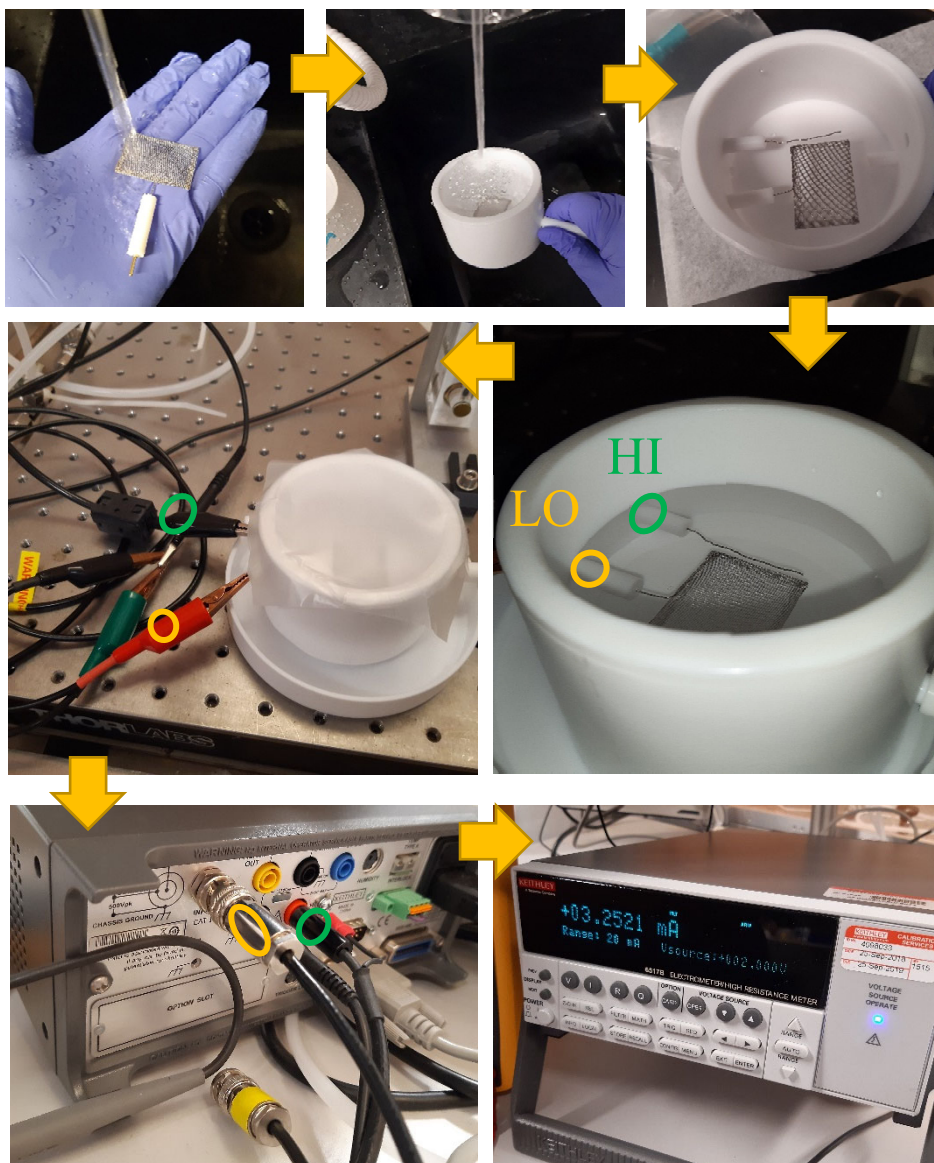
Figure G-4. The following process is repeated every time before and between consecutive measurements: The Pt gauze is rinsed (with ultrapure water only) and placed in a special PTFE cell for electrochemical cleaning. The counter electrode is a Pt wire (CH Instruments).Together, the electrodes are immersed in a solution of 0.1 M HClO$_4$ for electrochemical cleaning (also outlined in 4.2.1). Following cleaning, the Pt gauze is kept submerged in ultrapure water (prevents contaminants from sticking to the Pt surface) and carefully transferred to the ionizing cell only moments before sample placement and measurement.

Langmuir: The ACS journal of fundamental interface science
(Cover of July 6, 2021. Vol. 37, Issue 26)
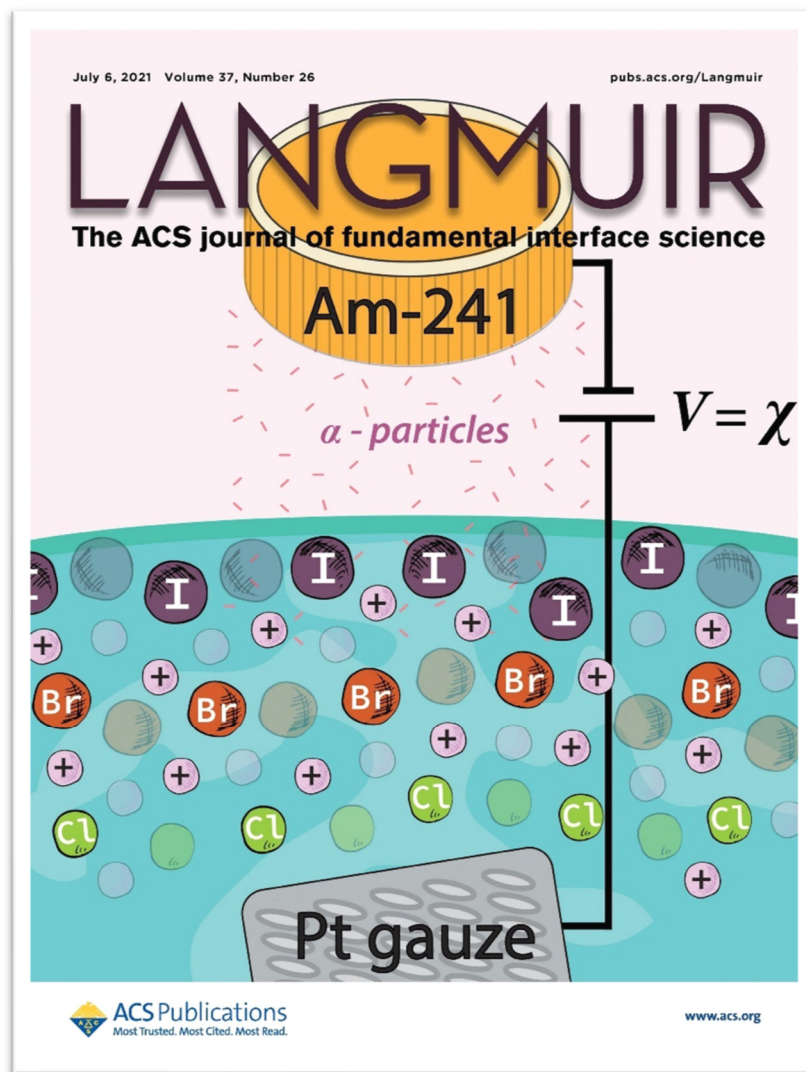
About the cover: Surface enrichment of iodide continues to be debated. Ionizing surface potential measurements quantify the "real" potential difference of the air–aqueous interface of halide salt solutions. Here, using an americium-241/platinum electrode configuration, iodide ions are observed to preferentially adsorb to the air–water interface over other aqueous halide ions: bromide and chloride. (Adel et al., *Langmuir* **2021**, 37, 7863-7874.)